



TECHNISCHE UNIVERSITÄT WIEN

DIPLOMA THESIS

Running coupling constant in the model of topological fermions

supervised by
Ao.Univ.Prof.i.R. Dipl.-Ing. Dr.techn. MANFRIED FABER
Atominstitute, TU Wien

Fabian Anmasser
Baumgasse 13/1/9
A-1030 Wien

Vienna, March 23, 2021

Manfried Faber

Fabian Anmasser

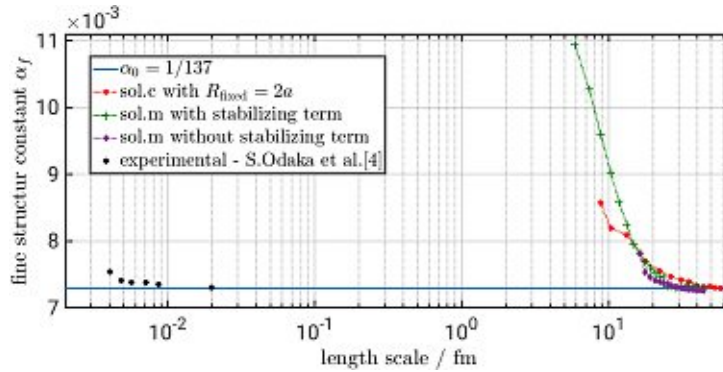
Abstract

The *model of topological fermions* (MTF) is a generalization to 3+1 dimensions of the SINE-GORDON wave equation. This is a non linear, differential equation, which solutions have particle like behaviour and are invariant under LORENTZ transformations. Solutions of the MTF are characterised by two topological quantum numbers, for spin and charge quantization, respectively. They are associated to electron/positron and spin up/down. Photon like excitations are also possible in the limit of $E_{\text{pot}} \rightarrow 0$, where the presented model converges into MAXWELL's electrodynamic.

The MTF tries to geometricize particle physics, which is a rare concept in contrast to the great efforts made to quantize gravitation. Maybe, the MTF opens a door to understand modern physics in a better way. To test the model, we compare it with the quantum field theory of electrodynamics (QED), where the effect of the running coupling constant α_f arises. This effect is also present in the SINE-GORDON model and the MTF. We want to find out, if they coincidence.

To do so, WABNIG, RESCH and THEUERKAUF developed numerical routines to minimize the energy of a dipole configuration on a lattice. In the present work, THEUERKAUF's algorithm was examined in depth on its precision. By use of this knowledge, a new numerical routine with enhanced accuracy was created in MATLAB. The overall accuracy could be improved by adding some interpolation routines, using symmetry arguments and introduce a term known from the SKYRME model. A conjugate gradient method was used to minimize the total energy of the configuration. Fortunately, the run times didn't get unreasonable big and stay in the same order of magnitude.

The new algorithm was first tested for the monopole configuration, where the analytical solution is known. After that it was applied on dipoles. The running coupling function was then extracted from the obtained energies and compared to the experimental data, which is shown in the figure below.



Contents

1	Introduction	5
2	Quantum electrodynamics	7
2.1	A brief introduction	7
2.2	Running coupling constant of QED	10
3	Model of topological fermions	17
3.1	Sine Gordon model	17
3.2	Generalisation to 3+1 dimensions	21
3.2.1	Degrees of freedom	21
3.2.2	Geometry and physics	21
3.2.3	Lagrangian	24
3.2.4	Equations of motion	26
3.2.5	Hedgehog approach	27
3.2.6	Electrodynamic limit	30
4	Gauge theories on a lattice	35
4.1	Recapitulating THEUERKAUF's algorithm	35
4.2	Gamma action	36
4.2.1	Working in cylinder coordinates	37
4.2.2	Error estimation for H_{pot}	42
4.2.3	Discretization	44
4.3	Wilson action	48
4.3.1	The QCD action in the continuum	48
4.3.2	Naive discretization of fermions	51
4.3.3	MTF on the lattice	55
4.4	Measures of accuracy	61
5	Dipole configurations	63
5.1	Energy contribution outside the box	63
5.2	Initial configuration	64

5.3	Singlet and triplet on the lattice	67
5.3.1	Adapting sol.c	68
5.3.2	Writing a Matlab simulation	70
6	Results	75
6.1	Type of integration method	75
6.2	Initialisation of a monopole configuration	76
6.3	Minimization of monopole configurations	80
6.4	Dipole configurations	84
6.4.1	Singlet energies	84
6.4.2	Running coupling in the MTF	85
7	Conclusion	87
A	Additional figures and diagrams	89
B	Lengthy calculations	91
B.1	Energy contributions for a relativistic soliton	91
B.2	Dual tensor identity	93

Chapter 1

Introduction

The history of particle physics began in the 9th century BC, where in philosophy, the idea of indivisible particles was formed. Ancient philosophers of India called the dead matter *ajiva* and they taught, that it consists of invisible particles *-permanu*, which have definite characteristics. In 5th century BC, in the tradition of LEUCIPPUS, DEMOCRITUS and EPICURUS ancient Greece philosophers represented the idea of atoms. In their language, *atomos* means not divide able.

Muslim- and early European scientists like BOYLE and NEWTON drove forward this idea by abstract reasoning. The first modern particle model was founded by DALTON in 19th century, who introduced the idea, that every chemical element consists of a characteristic particle.

Subatomic particles were found in the end of the 19th century by THOMSON and other physicists. MILLIKAN and FLETCHER measured the elemental charge with their famous oil drop experiment and showed that the electric charge is quantized in 1909. After that, the idea was formed, that negatively charged *electrons* together with yet unknown positively charged particles form an atom. Finally, experiments about radioactive decay falsified DALTON's model, where chemical elements were seen as fundamental particles.

RUTHERFORD demonstrated 1907 with his gold foil experiment, that the atom consists of a tiny core, who carries practically the total mass. This discovery was surprising, because it states that all matters consist mainly of empty space. In the following years the atom model was developed to a dense nucleus with positive charge consisting of *protons*, orbited by electrons with nearly no mass. At this point, chemistry could be explained by electromagnetic interaction between positive nuclei and electrons. The atomic number could be identified with the positive charge of the nucleus.

In research about radioactivity so called *isotopes* were found. Isotopes of a given element have the same positive charge but different characteristics and

atomic weight. This could be explained by introducing an electric neutral particle, which has to sit in the core of the atom, due to RUTHERFORD's gold foil experiment. It was called *neutron* and the term *nucleon* for constituents of the atom core were established.

Beside electromagnetic and gravitational force, the cohesion of the nucleons gave rise to a nuclear force, today known as strong force.

As EINSTEIN formulated the photo effect, the phenomena of light, which was considered to be wavelike, has become characteristics of particles. The associated elemental particle is called *photon*. Going on, the wave solutions of SCHRÖDINGER's equation showed, that particles like the electron also have a wavelike behaviour. The term particle-wave dualism was born. A particle is considered to be in certain states, classified by quantum numbers. For example in the hydrogen atom, the main quantum number n counts the semi-classical orbits of the electron from the innermost outwards. Other classical quantities like the angular momentum are also quantized. But there is no classical analogue to the spin, an intrinsic angular momentum of a particle, which orientates with respect to a quantization axis produced by an magnetic field. In 1928 DIRAC proposed his equation, which is the relativistic form of SCHRÖDINGER's one. The solutions of his equation gave rise to antiparticles and included the spin naturally. The antiparticle of the electron, the *positron* was experimentally confirmed in cosmic radiation, in 1932.

Due to energy- and angular momentum conservation, PAULI saw the need of *neutrinos* to explain the radioactive beta decay. It took 23 years to observe it for the first time in an atomic reactor. FERMI proposed a new short range force, today called the *weak* force to explain the beta decay.

With the rise of particle accelerators in the second half of the last century, energies in the MeV range were possible. And with it many new particles were found, most of them unstable. They could be divided into *mesons* and *baryons*, which appeared to be built together from the same constituents. GELL-MANN could order this particles by introducing a new quantum number, the *strangeness*. This procedure, the "Eightfold way", predicted a new particle Ω^- , which was found 1964 and supported GELL-MANN's theory. In the 1970s, the nuclear force was further developed to quantum chromodynamics. The associated fundamental force interacts between *colour* charged, subatomic particles - the *quarks*. Particles built of quarks, such as the proton and neutron are summed up by the term *hadron*.

Today, all this particles and the interactions between them are united in the *standard model*, compare figure A.0.1. Despite many successes, as predicting the HIGGS *boson*, there are some unanswered questions. The biggest of them is the unification of particle physics and gravity - an highly unsolved mystery in modern physics.

Chapter 2

Quantum electrodynamics

Since we want to compare the model of topological fermions (MTF) with the quantum field theory of electromagnetic forces (QED), we will now take a closer look on quantum electrodynamics as presented in [1] by THOMSON and give a brief introduction about it. Our goal is, to understand what the term running coupling constant means and how it could be related to the MTF.

2.1 A brief introduction

The fundamental, underlying and rigorous formulation of QED, quantum field theory would definitely go beyond the scope of this work and is not necessary for our considerations. Using perturbation theory, we want to give the reader a feeling for FEYNMAN diagrams and how the effect of the running coupling constant emerges.

Let us consider a quantum mechanical Hamiltonian, $H = H_0 + V$ with the solutions $|\phi_k\rangle$ for the unperturbed system, $H_0 |\psi\rangle = E_k |\psi\rangle$. The transition rate, Γ_{fi} is the probability for the system to get from the initial state $|\phi_i\rangle$ to the final one $|\phi_f\rangle$. It is given by FERMIS golden rule,

$$\Gamma_{fi} = 2\pi |T_{fi}|^2 \rho(E_i), \quad (2.1.1)$$

where $\rho(E_i)$ is the density of states in the initial state and T_{fi} is the associated transition matrix element. From perturbation theory in quantum mechanics, we can write T_{fi} up to first order as,

$$T_{fi} = \underbrace{\langle \phi_f | V | \phi_i \rangle}_{\text{scattering via potential}} + \underbrace{\sum_{j \neq i} \frac{\langle \phi_f | V | \phi_j \rangle \langle \phi_j | V | \phi_i \rangle}{E_i - E_j}}_{\text{scattering via intermediate state } |\phi_j\rangle} + \dots \quad (2.1.2)$$

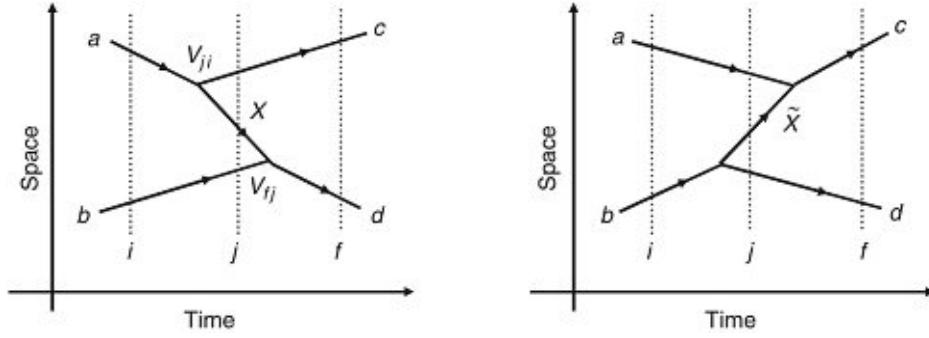


Figure 2.1.1: The two different time ordered possibilities for the interaction via a virtual particle X, from[1].

If we consider two particles 1,2 in initial state $|1_i\rangle = a$ and $|2_i\rangle = b$ interacting with each other, to get in final state $|1_f\rangle = c$ and $|2_f\rangle = d$, we have two possibilities how they can get there. $|1\rangle$ sends out a particle X and $|2\rangle$ absorbs it, or the other way round. The intermediate state in both cases would be the time between sending and absorption of X. Therefore, both cases add up to the total transition element $(T_{fi}^{12} + T_{fi}^{21})$, this is called time ordered perturbation with,

$$T_{fi}^{12} = \frac{\langle d|V|X+b\rangle\langle c+X|V|a\rangle}{(E_a - E_b) - (E_c + E_X + E_b)}, \quad (2.1.3)$$

$$T_{fi}^{21} = \frac{\langle c|V|\tilde{X}+a\rangle\langle d+\tilde{X}|V|b\rangle}{(E_a - E_b) - (E_d + E_{\tilde{X}} + E_a)}. \quad (2.1.4)$$

We introduce the abbreviations $V_{ji} = \langle c+X|V|a\rangle$ and $V_{fj} = \langle d|V|X+b\rangle$. The LORENTZ invariant matrix element M_{ji} is related to V_{ji} by,

$$V_{ji} = M_{ji}\Pi_k\sqrt{2E_k}, \quad (2.1.5)$$

where k runs over all involved particles. Hence we get,

$$V_{ji} = \frac{M_{a\rightarrow c+X}}{\sqrt{2E_a 2E_c 2E_X}} \quad \text{and} \quad V_{fj} = \frac{M_{X+b\rightarrow d}}{\sqrt{2E_b 2E_d 2E_X}}. \quad (2.1.6)$$

Inserting (2.1.6) into (2.1.3) yields,

$$T_{fi}^{12} = \frac{1}{2E_X} \frac{1}{\sqrt{2E_a 2E_b 2E_c 2E_d}} \frac{M_{a\rightarrow c+X} M_{X+b\rightarrow d}}{E_a - E_c - E_X}. \quad (2.1.7)$$

By doing the analogous steps for T_{fi}^{21} and using (2.1.5) again, we find the LORENTZ invariant matrix element,

$$\begin{aligned} M_{fi} &= (T_{fi}^{12} + T_{fi}^{21}) \Pi_i \sqrt{2E_i} = \\ &= \frac{M_{a \rightarrow c+X} M_{X+b \rightarrow d}}{2E_X} \left(\frac{1}{E_A - E_c - E_X} + \frac{1}{E_b - E_d - E_X} \right). \end{aligned} \quad (2.1.8)$$

No we use energy conservation, $E_b - E_d = E_c - E_a$ and the energy momentum relation, $E^2 = \mathbf{p}^2 + m^2$ to rearrange the last expression to,

$$M_{fi} = \frac{M_{a \rightarrow c+X} M_{X+b \rightarrow d}}{(p_a - p_c)^2 - m_X^2}, \quad (2.1.9)$$

with $q = p_a - p_c$ is the carried momentum of the virtual particle X, in our case the photon. Therefore, we have,

$$M_{fi} = M_{a \rightarrow c+X} \underbrace{\frac{1}{q^2 - m_X^2}}_{\text{propagator}} M_{X+b \rightarrow d}. \quad (2.1.10)$$

By using the DIRAC equation and minimal substitution, one gets the Hamiltonian of QED,

$$H_{\text{QED}} \psi = \underbrace{(\gamma^0 m - i\gamma^0 \vec{\gamma} \nabla)}_{H_0} \psi + \underbrace{e_0 \gamma^0 \gamma^\mu A_\mu}_{V} \psi, \quad (2.1.11)$$

with the four vector potential,

$$A_\mu = \epsilon_\mu^\lambda \exp(i(\vec{p}\vec{x} - Et)). \quad (2.1.12)$$

By inserting V into (2.1.10), we obtain,

$$\begin{aligned} M_{fi} &= M_{a \rightarrow c+X} \frac{1}{q^2} M_{X+b \rightarrow d} = \langle \psi_c | V | \psi_a \rangle \frac{1}{q^2} \langle \psi_d | V | \psi_b \rangle = \\ &= \langle \psi_c | e_0 \gamma^0 \gamma^\mu A_\mu | \psi_a \rangle \frac{1}{q^2} \langle \psi_d | e_0 \gamma^0 \gamma^\nu A_\nu | \psi_b \rangle = \\ &= e_0^2 \langle \psi_c | \gamma^0 \gamma^\mu | \psi_a \rangle \frac{\sum_\lambda \epsilon_\mu^\lambda (\epsilon_\nu^\lambda)^*}{q^2} \langle \psi_d | \gamma^0 \gamma^\nu | \psi_b \rangle = \\ &= e_0^2 \bar{u}(p_3) \gamma^\mu u(p_1) \frac{-g_{\mu\nu}}{q^2} \bar{u}(p_4) \gamma^\nu u(p_2). \end{aligned} \quad (2.1.13)$$

In (2.1.13), we used the definition for the adjoint spinor, $\bar{\psi} = \psi^\dagger \gamma^0$ and the notation u and v for particle,- and antiparticle solutions respectively. Because for the QED propagator, we have to sum over all polarisations, the sum in the third row comes into play. The identity, $\sum_\lambda \epsilon_\mu^\lambda (\epsilon_\nu^\lambda)^* = -g_{\mu\nu}$ holds.

2.2 Running coupling constant of QED

It has been a mystery ever since it was discovered more than fifty years ago, and all good theoretical physicists put this number up on their wall and worry about it. -RICHARD P. FEYNMAN[2], 1985

ARNOLD SOMMERFELD introduced the fine structure constant $\alpha_f = \frac{e_0^2}{4\pi\epsilon_0\hbar c}$ in 1916 in his research[3] regarding the spectral lines of the hydrogen atom. It is a dimensionless parameter, which represents the strength of electro-magnetic interaction and its numerical value is $137.035999084(21)^{-1}$, where the round brackets indicate the uncertainty. In the realm of QED, it is a measure for the coupling strength between photons and charged particles. Although this parameter seems to be constant in time, as there was up to now no significant deviation in time measurable, it depends on the energy scale, at which an interaction takes place. One may qualitatively imagine this circumstance in the following way: in QED the vacuum is not empty, fluctuations make particle antiparticle pair production for short times possible. This e^-e^+ pairs shield a charge and make it look smaller than it actually is, its real value remains not measurable. For high energies respectively small distances, there are less pairs to shield the charge, therefore it appears to be higher, as the experimental data from the VENUS collaboration[4] in table 2.1 suggests.

ratio	$Q = \sqrt{ q^2 }$ GeV	fit
$\alpha(t_0)/\alpha(q^2 \approx 0)$	10	1.013 ± 0.052
$\alpha(t_1)/\alpha(t_0)$	20.7 - 25.2	1.0067 ± 0.0047
$\alpha(t_2)/\alpha(t_0)$	25.2 - 32.4	1.0099 ± 0.0049
$\alpha(t_3)/\alpha(t_0)$	32.4 - 38.2	1.0099 ± 0.0061
$\alpha(t_4)/\alpha(t_0)$	38.2 - 45.6	1.0144 ± 0.0074
$\alpha(t_5)/\alpha(t_0)$	45.6 - 53.9	1.0328 ± 0.0114

Table 2.1: Shown are the measured ratios of α_f at various energies from the VENUS Collaboration[4], where BHABBA-scattering and muon-pair production at e^+e^- collisions were used. The first measurement at t_0 defines the scale and has a high error, compared to the ratios $\alpha(t_m)/\alpha(t_0)$, for which systematic errors in the experimental setup cancel. As can be clearly seen, the fit rises with higher energies Q .

The running of the coupling constant α_f is also closely intertwined to the term renormalization, as we will see in the following. To show the fine structure's dependence on the carried momentum q^2 , $\alpha_f = \alpha_f(q^2)$, we take electron-positron annihilation, $e^-e^+ \rightarrow \mu^-\mu^+$ as a working example. Note, that this leads to the same transition amplitude as electron-muon scattering. By applying the FEYNMAN rules on the diagram for electron-muon annihilation beside, the transition matrix element reads,

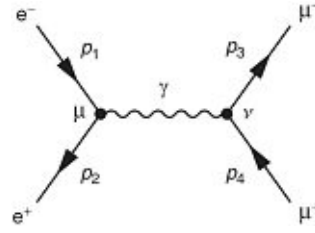


Figure 2.2.1: e^-e^+ annihilation[1].

$$M = -\{\bar{v}(p_2)[e_0\gamma^\mu]u(p_1)\}[g_{\mu\nu}/q^2]\{\bar{u}(p_3)[e_0\gamma^\nu]v(p_4)\}. \quad (2.2.1)$$

Due to the perturbation approach, we have also to consider higher order corrections, which emerge from the fact, that there are vacuum fluctuations in quantum field theories. These fluctuations allow particle pairs to arise out of the vacuum and then, after a short time, they annihilate again. The correction of order e_0^4 to the lowest order FEYNMAN diagrams are shown in figure 2.2.2. If a measurement of the cross section of such a electron-positron annihilation is done, all orders of correction are taken into account by nature. Therefore the electron charge e in a measurement is not the same as e_0 , which is referred to as the bare electron charge and participates in one single FEYNMAN diagram.

Now, one would have to add up all the higher order contributions to get the same result as for the measurement. Fortunately, the diagram (c) in figure 2.2.2, cancels exactly the effects of diagram (d) and (e). This characteristic is known as WARD identity¹ and it holds for all orders in QED, we will not go further in detail here.

Therefore, we are only left with the vacuum polarization and its multiplies. We will see later, that by using the geometrical series, it is possible to find an algebraic expression, in which all higher orders are contained. This procedure will lead us to the running of the fine structure constant $\alpha_f(q^2) = e^2(q^2)/4\pi$. Let us take a look to the FEYNMAN diagram of vacuum polarization and its

¹The WARD identity has to be fulfilled for any quantum field theory, other wise it would not be renormalise able[5].

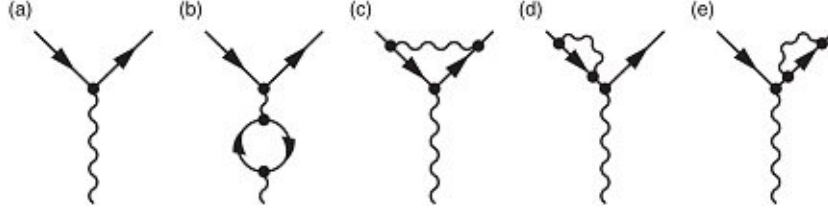


Figure 2.2.2: Leading order (a) and $\mathcal{O}(e_0^4)$ corrections (b-e) of the considered e^-e^+ annihilation[1].

transition amplitude²,

$$M = \frac{-ie_0^2}{q^4} \{ \bar{u}(p_3) \gamma^\mu u(p_1) \} \underbrace{ \left\{ \int \frac{d^4k}{(2\pi)^4} \frac{\text{Tr}[\gamma_\mu (\not{k} + mc) \gamma_\nu (\not{k} - \not{q} + mc)]}{(k^2 - m^2c^2)[(k - q)^2 - m^2c^2]} \right\}}_{\pi_{\mu\nu}(q^2)} \cdot \{ \bar{u}(p_4) \gamma^\mu u(p_2) \}, \quad (2.2.2)$$

where the loop is contained in the integral, which is divergent. This can be easily seen by estimating the overall momentums power,

$$\int |k|^3 d|k| \frac{|k|^2}{|k|^4} \rightarrow \infty, \quad \text{for } |k| \rightarrow \infty. \quad (2.2.3)$$

After a lengthy rearranging, which is not of interest for our consideration, we may write the integral in (2.2.2) as follows,

$$\pi_{\mu\nu}(q^2) = \frac{ig_{\mu\nu}q^2e_0^2}{12\pi^2} \left\{ \int_{m^2}^{\infty} \frac{dz}{z} - 6 \int_0^1 z(1-z) \ln \left[1 - \frac{q^2}{m^2c^2} z(1-z) \right] dz \right\}. \quad (2.2.4)$$

The second integral in (2.2.4) is not divergent and it is just a function $f(-q^2/m^2c^2)$. The first integral is clearly divergent, so we artificially introduce a cut off C ,

$$\int_{m^2}^{\infty} \frac{dz}{z} \rightarrow \int_{m^2}^{C^2} \frac{dz}{z} = \ln \left(\frac{C^2}{m^2} \right). \quad (2.2.5)$$

Therefore, we get for the loop integral in (2.2.2),

$$\pi_{\mu\nu}(q^2) = \frac{ig_{\mu\nu}q^2e_0^2}{12\pi^2} \left\{ \ln \left(\frac{C^2}{m^2} \right) - f \left(\frac{-q^2}{m^2c^2} \right) \right\}, \quad (2.2.6)$$

²The abbreviation \not{k} was introduced by FEYNMAN and is defined as $\not{k} \equiv \gamma_\mu k^\mu$.

and for the transition matrix element M of the electron-muon scattering we obtain,

$$M = -e_0^2 \{ \bar{u}(p_3) \gamma^\mu u(p_1) \} \frac{g_{\mu\nu}}{q^2} \left\{ 1 - \frac{e_0^2}{12\pi^2} \left[\ln \left(\frac{C^2}{m^2} \right) - f \left(\frac{-q^2}{m^2 c^2} \right) \right] \right\} \{ \bar{u}(p_4) \gamma^\mu u(p_2) \}. \quad (2.2.7)$$

Now we see, that this expression has a similar form as the contribution from the lowest order diagram, expect that the coupling constant (\propto charge) has changed from e_0 to a "renormalized" coupling constant, which reads,

$$e \equiv e_0 \sqrt{1 - \frac{e_0^2}{12\pi^2} \ln \left(\frac{C^2}{m^2} \right)}. \quad (2.2.8)$$

Inserting this expression back into (2.2.7) and we finally obtain the amplitude without the cut off C , so the infinities are gone. They are absorbed in the charge e , which is actually in the measurements involved.

$$M = -e^2 \{ \bar{u}(p_3) \gamma^\mu u(p_1) \} \frac{g_{\mu\nu}}{q^2} \left\{ 1 + \frac{e^2}{12\pi^2} f \left(\frac{-q^2}{m^2 c^2} \right) \right\} \{ \bar{u}(p_4) \gamma^\mu u(p_2) \}. \quad (2.2.9)$$

Through this procedure of renormalization, the charge has gained a dependence on the carried momentum of the photon, q^2 ,

$$e(q^2) = e(0) \sqrt{1 + \frac{e(0)^2}{12\pi^2} f \left(\frac{-q^2}{m^2 c^2} \right)}, \quad (2.2.10)$$

and by using $e^2 = 4\pi\alpha\epsilon_0\hbar c$, the fine structure constant also gains a dependence on q^2 .

After all, this whole derivation was just for the case of vacuum polarization with one loop. To take all higher corrections with arbitrary many loops into account, we define the bare propagator $P_0 \equiv e_0^2/q^2$ and recall again, that the integral in (2.2.2), which represents the loop, was abbreviated with $\pi_{\mu\nu}$. All diagrams of vacuum polarization are built up by these two components, as figure 2.2.3 shows. For the effective propagator, who contains all contributions, we make therefore the following ansatz,

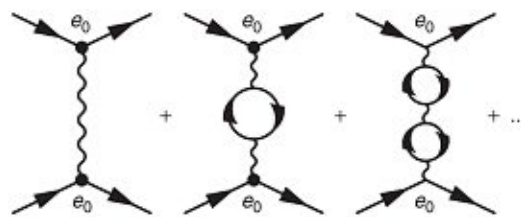


Figure 2.2.3: Higher order loop corrections[1].

$$P = P_0 + P_0 \pi_{\mu\nu}(q^2) P_0 + P_0 \pi_{\mu\nu}(q^2) P_0 \pi_{\mu\nu}(q^2) P_0 + \dots \quad (2.2.11)$$

By use of the geometrical series³ and the definition, $\Pi(q^2) \equiv \pi_{\mu\nu}/q^2$, we obtain for the effective propagator,

$$P = P_0 \frac{1}{1 - e_0^2 \Pi(q^2)} = \frac{e_0^2}{q^2} \frac{1}{1 - e_0^2 \Pi(q^2)} \equiv \frac{e^2(q^2)}{q^2}. \quad (2.2.12)$$

Therefore, the effective charge reads,

$$e^2(q^2) = \frac{e_0^2}{1 - e_0^2 \Pi(q^2)}, \quad (2.2.13)$$

which may be rearranged to e_0 ,

$$e_0^2 = \frac{e^2(\mu^2)}{1 + e^2(\mu^2) \Pi(\mu^2)}. \quad (2.2.14)$$

Here, in the last equation (2.2.14), $\mu^2 = q^2$ is the energy scale, at which the electron charge e is measured. If we insert this result back into (2.2.13), we get for the effective charge,

$$e^2(q^2) = \frac{e^2(\mu^2)}{1 - e^2(\mu^2) [\Pi(q^2) - \Pi(\mu^2)]}. \quad (2.2.15)$$

For $q^2, \mu^2 \gg m_0^2 c^2$, it can be shown[1], that the difference in the denominator simplifies to,

$$\Pi(q^2) - \Pi(\mu^2) \approx \frac{1}{12\pi^2} \ln \left(\frac{q^2}{\mu^2} \right). \quad (2.2.16)$$

Finally we arrive at an analytical expression for the running of the fine structure constant,

$$\alpha_f(q^2) = \frac{\alpha(\mu^2)}{1 - \alpha(\mu^2) \frac{1}{3\pi} \ln \left(\frac{q^2}{\mu^2} \right)}. \quad (2.2.17)$$

Generally, q has to be seen as a LORENTZ-four vector, $q^\mu = (E, \vec{p})^T$. The scalar product is given by, $q^\mu q_\mu = E^2 - \vec{p}^2 = s^2$, with \sqrt{s} called the centre-of-mass energy. To find the α_f as a function of the distance, we use the energy-momentum relation $E = \sqrt{m_0^2 c^4 + p^2 c^2}$, which simplifies in the already assumed high energy limit to $E = pc$. By inserting the DE-BROGLIE wavelength, we get a one to one correspondence for energy and distance,

$$E = \frac{hc}{\lambda}. \quad (2.2.18)$$

³ $a_0 \sum_{k=0}^{\infty} q^k = \frac{a_0}{1-q}$

Experimentally, for $\sqrt{s} = q = 193.2$ GeV, the fine structure constant was found to be $\frac{1}{127.4}$ by *ABBIENDI et al.* at the large electron-positron collider in CERN[6]. If we use this value to fix the scale, $\alpha_f(\mu = 193.2 \text{ GeV}) = 127.4^{-1}$, we are able to plot (2.2.17) as a function of energy and distance.

Chapter 3

Model of topological fermions

In this chapter, we will first introduce the SINE-GORDON model, a (1+1) dimensional wave equation with interesting solutions, which remind us strongly to particle physics. Also, an effect in analogy to the running coupling in QED is present in this model.

MANFRIED FABER[7], [8], [9] saw those analogies to particle physics and generalized the model to (3+1) dimensions, which will be part of the second subsection.

3.1 Sine Gordon model

For introducing the SINE-GORDON model, we follow REMOISSENET from [10]. To explain the model, one can imagine a mechanical set-up: a pole, on which a lot of pendulums are mounted. In addition, those pendulums are connected to their neighbours with torsion springs. If we label the deflection of the i -th pendulum with ϕ_i ($i \in \{1, 2, \dots, n\}$), the spring constant with K and the moment of inertia for one pendulum with Θ , we are able to derive the equation of motion by applying NEWTON's laws of motion. We get,

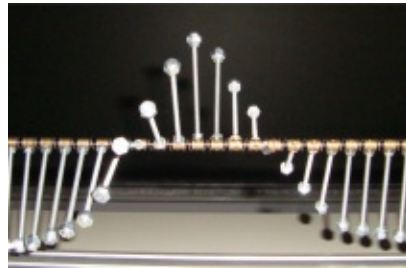


Figure 3.1.1: Mechanical model[8].

$$\Theta \frac{d^2 \phi_i}{dt^2} = K(\phi_{i+1} - 2\phi_i + \phi_{i-1}) - mgL \sin \phi_i. \quad (3.1.1)$$

L stands for the length of one pendulum, and m for its mass. By applying the continuum limit, $\phi_i(t) \rightarrow \phi(x, t)$, we get the continuous version of (3.1.1),

which reads,

$$\frac{\partial^2 \phi}{\partial t^2} - c_0 \frac{\partial \phi}{\partial x^2} + \omega_0^2 \sin \phi = 0, \quad (3.1.2)$$

with the parameters, $c_0^2 = a^2 K / \Theta$ and $\omega_0^2 = mgL / \Theta$, where a is the distance between two pendulums. To get completely rid of the constants, we introduce the substitutions,

$$T = \omega_0 t, \quad X = \frac{\omega_0}{c_0} x, \quad (3.1.3)$$

and the differential equation becomes,

$$\underbrace{\partial_T^2 \phi - \partial_X^2 \phi + \sin(\phi) = 0}_{\text{Sine-Gordon}}, \quad \underbrace{\partial_T^2 \phi - \partial_X^2 \phi + \phi = 0}_{\text{Klein-Gordon}}, \quad (3.1.4)$$

where we see the similarity to the KLEIN-GORDON equation. Here, the potential term changes from ϕ to $\sin \phi$. The KLEIN-GORDON equation was the first trial to make the SCHRÖDINGER equation invariant under LORENTZ transformations¹. The easiest way to find a solution for the SINE-GORDON equation is, by introducing a velocity v and a co-moving coordinate frame $s = X - vT$. By inserting

$$\phi = 4 \arctan \left(e^{\pm \frac{s-s_0}{\sqrt{1-v^2}}} \right) \quad (3.1.8)$$

into (3.1.4, left) one can proof that (3.1.8) is indeed a solution of the SINE-GORDON equation. The plus-minus sign in the exponential takes care of left and right turns of the pendulums. The associated solutions are called kinks and antikinks. In the mechanical model, they are produced by rotating a pendulum one full turn in clockwise or anticlockwise direction. These excitations show already particle behaviour, as kink-kink collision takes place.

¹The one dimensional SCHRÖDINGER equation reads,

$$i\hbar \partial_t \psi = H\psi, \quad (3.1.5)$$

with the non-relativistic Hamiltonian, $H = -\frac{\hbar^2}{2m} \partial_x^2 + V$. We find the KLEIN-GORDON equation by deriving (3.1.5) with respect to time,

$$i\hbar \partial_t^2 \psi = \partial_t H\psi = H \partial_t \psi = \frac{1}{i\hbar} H^2 \psi, \quad (3.1.6)$$

and inserting the relativistic energy momentum relation, $H^2 = m^2 c^4 + p^2 c^2$, with $p = -i\hbar \partial_x$.

$$\implies \frac{1}{c^2} \partial_t^2 \psi - \partial_x^2 \psi + \frac{m^2 c^2}{\hbar^2} \psi = 0. \quad (3.1.7)$$

By colliding a kink with an antikink, they annihilate each other by sending away so called *breathers*, breathers are solutions to the SINE-GORDON equation, without a full turn of the pendulums, they may be seen as analogy to photons. Another similarity to particle physics is, that moving kinks get LORENTZ contracted and experience a relativistic mass gain, as described in the following. Hence we introduce the gamma factor, $\gamma = 1/\sqrt{1-v^2}$, appearing in the exponential of 3.1.8.

In the mechanical model, we have three sorts of energies involved. The kinetic energy of a pendulum by swinging around, tension energy stored in the springs (often called *curvature* energy in this thesis) and a potential energy contribution due to gravity. By adding this parts, we get for the total energy in the system,

$$E = \frac{\Theta}{a} \omega_0 c_0 \int_{-\infty}^{\infty} \left[\underbrace{\frac{1}{2}(\partial_T \phi)^2}_{\text{kinetic}} + \underbrace{\frac{1}{2}(\partial_X \phi)^2}_{\text{tension}} + \underbrace{(1 - \cos \phi)}_{\text{potential}} \right] dX. \quad (3.1.9)$$

Inserting the solution of a single, moving kink into this formula for the energy, we get,

$$E = \gamma m_0 c_0^2, \quad (3.1.10)$$

which is precisely the formula found by EINSTEIN for relativistic mass gain², where m_0 is defined to be, $m_0 = 8 \frac{\omega_0}{c_0}$.

The kink-kink solution, where the two solitons repel each other reads,

$$\phi(X, T) = 4 \arctan \left(\frac{v \sinh(\gamma X)}{\cosh(\gamma v T)} \right), \quad (3.1.11)$$

and the attractive antikink-kink likewise,

$$\phi(X, T) = 4 \arctan \left(\frac{\sinh(\gamma v T)}{v \cosh(\gamma X)} \right). \quad (3.1.12)$$

To emphasize the localized nature of a soliton, we take a closer look to the change of the angle ϕ with respect to the position for the kink antikink case³,

$$\partial_X \phi = - \frac{4\gamma v \tanh(\gamma X) \operatorname{sech}(\gamma X) \sinh(\gamma T v)}{\operatorname{sech}^2(\gamma X) \sinh^2(\gamma T v) + v^2}, \quad (3.1.13)$$

which is plotted in the figure below.

²In appendix B, the calculation of the energy contributions for a 3 dimensional soliton and their dependencies on the LORENTZ factor γ is worked through.

³The sekans hyperbolicus function is defined as, $\operatorname{sech}(x) := \frac{1}{\cosh(x)}$.

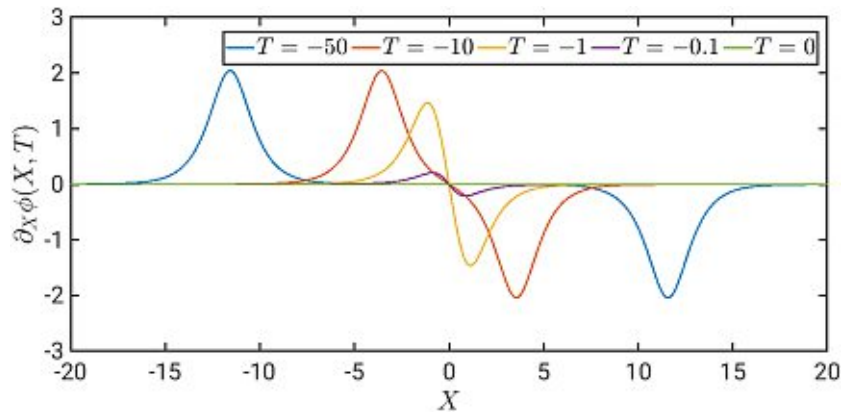


Figure 3.1.2: Particle characteristics of two solitons with opposite twist of ϕ , annihilating each other, if friction is considered. Plotted is equation (3.1.13), for different times T .

3.2 Generalisation to 3+1 dimensions

Following FABER's work in [7], [8], [9], a summary about the model of topological fermions is given in this section.

3.2.1 Degrees of freedom

As the SINE-GORDON model has one degree of freedom, we need for its generalization three of them. In our pendulum model, it is easy to imagine, what is rotating, namely the individual pendulums. In the MTF, we imagine, that space itself is twisted and this rotations are measured by three dimensional dreibeins⁴. They are associated with the three rotational angles in space, described by EULER in 1775. Another formalism to describe rotations in space was discovered by HAMILTON and even before by RODRIGUEZ - the unit *quaternions*. These are defined by,

$$Q = q_0 + q_1\mathbf{i} + q_2\mathbf{j} + q_3\mathbf{k} \quad \text{with} \quad \mathbf{i}^2 = \mathbf{j}^2 = \mathbf{k}^2 = \mathbf{ijk} = -1, \quad |Q| = 1. \quad (3.2.1)$$

For reasons to be clear later, we call q_0 the scalar- and $\vec{q} = (q_1, q_2, q_3)^T$ the vector component. More modern are the equivalent representations, the group **SO(3)** and **SU(2)**. **SU(2)** covers **SO(3)** twice and is isomorphic to the \mathbb{S}^3 - the surface of a sphere in four dimensions. Instead of the three basis elements of the quaternions, $\mathbf{i}, \mathbf{j}, \mathbf{k}$, we may use the PAULI matrices in **SU(2)**,

$$\sigma_x = \begin{pmatrix} 0 & 1 \\ 1 & 0 \end{pmatrix}, \quad \sigma_y = \begin{pmatrix} 0 & -i \\ i & 0 \end{pmatrix}, \quad \sigma_z = \begin{pmatrix} 1 & 0 \\ 0 & -1 \end{pmatrix}. \quad (3.2.2)$$

We imagine, that for every point in MINKOWSKI space, there is a 2×2 matrix associated, with three *internal* degrees of freedom. In analogy to quantum chromodynamics, we call them colour components and denote them with a subscript C in the following. Generally this **SU(2)** field may be written as,

$$Q = q_0 - i\vec{\sigma}\vec{q} = \cos \alpha(x) - i\vec{\sigma}\vec{n}(x) \sin \alpha(x). \quad (3.2.3)$$

3.2.2 Geometry and physics

Since there is a mapping between the four dimensional MINKOWSKI space and the internal colour space \mathbb{S}_C^3 , $(ct, \vec{x})^T \rightarrow (q_0, \vec{q})^T$, we want to find the rate

⁴This idea leads us to the tempting perception, that particles could be twists of space itself.

of change for $Q(x^\mu)$ with respect to its position in real space $x^\mu(s)$, where s parametrizes an arbitrary path. The derivation at the point s ,

$$\partial_s Q = \lim_{\delta s \rightarrow 0} \frac{Q(s + \delta s) - Q(s)}{\delta s}, \quad (3.2.4)$$

may be generally written as a linear combination of the basis matrices at that point, $\vec{\sigma}^Q = \vec{\sigma}Q$ with some coefficients $\vec{\Gamma}_s$,

$$\partial_s Q = -i\vec{\Gamma}_s \vec{\sigma}Q = e^{-i\vec{\sigma}\vec{\Gamma}_s dx^s} Q. \quad (3.2.5)$$

After rearranging the first equal sign in (3.2.5), we get,

$$(\partial_s Q)Q^\dagger = -i\vec{\sigma}\vec{\Gamma}_s \implies \vec{\Gamma}_s = \frac{i}{2}\text{Tr}[\vec{\sigma}\partial_s Q Q^\dagger], \quad (3.2.6)$$

which we use to find the *affine connection* $\vec{\Gamma}_s$ by inserting the **SU(2)** field $Q(x^\mu)$ from (3.2.3). By using $(\vec{\sigma}\vec{a})(\vec{\sigma}\vec{b}) = \vec{a}\vec{b} + i\vec{\sigma}(\vec{a} \times \vec{b})$, we obtain,

$$\begin{aligned} \vec{\Gamma}_s &= q_0 \partial_s \vec{q} - \vec{q} \partial_s q_0 + \vec{q} \times \partial_s \vec{q} = \\ &= \partial_s \alpha \vec{n} + \sin \alpha \cos \alpha \partial_s \vec{n} + \sin^2 \alpha \vec{n} \times \partial_s \vec{n}. \end{aligned} \quad (3.2.7)$$

In the next step, we want to assign each area element in MINKOWSKI space to an area element on the colour space \mathbb{S}_C^3 , $dx \wedge dy \rightarrow \vec{\Gamma}_x \times \vec{\Gamma}_y dx dy$, compare figure 3.2.1. The ratio between those elements is called the *curvature tensor* and is therefore defined by,

$$\vec{R}_{\mu\nu} := \vec{\Gamma}_\mu \times \vec{\Gamma}_\nu. \quad (3.2.8)$$

If we apply the symmetry of second derivatives onto the soliton field,

$$\partial_s \partial_t Q(s, t) = \partial_t \partial_s Q(s, t), \quad (3.2.9)$$

we get the so called MAURER-CARTAN equation, which is a differential form on LIE-groups, well known from differential geometry,

$$\vec{\Gamma}_\mu \times \vec{\Gamma}_\nu = \frac{1}{2} \left(\partial_\mu \vec{\Gamma}_\nu - \partial_\nu \vec{\Gamma}_\mu \right). \quad (3.2.10)$$

Using the MAURER-CARTAN equation, we find an expression for the curvature tensor, which is covariant under basis rotations,

$$\vec{R}_{\mu\nu} = \vec{\Gamma}_\mu \times \vec{\Gamma}_\nu = \frac{1}{2} \left(\partial_\mu \vec{\Gamma}_\nu - \partial_\nu \vec{\Gamma}_\mu \right) = \partial_\mu \vec{\Gamma}_\nu - \partial_\nu \vec{\Gamma}_\mu - \vec{\Gamma}_\mu \times \vec{\Gamma}_\nu. \quad (3.2.11)$$

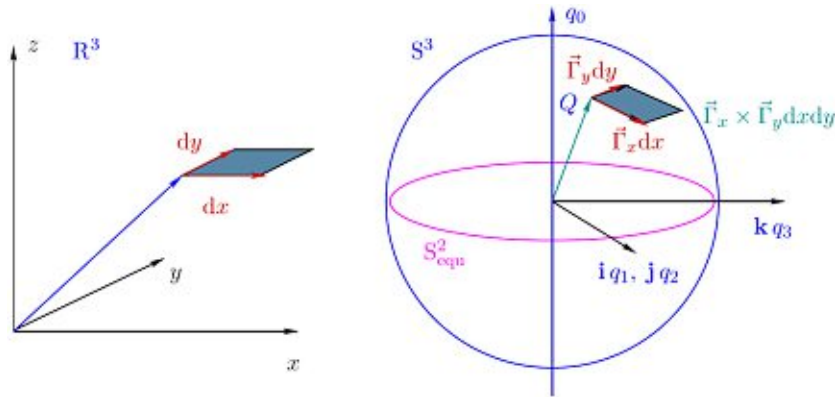


Figure 3.2.1: Illustration for the definition of the curvature tensor, taken from [8].

Before making the transition to physics, we have to take a look on the *dual* formulation of electrodynamics. The form of MAXWELL's equations in vacuum stays invariant under the transformation, $\vec{E} \rightarrow c\vec{B}$ and $c\vec{B} \rightarrow -\vec{E}$. It was therefore tempting for DIRAC to introduce magnetic monopoles, to expand this symmetry also for the case of the presence of charges,

$$\begin{array}{lcl}
 \nabla \mathbf{E} = \frac{\rho}{\varepsilon_0}, & & \nabla \mathbf{B} = \rho_M, \\
 \nabla \mathbf{B} = \rho_M, & \begin{array}{l} \mathbf{E} \rightarrow c\mathbf{B} \\ c\mathbf{B} \rightarrow -\mathbf{E} \end{array} & \nabla \mathbf{E} = \frac{\rho}{\varepsilon_0}, \\
 \nabla \mathbf{E} = -\partial_t \mathbf{B} - \mathbf{j}_M, & \xrightarrow{\rho \rightarrow \varepsilon_0 c \rho_M} & \nabla \times \mathbf{B} = \frac{1}{c^2} \partial_t \mathbf{E} + \mu_0 \mathbf{j}, \\
 \nabla \times \mathbf{B} = \frac{1}{c^2} \partial_t \mathbf{E} + \mu_0, & \begin{array}{l} \varepsilon_0 c \rho_M \rightarrow -\rho \\ \mathbf{j} \rightarrow \varepsilon_0 c \mathbf{j}_M \\ \varepsilon_0 c \mathbf{j}_M \rightarrow -\mathbf{j} \end{array} & \nabla \times \mathbf{E} = -\partial_t \mathbf{B} - \mathbf{j}_M.
 \end{array} \tag{3.2.12}$$

Up to now, no magnetic monopoles have been found. In the model of topological fermions, we use the dual formulation to describe electric monopoles instead of magnetic ones. This formulation seems to be more natural, than

the non-dual one, because if we take a look on the two tensors,

$$\begin{aligned}
 F^{\mu\nu} &= \begin{pmatrix} 0 & -\frac{E_x}{c} & -\frac{E_y}{c} & -\frac{E_z}{c} \\ \frac{E_x}{c} & 0 & -B_z & B_y \\ \frac{E_y}{c} & B_z & 0 & -B_x \\ \frac{E_z}{c} & -B_y & B_x & 0 \end{pmatrix}, \\
 {}^*F_{\mu\nu} &= \begin{pmatrix} 0 & B_x & B_y & B_z \\ -B_x & 0 & \frac{E_z}{c} & -\frac{E_y}{c} \\ -B_y & -\frac{E_z}{c} & 0 & \frac{E_x}{c} \\ -B_z & \frac{E_y}{c} & -\frac{E_x}{c} & 0 \end{pmatrix},
 \end{aligned} \tag{3.2.13}$$

we see, that for the dual formulation, the magnetic fields occupy the space-time components and the electric fields appear in the space-space components. If we remember, how magnetic fields are produced, namely by moving electric charges, this formulation feels more suitable than the other way round.

To relate physics with geometry, we set the dual field strength tensor proportional to the curvature tensor,

$$\boxed{{}^*F_{\mu\nu} \propto k \vec{R}_{\mu\nu}}. \tag{3.2.14}$$

The factor k basically fixes the units and to get the right correspondence with established electrodynamics in SI-units, the constant reads,

$$k = \frac{e_0}{4\pi\epsilon_0}. \tag{3.2.15}$$

In analogy to $F_{\mu\nu} = \partial_\mu A_\nu - \partial_\nu A_\mu$, with the four vector potential, $A^\mu = (\phi/c, \vec{A})^T$, we are able to assign a dual vector potential,

$$\vec{C}_\mu = -\frac{e_0}{4\pi\epsilon_0} \vec{\Gamma}_\mu, \quad {}^*F_{\mu\nu} = \partial_\mu \vec{C}_\nu - \partial_\nu \vec{C}_\mu. \tag{3.2.16}$$

3.2.3 Lagrangian

From classical mechanics over electrodynamics and general relativity up to quantum mechanics – all theoretical theories may be described in terms of the LAGRANGE formulation. Therefore, we follow this way and try to find the LAGRANGIAN for the MTF. It will turn out to be some sort of generalization of MAXWELL's electrodynamics, which distinguishes between charges and forces created by them. In the MTF however, there is no need for this separation. Both, the particles and forces emerge from the Q field, which can be easily seen by keeping the mechanical model in mind.

As the SINE-GORDON model is non-linear, we also expect its generalization to be of that form and MAXWELL's electrodynamics should be its linearisation. To find the LAGRANGIAN, we use an elimination process. Since the action has to be a LORENTZ-invariant quantity, the curvature tensor $\vec{R}_{\mu\nu}$ has to appear in even powers to contract both, the space-time- and colour indices. As we will see, for $\mathcal{L} \propto \vec{R}_{\mu\nu}\vec{R}^{\mu\nu}$, we get accordance with electrodynamics. As for all things in equilibrium, there are always at least two forces fighting against each other, creating a point, where both of them are equally strong. To get stable excitations, the need for such a counterpart to the curvature energy is given. In the mechanical model, this is the potential energy due to gravity. For the (3+1) model, we introduce a potential term Λ^5 . Hence, we define the LAGRANGIAN to be,

$$\mathcal{L} := \mathcal{L}_{\text{cur}} - \mathcal{H}_{\text{pot}} = -\frac{\alpha_f \hbar c}{4\pi} \left(\frac{1}{4} \vec{R}_{\mu\nu} \vec{R}^{\mu\nu} + \Lambda \right), \quad (3.2.17)$$

where the pre-factor to get SI-units is chosen to be in harmony with (3.2.15). To find an appropriate expression for the potential term, we use again an elimination process. Using the HOBART-DERRICK theorem, we know that only less than three derivatives can be involved. This means, that essentially two, or no derivatives can stay to preserve invariance under LORENTZ transformations. Furthermore, we are able to exclude the case of two derivatives, because such a term was already examined by SKYRME, describing short range interactions, like they appear in QCD.

Due to the sphere-symmetrical nature of a particle, no directional components of the Q field should play a role in the potential term and only even powers are allowed, leading to $\Lambda \propto q_0^{2m}$, with $m = 1, 2, 3, \dots$. Comparing with the curvature part, where four derivatives of Q are involved, we need an inverse length to the fourth power in the potential term to get the right dimension. Therefore, we claim the potential term to be,

$$\Lambda(q_0) = \frac{q_0^{2m}}{r_0^4}, \quad \text{with } m \in \mathbb{N} \setminus 0. \quad (3.2.18)$$

The constant r_0 fixes the length- and energy scale for a soliton. Hence, the theory of MTF is described by,

$$\boxed{\mathcal{L}_{\text{MTF}} = -\frac{\alpha_f \hbar c}{4\pi} \left(\frac{1}{4} \vec{R}_{\mu\nu} \vec{R}^{\mu\nu} + \frac{q_0^{2m}}{r_0^4} \right)}, \quad (3.2.19)$$

⁵The Greek letter Λ is not chosen at random here, it is a homage to the cosmological constant arising in general relativity. Maybe the dark matter/energy manifests as the potential energy needed in MTF.

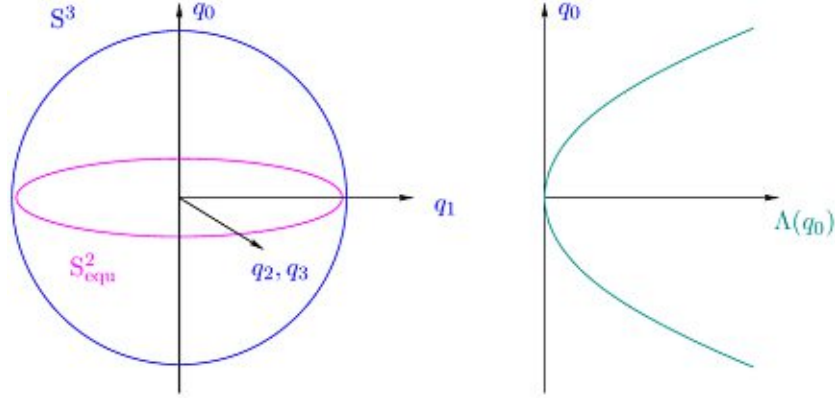


Figure 3.2.2: For $\Lambda = 0$, electrodynamics is recovered, therefore photons may be interpreted as goldstone bosons of the MTF. Illustration was taken from [8].

and the corresponding canonical energy-momentum tensor is given by,

$$\Theta^\mu{}_\nu = -\frac{\alpha_f \hbar c}{4\pi} \left(\vec{R}_{\nu\sigma} \vec{R}^{\mu\sigma} - \frac{1}{4} \vec{R}_{\rho\sigma} \vec{R}^{\rho\sigma} \delta^\mu{}_\nu - \Lambda \delta^\mu{}_\nu \right). \quad (3.2.20)$$

This energy-momentum tensor is naturally symmetric, whereas in usual electrodynamics, it needs to be symmetrized by help of an artificial procedure – another nice indicator for the relevance of the MTF.

3.2.4 Equations of motion

After having found the LAGRANGIAN, we are ready to derive the EULER-LAGRANGE equations of motion, using the variation principle. We vary the soliton field Q , by multiplication with the $\mathbf{SU}(2)$ matrix, $\exp(i\vec{\sigma}\vec{\zeta})$. Therefore the constraint $|Q| = 1$ remains preserved. After some technical work, one obtains,

$$\delta S[\vec{\zeta}] = \int d^4x \delta \mathcal{L} = \int d^4x \vec{\zeta} [\vec{q} \partial_{q_0} \Lambda + \partial_\mu (\vec{\Gamma}_\nu \times \vec{R}^{\mu\nu})] = 0. \quad (3.2.21)$$

Hence, the equations of motion read,

$$\partial_\mu [\vec{\Gamma}_\nu \times \vec{R}^{\mu\nu}] + \vec{q} \frac{d\Lambda}{dq_0} = 0, \quad (3.2.22)$$

which may be seen as a generalization of NEWTON's second axiom, $\vec{p} = -\nabla V$.

3.2.5 Hedgehog approach

Now we are ready to construct explicit solutions for particles using the general $SU(2)$ field in (3.2.3). Again, exploiting the spherical symmetry of a particle, we are able to reduce the dependencies of the profile function α and the \vec{n} -field to the radial distance. The simplest, static, radial symmetric vector field one can imagine looks like a hedgehog, pointing away⁶ from the centre with length one everywhere,

$$\vec{n}(x) = \frac{\vec{r}}{r}, \quad \alpha(\rho) = \alpha\left(\frac{r}{r_0}\right) \in [0, \pi/2], \quad (3.2.23)$$

where the dimensionless variable $\rho = r/r_0$ is introduced. In the following, we will try to find the functional expression for $\alpha(\rho)$ to fully solve the problem and compare the solution with the electron known from measurements. By inserting the hedgehog ansatz into (3.2.7), we get the connections $\vec{\Gamma}_i$ in spherical coordinates,

$$\begin{aligned} \vec{\Gamma}_r &= \partial_\rho \alpha(\rho) \vec{n}, \\ \vec{\Gamma}_\vartheta &= \sin \alpha [\cos \alpha \hat{e}_\theta + \sin \alpha \hat{e}_\phi], \\ \vec{\Gamma}_\varphi &= \sin \theta \sin \alpha [\cos \alpha \hat{e}_\phi - \sin \alpha \hat{e}_\theta]. \end{aligned} \quad (3.2.24)$$

One must not be confused at this point with the double occurring angles. θ and ϕ indicate internal colour components, whereas ϑ and φ assign indices in external, "real" MINKOWSKI space.

After having found the connections, we can divide them by their length scales in spherical coordinates, $g_{\mu\nu} = (-1, l_r^2, l_\vartheta^2, l_\varphi^2)$, with $(l_r, l_\vartheta, l_\varphi) = (1, r, r \sin \vartheta)$ and insert them into (3.2.16), to obtain the dual gauge fields \vec{C}_i ,

$$\begin{aligned} \vec{C}_r &= -\frac{e_0}{4\pi\epsilon_0 c} \frac{\vec{\Gamma}_r}{l_r}, \\ \vec{C}_\vartheta &= -\frac{e_0}{4\pi\epsilon_0 c} \frac{\vec{\Gamma}_\vartheta}{l_\vartheta}, \\ \vec{C}_\varphi &= -\frac{e_0}{4\pi\epsilon_0 c} \frac{\vec{\Gamma}_\varphi}{l_\varphi}. \end{aligned} \quad (3.2.25)$$

We find the associated electric field components by comparison with the dual field strength tensor in spherical coordinates, for example, $\vec{E}_r \propto \vec{R}_{\vartheta\varphi} =$

⁶Or towards the centre. We will see, that those configurations correspond to the exact same particle, except it carries the opposite charge.

$\vec{\Gamma}_\vartheta \times \vec{\Gamma}_\varphi$. Therefore in this model, the electric and magnetic fields can be interpreted as the ratios of area elements in internal- and external space,

$$\begin{aligned}\vec{E}_r &= -\frac{e_0}{4\pi\epsilon_0} \frac{\vec{\Gamma}_\vartheta \times \vec{\Gamma}_\varphi}{r^2 \sin \vartheta} = -\frac{e_0}{4\pi\epsilon_0} \frac{\sin^2 \alpha}{r^2} \vec{n}, \\ \vec{E}_\vartheta &= -\frac{e_0}{4\pi\epsilon_0} \frac{\vec{\Gamma}_\varphi \times \vec{\Gamma}_r}{r \sin \vartheta} = -\frac{e_0}{4\pi\epsilon_0} \frac{\alpha'(r) \sin \alpha}{r} (\cos \alpha \hat{e}_\theta + \sin \alpha \hat{e}_\phi), \\ \vec{E}_\varphi &= -\frac{e_0}{4\pi\epsilon_0} \frac{\vec{\Gamma}_r \times \vec{\Gamma}_\vartheta}{r} = -\frac{e_0}{4\pi\epsilon_0} \frac{\alpha'(r) \sin \alpha}{r} (\cos \alpha \hat{e}_\phi + \sin \alpha \hat{e}_\theta).\end{aligned}\quad (3.2.26)$$

As expected for a statical solution, all other components, which are the magnetic ones of the curvature tensor, vanish. Hence, we are able to find the total energy functional of this configuration by using $H_e = \epsilon_0/2 \int d^3x (\vec{E}_r \vec{E}_r + \vec{E}_\vartheta \vec{E}_\vartheta + \vec{E}_\varphi \vec{E}_\varphi)$ from electrodynamics,

$$H[\alpha] = H_e + H_{\text{pot}} = \frac{\alpha_f \hbar c}{r_0} \int_0^\infty d\rho \left[\underbrace{\frac{\sin^4 \alpha}{2\rho^2} + (\partial_\rho \cos \alpha)^2}_{h_e} + \underbrace{\rho^2 \cos^{2m} \alpha}_{h_{\text{pot}}} \right]. \quad (3.2.27)$$

h_e and h_{pot} are the electrical and potential radial energy density. By setting the variation of the functional $H[\alpha]$ with respect to the function $\alpha(\rho)$ equal to zero, we obtain a differential equation,

$$\partial_\rho^2 \cos \alpha + \frac{(1 - \cos^2 \alpha) \cos \alpha}{\rho^2} - m\rho^2 \cos^{2m-1} \alpha = 0, \quad (3.2.28)$$

which solutions minimize the energy functional. Obviously, for different values of m , we obtain different solutions. For $m = 2$ and $m = 3$ solutions were already found. The most appealing one seems to be the case $m = 3$, leading to,

$$\alpha(\rho) = \arctan \rho. \quad (3.2.29)$$

Therefore the component q_0^7 of the Q field reads,

$$q_0 = \frac{r_0}{\sqrt{r_0^2 + r^2}}. \quad (3.2.30)$$

Inserting the just found solution for $\alpha(\rho)$ into h_e and h_{pot} , we get for the total radial energy density,

$$h(\rho) = \frac{\alpha_f \hbar c}{r_0} \left[\frac{\rho^2}{2(1 + \rho^2)^2} + \frac{\rho^2}{(1 + \rho^2)^3} + \frac{\rho^2}{(1 + \rho^2)^3} \right]. \quad (3.2.31)$$

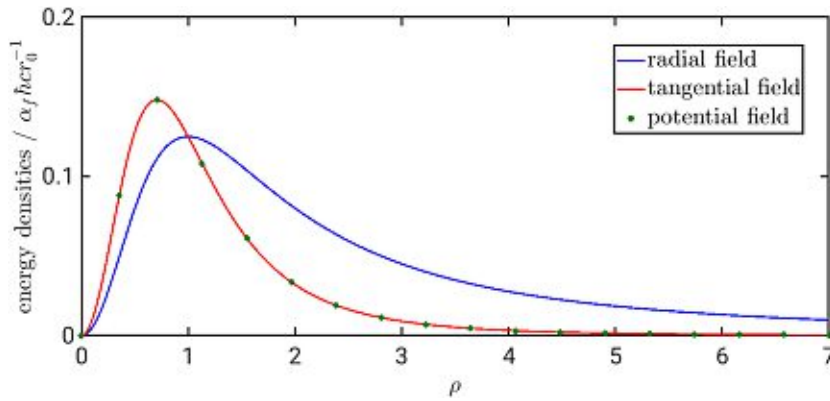


Figure 3.2.3: Plot of the three terms energy densities in (3.2.31). Tangential and potential components approach zero relatively quickly, whereas the radial component shows the usual $1/r^2$ behaviour for large distances.

Although soliton solutions show clearly characteristics of particles, there are no singularities in the vicinity arising in this model. This circumstance may be seen in figure 3.2.3, where the three energy density contributions are plotted. Integrating them over the whole \mathbb{R}^3 , leads to the total energy of an electron,

$$H_{\text{mono}} = \frac{\alpha_f \hbar c \pi}{r_0} \frac{\pi}{4}. \quad (3.2.32)$$

From measurements, we know the rest mass of an electron is about 0.511 MeV. Inserting this value into (3.2.32), and we are able to calculate the radius,

$$r_0 = \frac{\alpha_f \hbar c \pi}{H_{\text{mono}} \frac{\pi}{4}} \approx \frac{1.44 \text{ MeVfm} \pi}{0.511 \text{ MeV} \frac{\pi}{4}} = 2.21 \text{ fm}, \quad (3.2.33)$$

which comes very close to the classical electron radius from BOHR's atomic model, 2.82 fm.

As a consequence of the HOBART-DERRICK theorem or by calculating the energies explicitly, one will find, that the ratio between total energy and the potential one is exactly four. This will be an important measure of accuracy to control the validity of our numerical computations later on,

$$\frac{H_{\text{mono}}}{H_{\text{pot}}} = 4. \quad (3.2.34)$$

⁷This component is here explicitly written out, because we will need it later for finding a good initial configuration of the dipoles.

3.2.6 Electrodynamic limit

For vanishing potential energy, $\Lambda(q_0) \rightarrow 0$, which means, far away from the monopole centres, we come into the regime of ordinary electrodynamics. It is comparable with the mechanical model, where the gravitation is switched off. Due to the absence of particles, we call it *vacuum*. Setting $\alpha = \pi/2$ in (3.2.3), its $\mathbf{SU}(2)$ field reads,

$$Q = -i\vec{\sigma}\vec{n} \in \mathbb{S}_{\text{equ}}^2, \quad (3.2.35)$$

where $\mathbb{S}_{\text{equ}}^2$ denotes the equator of \mathbb{S}^3 , compare figure 3.2.2. By inserting the vacuum field into (3.2.7) and (3.2.8), we get for the curvature tensor,

$$\vec{\Gamma}_\mu = \vec{n} \times \partial_\mu \vec{n}, \quad (3.2.36)$$

$$\vec{R}_{\mu\nu} = \partial_\mu \vec{n} \times \partial_\nu \vec{n}. \quad (3.2.37)$$

We see, that $\vec{R}_{\mu\nu}$ points in the same direction as \vec{n} , therefore we are able to get rid of the colour components, by projecting the tensor onto \vec{n} . Up to a constant to stay in SI-units, we identify $\vec{R}_{\mu\nu}\vec{n}$ as the dual electromagnetic field strength tensor known from ordinary electrodynamics,

$${}^*f_{\mu\nu} = -\frac{e_0}{4\pi\epsilon_0 c} \vec{R}_{\mu\nu}\vec{n} = -\frac{e_0}{4\pi\epsilon_0 c} \vec{n}[\partial_\mu \vec{n} \times \partial_\nu \vec{n}] = \begin{pmatrix} 0 & B_x & B_y & B_z \\ -B_x & 0 & \frac{E_z}{c} & -\frac{E_y}{c} \\ -B_y & -\frac{E_z}{c} & 0 & \frac{E_x}{c} \\ -B_z & \frac{E_y}{c} & -\frac{E_x}{c} & 0 \end{pmatrix}, \quad (3.2.38)$$

and the electrodynamic LAGRANGIAN,

$$\mathcal{L}_{\text{ED}} = -\frac{\alpha_f \hbar c}{4\pi} \frac{1}{4} (\vec{n}\vec{R}_{\mu\nu})(\vec{n}\vec{R}^{\mu\nu}) = -\frac{1}{4\mu_0} {}^*f_{\mu\nu} {}^*f^{\mu\nu}. \quad (3.2.39)$$

The charge inside a closed surface \mathcal{S} may be related to the flux across the surface, by using GAUSS's law,

$$Q_e(\mathcal{S}) = \int_{\mathcal{V}} d^3x \rho = \epsilon_0 c \oint_{\partial\mathcal{V}} dudv {}^*f_{uv}, \quad (3.2.40)$$

where u and v parametrize the surface and \mathcal{V} is the volume surrounded by \mathcal{S} . Inserting (3.2.38) and we get,

$$Q_e(\mathcal{S}) = -e_0 \underbrace{\frac{1}{4\pi} \oint_{\mathcal{S}} dudv \vec{n}[\partial_u \vec{n} \times \partial_v \vec{n}]}_{\text{winding number } w(\mathcal{S})}. \quad (3.2.41)$$

In topology, a winding number is an integer, which counts full circulations of a closed curve around a certain point⁸. The winding number in our case

⁸See A.0.2 for intuitive understanding

matches with the one, known from the map, $\mathbb{S} \rightarrow \mathbb{S}_{\text{equ}}^2$. $w(\mathcal{S})$ counts essentially the charges inside a sphere. For example, inserting the hedgehog $\vec{n} = \vec{r}/r$, leads to $w(\mathcal{S}) = 1$ and the anti hedgehog, $\vec{n} = -\vec{r}/r$ to $w(\mathcal{S}) = -1$. The analogy to the mechanical model is once more given, where charges are replaced by twists in clock- or anti clockwise direction.

Since only integer values for the winding number are possible, we call $w(\mathcal{S})$ a topological quantum number and it determines the charge,

$$q_{\text{electric}}(\mathcal{S}) = -e_0 w(\mathcal{S}). \quad (3.2.42)$$

To find the MAXWELLS equations, we once again use GAUSS's law,

$$\begin{aligned} \oint_{\mathcal{S}} dx^\mu dx^\nu \star f_{\mu\nu} &= \frac{1}{3} \int_V dx^\mu dx^\nu dx^\rho \underbrace{(\partial_\mu \star f_{\nu\rho} + \partial_\nu \star f_{\rho\mu} + \partial_\rho \star f_{\mu\nu})}_{3 \operatorname{div} \star f} \stackrel{B.2}{=} \\ &= \frac{1}{3} \int_V dx^\mu dx^\nu dx^\rho \epsilon_{\mu\nu\rho\sigma} \partial_\lambda f^{\lambda\sigma} = \\ &= \frac{\mu_0}{3} \int_V dx^\mu dx^\nu dx^\rho \epsilon_{\mu\nu\rho\sigma} j^\sigma. \end{aligned} \quad (3.2.43)$$

Due to the arbitrary volume of integration, we find $\partial_\mu f^{\mu\nu} = \mu_0 j^\nu$, which are the two inhomogeneous equations in four dimensional formulation. For the other two, the homogeneous ones, we need the equations of motion (3.2.22) in electrodynamic limit,

$$\begin{aligned} 0 &= \partial_\mu [\vec{\Gamma}_\nu \times \vec{R}^{\mu\nu}] = \partial_\mu [(\partial_\nu \vec{n} \times \vec{n}) \times (\partial^\mu \vec{n} \times \partial^\nu \vec{n})] = \\ &= -\partial_\mu \underbrace{\{\partial_\nu \vec{n} [\vec{n} (\partial^\mu \vec{n} \times \partial^\nu \vec{n})]\}}_{\star f^{\mu\nu}} = -\partial_\nu \vec{n} \underbrace{\partial_\mu [\vec{n} (\partial^\mu \vec{n} \times \partial^\nu \vec{n})]}_{G^\nu}. \end{aligned} \quad (3.2.44)$$

G^ν is the magnetic current density in natural units. We denote it in SI-units with,

$$g^\nu = -\frac{e_0}{4\pi\epsilon_0} G^\nu = (c\rho_M, \mathbf{g}). \quad (3.2.45)$$

We rewrite (3.2.44), to get,

$$g^\nu = c \partial_\mu \star f^{\mu\nu}, \quad (3.2.46)$$

where the other two MAXWELL equations are encoded,

$$\partial_\mu f^{\mu\nu} = \mu_0 j^\nu \Leftrightarrow \begin{cases} \frac{\rho}{\epsilon_0} = \nabla \cdot \mathbf{E}, \\ \frac{\mathbf{j}}{\epsilon_0} = c^2 \nabla \times \mathbf{B} - \partial_t \mathbf{E}, \end{cases} \quad (3.2.47)$$

$$g^\mu = c \partial_\nu \star f^{\nu\mu} \Leftrightarrow \begin{cases} \rho_M = \nabla \cdot \mathbf{B}, \\ \mathbf{g} = -\nabla \times \mathbf{E} - \partial_t \mathbf{B}. \end{cases} \quad (3.2.48)$$

Nevertheless, we are able to find further constraints to the \mathbf{E} and \mathbf{B} fields in (3.2.44), which show a need for explanation. They are,

$$\begin{aligned}\mathbf{B}\mathbf{g} &= 0, \\ c^2\mathbf{B}\rho_M &= \mathbf{g} \times \mathbf{E},\end{aligned}\tag{3.2.49}$$

and are not linear independent from (3.2.48). They imply, that electric- and magnetic fields have to be perpendicular to each other. However, it is easy to construct an experimental setup, which leads to parallel fields, contradicting therefore the MTF. An excuse could be, that on a microscopic scale, the equations (3.2.49) hold, whereas in the macroscopic world, an average over space or time breaks the condition.

Spin quantization & elemental solitons

A volume element in real space, parametrized in spherical coordinates, reads, $dV_e = r^2 \sin \theta dr d\vartheta d\varphi$. The associated element in the internal space therefore is, $dV_i = \vec{\Gamma}_r(\vec{\Gamma}_\vartheta \times \vec{\Gamma}_\varphi) dr d\vartheta d\varphi$. The integral over the whole space of that volume element, normalized to the surface of a sphere in four dimensions,

$$\mathcal{Q} = \frac{1}{V(\mathcal{S}^3)} \int_0^\infty dr \int_0^\pi d\vartheta \int_0^{2\pi} d\varphi \vec{\Gamma}_r(\vec{\Gamma}_\vartheta \times \vec{\Gamma}_\varphi),\tag{3.2.50}$$

$$V(\mathcal{S}^3) = \int_{S^2} d^2n \int_0^\pi d\alpha \sin^2 \alpha = 2\pi^2,\tag{3.2.51}$$

is called the topological charge. It is the second topological quantum number beside the winding number. It counts the coverings of a configuration in the internal space, \mathcal{S}^3 . For a hedge-hog ansatz, we get $\mathcal{Q} = 1/2$ and we can define it to has spin up, or $+1/2$.

In [9], it was shown that \mathcal{Q} is time independent. Stable monopole configurations are therefore characterised by the two integers, \mathcal{Q} and w_s . We are now able to use the hedge-hog solution, with $\mathcal{Q} = +1/2$ and $w_s = +1$ to construct other topological distinct configurations by applying certain transformations. First one is the parity transformation $\Pi_{\vec{n}}$, which mirrors points around the origin,

$$\begin{aligned}\vec{n}(\vec{r}) &\rightarrow -\vec{n}(\vec{r}), \\ Q &\rightarrow Q^\dagger = \exp(-i\alpha\vec{\sigma}\vec{n}), \\ w_s &\rightarrow -w_s, \\ \mathcal{Q} &\rightarrow -\mathcal{Q},\end{aligned}\tag{3.2.52}$$

leading to a change of sign for \mathcal{Q} . Consequently, we could call this case spin down, or $\mathcal{Q} = -1/2$. Summarizing the two relations of the found topological quantum numbers for charge and spin, we have in the MTF,

$$\boxed{q_{\text{electric}} = -e_0 w_s, \quad \text{and} \quad s = |\mathcal{Q}|.} \quad (3.2.53)$$

The second transformation is the multiplication by the centre-element, $z = \exp(i\pi\sigma_z)$ ⁹, $\mathcal{Q} \rightarrow z\mathcal{Q}$,

$$\begin{aligned} \vec{n}(\vec{r}) &\rightarrow -\vec{n}(\vec{r}), \\ \alpha &\rightarrow \pi - \alpha, \\ w_s &\rightarrow -w_s, \\ \mathcal{Q} &\rightarrow \mathcal{Q}, \end{aligned} \quad (3.2.54)$$

which only changes the sign of the winding number and therefore the charge, analogously to the conjugation operator in particle physics. Hence, we obtain four different solitons, which are topologically distinct, compare figure 3.2.4. One might be likely reminded to the DIRAC equation, with the four component spinors as solutions. In DIRAC representation, the upper two components describe a particle with spin up- and down, whereas the lower two characterize an antiparticle with spin up- and down.

⁹The centre-elements of a group G is the set, $Z(G) := \{z \in G \mid \forall g \in G : gz = zg\}$.

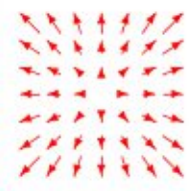
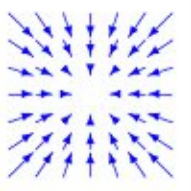
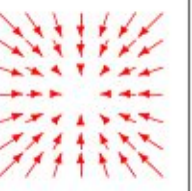
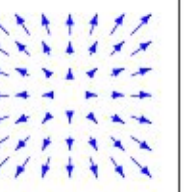
parameter	1	z	Π_n	$z\Pi_n$
n_K	r_K/r	$-r_K/r$	$-r_K/r$	r_K/r
q_0	≥ 0	≤ 0	≥ 0	≤ 0
w_s	1	-1	-1	1
$2Q$	1	1	-1	-1
diagram				

Figure 3.2.4: "Elemental soliton configurations". Shown are cross-sections of the spheric symmetrical vector part, \vec{q} . The sign of q_0 is depicted in the colour with, red stands for $q_0 > 0$ and blue for $q_0 < 0$. Illustration was made by THEUERKAUF[11].

Chapter 4

Gauge theories on a lattice

Lattice calculations are likely to be used, where problems can not be solved by a perturbation approach, like in QCD. The idea of the lattice computation is to look at the space-time structure only on a discrete, four dimensional grid or lattice. Field components are therefore only defined on points and derivations are approximated by discrete versions. The fundamental parameter is the lattice constant, which measures the distance between two points, who are equidistant distributed in each of the four directions.

To minimize the energy- or action function, one may use a method based on random field changes or a high dimensional gradient descent.

4.1 Recapitulating THEUERKAUF's algorithm

Building up on the work of WABNIG[12] and RESCH[13], THEUERKAUF developed a *c* program in his diploma thesis[11], which minimizes the energy for a soliton configuration on a lattice. The goal was to do dipole configurations, therefore the cylindrical symmetry was exploited. To save memory, no time dependence was considered. The idea is, to see the time evolution of a collision of two fermions like a film, where it is good enough to compute the individual frames. The distance between the poles was changed for every frame, therefore getting the energy as a function of the dipole distance, which may be compared to the COULOMB potential. We expect, that the deviations to that potential, is governed by the formula of the running coupling constant of QED.

To begin with, THEUERKAUF has done monopole configurations with two different methods, namely GAMMA- and WILSON action. In the first case, the three energy components, H_{cur} , H_{pot} and H_{out} are calculated as a function of the soliton field. The second method works in analogy to the lattice

simulations of QCD. Both methods are in detail explained in this chapter. To minimize the total energy, a standard routine called POWELL from numerical recipes[14] was implemented.

4.2 Gamma action

The energy momentum tensor of the MTF as derived in (3.2.20), reads,

$$\Theta^\mu_\nu = -\frac{\alpha_f \hbar c}{4\pi} \left(\vec{R}_{\nu\sigma} \vec{R}^{\mu\sigma} - \frac{1}{4} \vec{R}_{\rho\sigma} \vec{R}^{\rho\sigma} \delta^\mu_\nu - \Lambda \delta^\mu_\nu \right), \quad (4.2.1)$$

The energy density is the (00)-component of the energy momentum tensor,

$$\begin{aligned} \Theta^0_0 &= -\frac{\alpha_f \hbar c}{4\pi} \left(\vec{R}_{0\sigma} \vec{R}^{0\sigma} - \frac{1}{4} \vec{R}_{\rho\sigma} \vec{R}^{\rho\sigma} - \Lambda \right) = \\ &= \underbrace{-\frac{\alpha_f \hbar c}{4\pi} \left(\vec{R}_{0\sigma} \vec{R}^{0\sigma} - \frac{1}{4} \vec{R}_{\rho\sigma} \vec{R}^{\rho\sigma} \right)}_{\mathcal{H}_{\text{cur}} + \mathcal{H}_{\text{kin}}} + \underbrace{\frac{\alpha_f \hbar c}{4\pi} \Lambda(q_0)}_{\mathcal{H}_{\text{pot}}} \end{aligned} \quad (4.2.2)$$

To calculate the multiplications of tensor components, we remember the form of the curvature tensor,

$${}^* \vec{F}_{\mu\nu} = \frac{1}{2} \left(\partial_\mu \vec{C}_\nu - \partial_\nu \vec{C}_\mu \right) = -\frac{e_0}{4\pi\epsilon_0 c} \vec{R}_{\mu\nu} = \begin{pmatrix} 0 & \vec{B}_1 & \vec{B}_2 & \vec{B}_3 \\ -\vec{B}_1 & 0 & \frac{\vec{E}_3}{c} & -\frac{\vec{E}_2}{c} \\ -\vec{B}_2 & -\frac{\vec{E}_3}{c} & 0 & \frac{\vec{E}_1}{c} \\ -\vec{B}_3 & \frac{\vec{E}_2}{c} & -\frac{\vec{E}_1}{c} & 0 \end{pmatrix}, \quad (4.2.3)$$

and get for the products,

$$\vec{R}_{0\sigma} \vec{R}^{0\sigma} = -\left(\frac{4\pi\epsilon_0 c}{e_0} \right)^2 \underbrace{\left(\vec{B}_1^2 + \vec{B}_2^2 + \vec{B}_3^2 \right)}_{\vec{B}_i \vec{B}_i \equiv \vec{B}\vec{B}}, \quad (4.2.4)$$

$$\vec{R}_{\mu\nu} \vec{R}^{\mu\nu} = 2 \left(\frac{4\pi\epsilon_0}{e_0} \right)^2 \left(\vec{E}\vec{E} - c^2 \vec{B}\vec{B} \right). \quad (4.2.5)$$

The constants may be further reduced by using the fine structure constant,

$$\left(\frac{4\pi\epsilon_0 c}{e_0} \right)^2 \cdot \left(-\frac{\alpha_f \hbar c}{4\pi} \right) = -\frac{4\pi\epsilon_0^2 \hbar c^3}{e_0^2} \alpha_f = -\frac{4\pi\epsilon_0^2 \hbar c^3}{e_0^2} \underbrace{\frac{e_0^2}{4\pi\epsilon_0 \hbar c}}_{\alpha_f} = -\epsilon_0 c^2, \quad (4.2.6)$$

and inserting the tensor elements from (4.2.3) into (4.2.2) leads to,

$$\Theta^0_0 = \frac{\epsilon_0}{2} \left(c^2 \vec{\mathbf{B}}\vec{\mathbf{B}} + \vec{\mathbf{E}}\vec{\mathbf{E}} \right) + \frac{\alpha_f \hbar c}{4\pi} \Lambda(q_0). \quad (4.2.7)$$

Since we are considering static cases, we have no magnetic fields, $\mathcal{H}_{\text{kin}} = 0$, $\vec{\mathbf{B}} = 0$ and we get for the energy density,

$$\Theta^0_0 = \underbrace{\frac{\epsilon_0}{2} \vec{\mathbf{E}}\vec{\mathbf{E}}}_{\mathcal{H}_{\text{cur}}} + \underbrace{\frac{\alpha_f \hbar c}{4\pi} \Lambda(q_0)}_{\mathcal{H}_{\text{pot}}}. \quad (4.2.8)$$

These two components of energy will be calculated inside a cylinder with radius R and height $2Z$. Outside of this cylinder we will consider pure electrodynamics and show, that this assumption is reasonable.

4.2.1 Working in cylinder coordinates

Due to the cylindrical symmetry of a dipole configuration, we will work in cylinder coordinates for both, monopole,- and dipole configurations. Therefore we will now express the soliton field Q , the affine connection $\vec{\Gamma}_\mu$, the curvature tensor $\vec{R}_{\mu\nu}$ and the resulting energy densities in terms of cylindrical coordinates. The general soliton field (3.2.3) for any configuration in these coordinates reads¹,

$$Q(r, \phi, z) = q_0(r, z) - i\vec{\sigma}\vec{q}(r, \phi, z), \quad (4.2.9)$$

where the vector part has the form,

$$\vec{q}(r, \phi, z) = \begin{pmatrix} q_r(r, z) \cos(\phi) \\ q_r(r, z) \sin(\phi) \\ q_z(r, z) \end{pmatrix}. \quad (4.2.10)$$

By remembering the form of the affine connection $\vec{\Gamma}_\mu$ in (3.2.7) and inserting (4.2.10),

$$\vec{\Gamma}_\mu(r, \phi, z) = q_0 \partial_\mu \vec{q} - \vec{q} \partial_\mu q_0 + \vec{q} \times \partial_\mu \vec{q}, \quad (4.2.11)$$

¹Since q_0 depends only on the distance to the centre of the soliton and we are using cylindrical coordinates, q_0 does not depend on ϕ .

we obtain its three components $\vec{\Gamma}_r$, $\vec{\Gamma}_\phi$ and $\vec{\Gamma}_z$,

$$\vec{\Gamma}_r = \begin{pmatrix} (q_0 \partial_r q_r - q_r \partial_r q_0) \cos(\phi) + (q_r \partial_r q_z - q_z \partial_r q_r) \sin(\phi) \\ (q_0 \partial_r q_r - q_r \partial_r q_0) \sin(\phi) + (q_z \partial_r q_r - q_r \partial_r q_z) \cos(\phi) \\ q_0 \partial_r q_z - q_z \partial_r q_0 \end{pmatrix}, \quad (4.2.12)$$

$$\vec{\Gamma}_\phi = q_r \begin{pmatrix} -q_0 \sin(\phi) - q_z \cos(\phi) \\ q_0 \cos(\phi) - q_z \sin(\phi) \\ q_r \end{pmatrix} \quad (4.2.13)$$

$$\vec{\Gamma}_z = \begin{pmatrix} (q_r \partial_z q_z - q_z \partial_z q_r) \sin(\phi) + (q_0 \partial_z q_r - q_r \partial_z q_0) \cos(\phi) \\ (q_z \partial_z q_r - q_r \partial_z q_z) \cos(\phi) + (q_0 \partial_z q_r - q_r \partial_z q_0) \sin(\phi) \\ q_0 \partial_z q_z - q_z \partial_z q_0 \end{pmatrix}. \quad (4.2.14)$$

Now, by help of the definition, $\vec{R}_{\mu\nu} \equiv \vec{\Gamma}_\mu \times \vec{\Gamma}_\nu$, we are able to compute the components of the curvature tensor, which read,

$$\vec{R}_{\phi z} = q_r \begin{pmatrix} \partial_z q_0 \sin(\phi) + \partial_z q_z \cos(\phi) \\ -\partial_z q_0 \cos(\phi) + \partial_z q_z \sin(\phi) \\ -\partial_z q_r \end{pmatrix}, \quad (4.2.15)$$

$$\vec{R}_{zr} = \frac{\partial_r q_r \partial_z q_z - \partial_z q_r \partial_r q_z}{q_0} \begin{pmatrix} -q_0 \sin(\phi) - q_z \cos(\phi) \\ q_0 \cos(\phi) - q_z \sin(\phi) \\ q_r \end{pmatrix}, \quad (4.2.16)$$

$$\vec{R}_{r\phi} = q_r \begin{pmatrix} -\partial_r q_0 \sin(\phi) - \partial_r q_z \cos(\phi) \\ \partial_r q_0 \cos(\phi) - \partial_r q_z \sin(\phi) \\ \partial_r q_r \end{pmatrix}. \quad (4.2.17)$$

As shown in (4.2.8), the curvature energy is, $H = \epsilon_0 \int dx^3 |\vec{E}|^2/2$ and because of the relation, $\vec{E}_i \propto \vec{R}_{jk}$, we get the curvature tensor's squares,

$$\vec{R}_{\phi z}^2 = q_r^2 [(\partial_z q_0)^2 + (\partial_z q_r)^2 + (\partial_z q_z)^2], \quad (4.2.18)$$

$$\vec{R}_{zr}^2 = q_0^{-2} (\partial_r q_r \partial_z q_z - \partial_z q_r \partial_r q_z)^2, \quad (4.2.19)$$

$$\vec{R}_{r\phi}^2 = q_r^2 [(\partial_r q_0)^2 + (\partial_r q_r)^2 + (\partial_r q_z)^2], \quad (4.2.20)$$

as well as the energy contributions with the proper conversion factor to SI units and the length scales of cylinder coordinates, $l_\phi = r$ and $l_r = l_z = 1$.

$$\vec{E}_r = -\frac{e_0}{4\pi\epsilon_0} \frac{1}{l_\phi l_z} \vec{R}_{\phi z}, \quad (4.2.21)$$

$$\vec{E}_\phi = \frac{e_0}{4\pi\epsilon_0} \frac{1}{l_r l_z} \vec{R}_{rz}, \quad (4.2.22)$$

$$\vec{E}_z = -\frac{e_0}{4\pi\epsilon_0} \frac{1}{l_r l_\phi} \vec{R}_{r\phi}. \quad (4.2.23)$$

Curvature energy density

Finally we are ready to express the curvature energy density \mathcal{H}_{cur} as a function of the soliton field Q in cylindrical coordinates,

$$\begin{aligned}\mathcal{H}_{cur} &= \frac{1}{2}\epsilon_0\vec{E}_i\vec{E}_i = \frac{1}{2}\epsilon_0(\vec{E}_r^2 + \vec{E}_\phi^2 + \vec{E}_z^2) = \\ &= \frac{1}{2}\frac{\alpha_f\hbar c}{4\pi}\frac{1}{r^2}\left\{q_r^2[(\partial_z q_0)^2 + (\partial_z q_r)^2 + (\partial_z q_z)^2] + \frac{r^2}{q_0^2}(\partial_r q_r \partial_z q_z - \partial_z q_r \partial_r q_z)^2 + \right. \\ &\quad \left. + q_r^2[(\partial_r q_0)^2 + (\partial_r q_r)^2 + (\partial_r q_z)^2]\right\},\end{aligned}\tag{4.2.24}$$

where we used the definition of the fine structure constant α_f from section 2.2 and the following identity,

$$\frac{\alpha_f\hbar c}{e_0} = \frac{e_0}{4\pi\epsilon_0}.\tag{4.2.25}$$

Potential energy density

Since, the potential energy does not depend on q_r , q_ϕ or q_z , we may use the expression in (4.2.8) as well in cylindrical coordinates,

$$\mathcal{H}_{pot} = \frac{\alpha_f\hbar c}{4\pi}\frac{q_0^{2m}}{r_0^4},\tag{4.2.26}$$

where we always use $m = 3$ and therefore,

$$q_0^6 = \frac{r_0^6}{(r_0^2 + \rho^2 + z^2)^3}.\tag{4.2.27}$$

Energy contribution outside the box

We will begin with the case of a monopole centred in the origin of a cylinder. For convenience, we assume that outside this cylinder, the non-radial electric field components and the potential energy are negligible, since for far distances the model of topological fermions approaches classical electrodynamics, as described in section 3.2.6. Therefore, we begin with the electric potential of a unit charge and rewrite it in cylindrical coordinates²,

$$\Phi = \frac{1}{4\pi\epsilon_0}\frac{e_0}{|\vec{r}'|} = \frac{1}{4\pi\epsilon_0}\frac{e_0}{\sqrt{\rho^2 + z^2}}.\tag{4.2.28}$$

²To reduce confusion, we use in this section for the cylindrical radius coordinate the letter ρ and for the radial component of spherical coordinates, we write r .

The associated electric field reads,

$$\vec{E}(r) = -\nabla\Phi = \frac{e_0}{4\pi\epsilon_0} \frac{\vec{r}}{r^3} = \frac{1}{4\pi\epsilon_0} \frac{e_0}{\sqrt{(\rho^2 + z^2)^3}} \begin{pmatrix} \rho \\ 0 \\ z \end{pmatrix}. \quad (4.2.29)$$

We have to integrate $|\vec{E}|^2$ over the whole volume except the cylinder, characterised by its radius R and its half length Z . Due to the cylindrical symmetry, we get an integration factor of 2π and we are able to restrict our consideration to the r - z plane, where the cylinder gets projected to a rectangular box. We split the remaining two dimensional area into three smaller branches, which are shown in figure 4.2.1. Hence, the energy outside the box may be written,

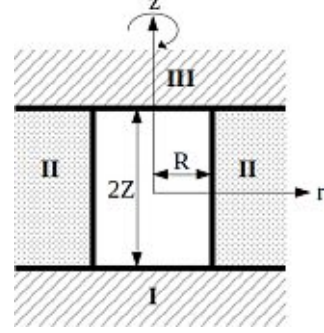


Figure 4.2.1: Integration areas.

$$\begin{aligned} H_{\text{out}} &= \frac{\epsilon_0}{2} \int_{\mathbb{R}^3 \setminus \text{box}} d^3x |\vec{E}|^2 = \frac{\epsilon_0}{2} \int_{\mathbb{R}^3 \setminus \text{box}} \rho d\rho d\varphi dz |\vec{E}|^2 = \pi\epsilon_0 \int_{\mathbb{R}^2 \setminus \text{box}} \rho d\rho dz |\vec{E}|^2 \\ &= \pi\epsilon_0 \left\{ \underbrace{\int_{-\infty}^{-Z} \int_0^{\infty} \rho d\rho dz}_{\text{I}} + \underbrace{\int_{-Z}^Z \int_R^{\infty} \rho d\rho dz}_{\text{II}} + \underbrace{\int_Z^{\infty} \int_0^{\infty} \rho d\rho dz}_{\text{III}} \right\} |\vec{E}|^2. \end{aligned} \quad (4.2.30)$$

For symmetry reasons, we see that area I and III will lead to the same value, therefore we calculate only the first one and take it twice and neglect the constant for a moment. Inserting the electric field we get,

$$H_{\text{out},I} = H_{\text{out},III} \approx \int_{-\infty}^{-Z} \int_0^{\infty} \frac{\rho}{(\rho^2 + z^2)^2} d\rho dz = \int_{-\infty}^{-Z} \int_{z^2}^{\infty} \frac{1}{2u^2} du dz = \frac{1}{2Z}, \quad (4.2.31)$$

where we have used the substitution $u(\rho, z) = \rho^2 + z^2$ to perform the radial integration over ρ . The associated differential reads, $du = 2\rho d\rho$. With the same substitution we integrate over the second area,

$$H_{\text{out},II} \approx \int_{-Z}^Z \int_R^{\infty} \frac{\rho}{(\rho^2 + z^2)^2} d\rho dz = \int_{-Z}^Z \frac{dz}{2(R^2 + z^2)}. \quad (4.2.32)$$

Taking the constants into account, we get for the sum of the three components of H_{out} as an interim result,

$$H_{\text{out}} = \pi\epsilon_0 \left(\frac{e_0}{4\pi\epsilon_0} \right)^2 \frac{1}{2} \left\{ \frac{2}{Z} + \int_{-Z}^Z \frac{dz}{R^2 + z^2} \right\}. \quad (4.2.33)$$

For the z -integration in the second term, we may use again a substitution, $z = R \tan(\alpha)$ with $dz = R(1 + \tan^2(\alpha))d\alpha$. Therefore, by using (4.2.25) again, we obtain,

$$H_{\text{out}} = \frac{e_0^2}{32\pi\epsilon_0} \left\{ \frac{2}{Z} + \frac{1}{R} \int_{\arctan(-Z/R)}^{\arctan(Z/R)} d\alpha \right\} = \frac{\alpha_f \hbar c}{4} \left(\frac{1}{Z} + \frac{1}{R} \arctan \left(\frac{Z}{R} \right) \right). \quad (4.2.34)$$

Let us do a short check, for which regime our assumption about the electrodynamic limit is reasonable. Thus, we take a look at the scalar part (3.2.30) and introduce $\eta \equiv r/r_0$ to get the relation,

$$q_0 = \frac{r_0}{\sqrt{r_0^2 + r^2}} = \frac{1}{\sqrt{\eta^2 + 1}}, \quad (4.2.35)$$

which is plotted in figure 4.2.2. Since the potential energy (3.2.18) is proportional to q_0^{2m} , we see that the potential term approaches zero relatively quickly for rising η . For a sphere of radius $r = 10r_0$ and $m = 3$ we get the following values (table 4.1) for the different energy components in- and outside a sphere, computed with the radial energy density from (3.2.31). We are considering cylindrical lattices, therefore the calculation for a sphere with radius r overestimates the energies outside, compared to a cylinder with radius r and height $z > r$. The ratio $(H_{\text{out}}^{\text{tan}} + H_{\text{out}}^{\text{pot}})/H_{\text{out}}^{\text{rad}} \approx 0.0134$, which shows, that our assumption of pure electrodynamics outside the box is fulfilled by at least 98.66%.

energies / MeV	radial	tangential	potential	Σ
inside:	0.224	0.127725	0.127725	0.47945
outside:	0.032	0.00021334	0.00021334	0.03243
			total:	≈ 0.511

Table 4.1: Compilation of the various energies in,- and outside a sphere with radius $r = 10r_0$. By comparing radial, tangential and potential energy outside the box, it can be seen that electrodynamic limit is very well approached.

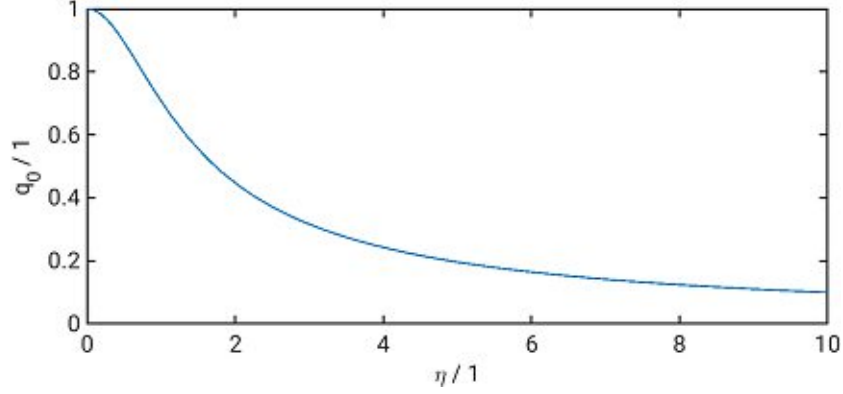


Figure 4.2.2: Plot of the scalar part q_0 as a function of the ratio $r/r_0 \equiv \eta$. Potential energy is proportional to q_0^6 .

4.2.2 Error estimation for H_{pot}

After we did the appraisal for the involved energies in- and outside a sphere, we want to go on and find an analytical expression for the potential energy outside, which we neglect in the electrodynamic limit. The potential energy density (4.2.26) reads,

$$\mathcal{H}_{\text{pot}} = \frac{\alpha_f \hbar c}{4\pi} \frac{q_0^6}{r_0^4}, \quad (4.2.36)$$

where we use $m = 3$ and write q_0 in cylindrical coordinates,

$$q_0 = \frac{r_0}{\sqrt{r_0^2 + r^2}} = \frac{r_0}{\sqrt{r_0^2 + \rho^2 + z^2}}. \quad (4.2.37)$$

The neglected potential energy outside the box yields,

$$\begin{aligned} H_{\text{pot}}^{\text{out}} &= \frac{\alpha_f \hbar c}{4\pi r_0^4} \int_{\mathbb{R}^3 \setminus \text{box}} d^3x q_0^6 = \frac{\alpha_f \hbar c}{4\pi r_0^4} \int_{\mathbb{R}^3 \setminus \text{box}} \rho d\rho d\varphi dz \frac{r_0^6}{(r_0^2 + \rho^2 + z^2)^3} = \\ &= \underbrace{\frac{\alpha_f \hbar c r_0^2}{2}}_K \int_{\mathbb{R}^2 \setminus \text{box}} \rho d\rho dz \frac{1}{(r_0^2 + \rho^2 + z^2)^3}. \end{aligned} \quad (4.2.38)$$

We split the integral in the exact same way as done in (4.2.30), getting three areas, where the upper and lower part give the same value due to symmetry. By comparing with figure 4.2.1, we get,

$$H_{\text{pot}}^{\text{out}} = K \left\{ 2 \cdot \underbrace{\int_{-\infty}^{-Z} \int_0^{\infty} \rho d\rho dz}_{\text{I, III}} + \underbrace{\int_{-Z}^Z \int_R^{\infty} \rho d\rho dz}_{\text{II}} \right\} (r_0^2 + \rho^2 + z^2)^{-3}. \quad (4.2.39)$$

The integration over ρ may be done with the substitution, $u(\rho, z) = r_0^2 + \rho^2 + z^2$ with $du = 2\rho d\rho$,

$$\begin{aligned} \mathbf{I} &= \frac{1}{2} \int_{-\infty}^{-Z} \int_{r_0^2+z^2}^{\infty} dz du u^{-3} = \frac{1}{4} \int_{-\infty}^{-Z} dz \frac{1}{(r_0^2 + z^2)^2}, \\ \mathbf{II} &= \frac{1}{4} \int_{-Z}^Z dz \frac{1}{(r_0^2 + R^2 + z^2)^2}. \end{aligned} \quad (4.2.40)$$

For the integration over z , we use another substitution, $z = r_0 \tan(\alpha)$ with $dz = r_0 / \cos^2(\alpha) d\alpha$ for the first integral,

$$\begin{aligned} \mathbf{I} &= \frac{1}{4} \int \frac{r_0}{\cos^2(\alpha)} d\alpha r_0^{-4} \underbrace{(1 + \tan^2(\alpha))^{-2}}_{\cos^4(\alpha)} = \frac{1}{4r_0^3} \int d\alpha \cos^2(\alpha) = \\ &= \frac{1}{8r_0^3} (\alpha + \sin(\alpha) \cos(\alpha)), \end{aligned} \quad (4.2.41)$$

and for the second one, we use $z = \sqrt{r_0^2 + R^2} \tan(\beta)$,

$$\begin{aligned} \mathbf{II} &= \frac{1}{4} \int \frac{\sqrt{r_0^2 + R^2}}{\cos^2(\beta)} d\beta (r_0^2 + R^2)^{-2} (1 + \tan^2(\beta))^{-2} = \\ &= \frac{1}{4(r_0^2 + R^2)^{3/2}} \int d\beta \cos^2(\beta). \end{aligned} \quad (4.2.42)$$

Substituting back to z with $\alpha = \arctan(z/r_0)$, $\beta = \arctan(z/\sqrt{r_0^2 + R^2})$ respectively and taking the integration boundaries into account, we obtain,

$$\begin{aligned} \mathbf{I} &= \frac{1}{8r_0^3} \left[\arctan\left(\frac{z}{r_0}\right) + \frac{z/r_0}{(z/r_0)^2 + 1} \right]_{-\infty}^{-Z} = \\ &= \frac{1}{8r_0^3} \left[\arctan\left(\frac{-Z}{r_0}\right) - \frac{r_0 Z}{r_0^2 + Z^2} + \frac{\pi}{2} \right], \\ \mathbf{II} &= \frac{1}{8(r_0^2 + R^2)^{3/2}} \left[\arctan\left(\frac{z}{\sqrt{r_0^2 + R^2}}\right) + \frac{z\sqrt{r_0^2 + R^2}}{r_0^2 + R^2 + z^2} \right]_{-Z}^Z = \\ &= \frac{1}{4(r_0^2 + R^2)^{3/2}} \arctan\left(\frac{Z}{\sqrt{r_0^2 + R^2}}\right). \end{aligned} \quad (4.2.43)$$

Therefore, we get for the total potential energy outside the box (4.2.39),

$$\begin{aligned} H_{\text{pot}}^{\text{out}} &= \frac{\alpha_f \hbar c r_0^2}{2} \left\{ \frac{1}{4r_0^3} \left[\arctan\left(\frac{-Z}{r_0}\right) - \frac{r_0 Z}{r_0^2 + Z^2} + \frac{\pi}{2} \right] + \right. \\ &\quad \left. + \frac{1}{4(r_0^2 + R^2)^{3/2}} \arctan\left(\frac{Z}{\sqrt{r_0^2 + R^2}}\right) \right\}. \end{aligned} \quad (4.2.44)$$

If we consider a lattice with the specifications of $Z = 10r_0$ and $R = 10r_0$, and the soliton radius, $r_0 = 2.21\text{fm}$, we find for the numerical value of the potential energy outside the box,

$$H_{\text{pot}}^{\text{out}} \approx 1.17 \cdot 10^{-4} \text{MeV}. \quad (4.2.45)$$

4.2.3 Discretization

Having gathered all energy contributions, we are now ready to go on with the discretization, which is necessary for the numerical calculations on a computer. Therefore, the soliton field Q stated in (4.2.9), with its components q_0 , q_r and q_z is only defined on discrete points of a lattice. Since q_0 acts only as the scalar part of the quaternion, we are left with a rectangular, two dimensional grid. It is characterized with the number of points in r direction n_r and the number of points in z direction n_z . The distance between two points is called lattice constant and we denote it by a .

Derivatives

To evaluate the curvature energy density \mathcal{H}_{cur} (4.2.24), we need the soliton field's derivatives of the form $\partial_i q_j$. Therefore, we introduce derivatives defined on the lattice and label the points in each of the two directions with the index i ,

$$0 \leq \dots \leq x_{i-1} \leq x_i \leq \dots \quad \text{and} \quad 0 \leq i \leq n_{r,z} \quad \text{with} \quad i, n_{r,z} \in \mathbb{N}.$$

For a general function $f(x_i)$, one can distinguish between a left,- and a right derivative,

$$\frac{df}{dx_i} \approx \left(\frac{\Delta f}{\Delta x_i} \right)_{\text{left}} = \frac{f(x_i) - f(x_{i-1})}{\Delta x_i} = \frac{f(x_i) - f(x_{i-1})}{a} \quad (4.2.46)$$

and

$$\frac{df}{dx_i} \approx \left(\frac{\Delta f}{\Delta x_i} \right)_{\text{right}} = \frac{f(x_{i+1}) - f(x_i)}{a}. \quad (4.2.47)$$

At the boundary of the box, we apply these two forms of derivative, which are approximations of first order. But whenever possible, we use enhanced formulas for derivatives, which take more neighbouring points into account. To improve accuracy, a polynomial of second order $g(x) = a_2x^2 + a_1x + a_0$ is fitted through the function values $f(x_{i-1})$, $f(x_i)$ and $f(x_{i+1})$. If we take the

derivative of that polynomial at the point x_i , we get $dg/dx_i = 2a_2x_i + a_1$, which is a second order approximation for the derivative,

$$\frac{df}{dx_i} \approx \frac{f(x_{i+1}) - f(x_{i-1}))}{2a}. \quad (4.2.48)$$

Three or more points away from the boundary, we use an even better approximation, which fits a fourth order polynomial through five neighbouring points. The derivative then reads,

$$\frac{df}{dx_i} \approx \frac{f(x_{i-2}) - 8f(x_{i-1}) + 8f(x_{i+1}) - f(x_{i+2}))}{12a}. \quad (4.2.49)$$

With these expressions, we are prepared to calculate the curvature energy density \mathcal{H}_{cur} in a numerical manner.

Energies on the lattice

Our goal is to calculate the total energy H_{tot} , therefore we want to integrate the energy densities and sum them up,

$$H_{tot} = \int_{\mathbb{R}^3} d^3x [\mathcal{H}_{cur} + \mathcal{H}_{pot}] + H_{out} = H_{in} + H_{out}. \quad (4.2.50)$$

For the numerical integration on the lattice, we have to rearrange the expressions for \mathcal{H}_{cur} and \mathcal{H}_{pot} in (4.2.24) and (4.2.26), because the coordinates r and z are not continuous any more. Hence we introduce dimensionless coordinates $\bar{r}, \bar{\varphi}, \bar{z} \in \mathbb{N}$, defined by the relations,

$$r = a\bar{r}, \quad \varphi = \bar{\varphi}, \quad z = a\bar{z}, \quad (4.2.51)$$

who just number the lattice points. By inserting (4.2.51) into the derivatives, they become,

$$\partial_r \vec{q} = \frac{1}{a} \frac{\partial \vec{q}(r, z)}{\partial \bar{r}} = \frac{1}{a} \partial_{\bar{r}} \vec{q} \equiv \frac{1}{a} \bar{\partial}_r \vec{q} \quad \text{and} \quad \partial_z \vec{q} = \frac{1}{a} \bar{\partial}_z \vec{q}. \quad (4.2.52)$$

Now, we apply these derivatives on the lattice onto \mathcal{H}_{cur} to get the curvature energy on the lattice,

$$H_{cur} = \int_{\mathbb{R}^3} d^3x \mathcal{H}_{cur} = a^3 \int_{\mathbb{R}^3} \bar{r} d\bar{r} d\bar{\varphi} d\bar{z} \mathcal{H}_{cur}, \quad (4.2.53)$$

with

$$\begin{aligned} \mathcal{H}_{cur} = \frac{1}{2} \frac{\alpha_f \hbar c}{4\pi} \frac{1}{r^2} & \left\{ q_r^2 [(\partial_z q_0)^2 + (\partial_z q_r)^2 + (\partial_z q_z)^2] + \frac{r^2}{q_0^2} (\partial_r q_r \partial_z q_z - \partial_z q_r \partial_r q_z)^2 + \right. \\ & \left. + q_r^2 [(\partial_r q_0)^2 + (\partial_r q_r)^2 + (\partial_r q_z)^2] \right\}, \end{aligned} \quad (4.2.54)$$

and consequently,

$$\begin{aligned} \mathcal{H}_{\text{cur}} = & \frac{1}{2} \frac{\alpha_f \hbar c}{4\pi} \frac{1}{a^2 \bar{r}^2} \left\{ \underbrace{\frac{q_r^2}{a^2} [(\bar{\partial}_z q_0)^2 + (\bar{\partial}_z q_r)^2 + (\bar{\partial}_z q_z)^2]}_{\bar{\mathcal{H}}_1/a^2} + \right. \\ & \left. + \underbrace{\frac{a^2 \bar{r}^2}{a^4 q_0^2} (\bar{\partial}_r q_r \bar{\partial}_z q_z - \bar{\partial}_z q_r \bar{\partial}_r q_z)^2}_{\bar{r}^2 \bar{\mathcal{H}}_2/a^2} + \underbrace{\frac{q_r^2}{a^2} [(\bar{\partial}_r q_0)^2 + (\bar{\partial}_r q_r)^2 + (\bar{\partial}_r q_z)^2]}_{\bar{\mathcal{H}}_3/a^2} \right\}. \end{aligned} \quad (4.2.55)$$

The integration over φ yields 2π and we obtain finally the curvature energy H_{cur} on the lattice,

$$\begin{aligned} H_{\text{cur}} &= \frac{2\pi}{2} \frac{\alpha_f \hbar c}{4\pi} \frac{1}{a^4} \int_{\mathbb{R}^2} \bar{r} d\bar{r} d\bar{z} \frac{1}{\bar{r}^2} \left\{ \bar{\mathcal{H}}_1 + \bar{r}^2 \bar{\mathcal{H}}_2 + \bar{\mathcal{H}}_3 \right\} = \\ &= \frac{\alpha_f \hbar c}{a} \frac{1}{4} \int_{\mathbb{R}^2} d\bar{r} d\bar{z} \underbrace{\frac{1}{\bar{r}} \left\{ \bar{\mathcal{H}}_1 + \bar{r}^2 \bar{\mathcal{H}}_2 + \bar{\mathcal{H}}_3 \right\}}_{\bar{H}_{\text{cur}}}. \end{aligned} \quad (4.2.56)$$

For the potential energy on the lattice, we perform the same derivation as done before, starting with the expression for the potential energy density (4.2.26),

$$\begin{aligned} H_{\text{pot}} &= \int_{\mathbb{R}^3} d^3x \mathcal{H}_{\text{pot}} = \frac{\alpha_f \hbar c}{4\pi r_0^4} \int_{\mathbb{R}^3} d^3x q_0^{2m} = 2\pi \frac{\alpha_f \hbar c}{4\pi a^4 \bar{r}_0^4} \int_{\mathbb{R}^2} a^3 \bar{r} d\bar{r} d\bar{z} q_0^{2m} = \\ &= \frac{\alpha_f \hbar c}{a} \frac{1}{2\bar{r}_0^4} \underbrace{\int_{\mathbb{R}^2} \bar{r} d\bar{r} d\bar{z} q_0^{2m}}_{\bar{H}_{\text{pot}}}. \end{aligned} \quad (4.2.57)$$

Therefore, the entire energy inside the box reads,

$$H_{\text{in}} = \frac{\alpha_f \hbar c}{a} \left(\bar{H}_{\text{cur}} + \bar{H}_{\text{pot}} \right). \quad (4.2.58)$$

Here, we want to emphasize again, that quantities with a bar over them are always dimensionless as can be seen in (4.2.58), because α_f has no dimension, $\hbar c \approx 200 \text{ MeV fm}$ and a measures the distance between two neighbouring points in fm.

Secondly, we want to highlight that α_f acts here just as a conversion factor and it is perfectly okay to see it as a constant for this purpose. Later, we will show, that the force of attraction in a dipole varies with the momentum q^2 , respectively with the distance between the two poles, which may be interpreted as a running of the coupling constant $\alpha_f = \alpha_f(q^2)$.

Last, but not least we express the energy outside the box, H_{out} , in terms of dimensionless units, \bar{R} and \bar{Z} , who are defined by $R = a\bar{R}$ and $Z = a\bar{Z}$. R denotes the radius and Z is half of the height of our considered cylinder placed around the origin. Recapitulating (4.2.34) and insert these relations, we get,

$$H_{\text{out}} = \frac{\alpha_f \hbar c}{4} \left(\frac{1}{\bar{Z}} + \frac{1}{\bar{R}} \arctan \left(\frac{\bar{Z}}{\bar{R}} \right) \right) = \frac{\alpha_f \hbar c}{a} \underbrace{\frac{1}{4} \left(\frac{1}{\bar{Z}} + \frac{1}{\bar{R}} \arctan \left(\frac{\bar{Z}}{\bar{R}} \right) \right)}_{\bar{H}_{\text{out}}}. \quad (4.2.59)$$

Thus, we obtain for the total energy of the simulation,

$$H_{\text{tot}} = H_{\text{in}} + H_{\text{out}} = \frac{\alpha_f \hbar c}{a} \left(\bar{H}_{\text{cur}} + \bar{H}_{\text{pot}} + \bar{H}_{\text{out}} \right) = \frac{\alpha_f \hbar c}{a} \bar{H}_{\text{tot}}. \quad (4.2.60)$$

Note, that the way of computing the total energy and minimizing this function is called GAMMA action. Another method is WILSON action, which provides a discretized version of computing the total action S on a lattice. In our static consideration, WILSON action provides only an other method to compute the curvature energy H_{cur} as stated in the next section. We will use this second routine to check our calculation of the total energy. In addition, we are able to compare both methods with the analytical solution for a monopole, which is done in section 6.2.

4.3 Wilson action

Before we derive an expression for the WILSON action on the lattice for the MTF, we want to give a short overview about lattice QCD[15] and apply the presented concepts onto the MTF later.

4.3.1 The QCD action in the continuum

Quarks and gluon fields

In QCD quarks are described by DIRAC spinors $\psi_{c\alpha}^f(x)$ at every point x in the MINKOWSKI spacetime. Here, $f \in \{u, d, s, c, b, t\}$ indicates the flavour, $c \in \{\text{blue, red, green}\}$ the colour component and $\alpha \in \{1, 2, 3, 4\}$ the spinor component.

Taking the DIRAC equation, $(i\gamma^\mu \partial_\mu - m)\psi_{c\alpha}^f(x) = 0$ and making it invariant under local rotations in the colour space, also called gauge transformations, we have to introduce gauge fields of the form $\mathcal{A}_\mu(x)_{cd}$ associated with the gluons, the gauge bosons of QCD. The index μ in $\mathcal{A}_\mu(x)_{cd}$ indicates, that it is a vector field. The colour indices cd , make clear, that for each x and μ , the gauge field is a 3×3 matrix, which has to be hermitian and traceless. By dropping all non-MINKOWSKI indices for a while, a rotation of the spinor in colour space reads,

$$\psi(x) \rightarrow \psi(x)' = \exp(i\theta^a(x)t_a) \psi(x) = \Omega(x) \psi(x), \quad (4.3.1)$$

where $t_a = \frac{\lambda_a}{2}$ and λ_a are the GELL-MANN matrices with $a \in \{1, 2, \dots, 8\}$. We demand the DIRAC equation to be invariant under this transformation. Inserting ψ' into the DIRAC equation, leads to,

$$i\gamma^\mu \overbrace{(\partial_\mu + i t_a \partial_\mu \theta^a)}^{\mathcal{D}_\mu} \psi - m\psi = 0, \quad (4.3.2)$$

which is gauge invariant, if the introduced gauge field $\mathcal{A}_\mu = \sum_{a=1}^8 A_\mu^a t_a$ transforms like,

$$A_\mu^a \rightarrow A_\mu^{a'} = A_\mu^a - \partial_\mu \theta^a + f_{abc} \theta^a A_\mu^b, \quad (4.3.3)$$

where f_{abc} are the structure constants of the group $\text{SU}(3)$. $\mathcal{D}_\mu \equiv \partial_\mu + i\mathcal{A}_\mu$ is called *covariant derivative*.

For convenience, the total action may be divided into three parts, namely the fermionic, the interaction and the gluon component.

Fermion action

$S_F[\psi, \bar{\psi}, \mathcal{A}]$ is called the fermionic QCD action and is given by,

$$S_F[\psi, \bar{\psi}, \mathcal{A}] = \sum_{f=1}^6 \int d^4x \bar{\psi}^f (\gamma^\mu (\partial_\mu + i\mathcal{A}_\mu) + m^f) \psi^f, \quad (4.3.4)$$

using EINSTEIN summation. Dropping the sum for over the various flavours for convenience, we are left with,

$$S_F[\psi, \bar{\psi}, \mathcal{A}] = \int d^4x \underbrace{\bar{\psi} (\gamma^\mu (\partial_\mu + i\mathcal{A}_\mu) + m) \psi}_{\text{Lagrangian } \mathcal{L}}, \quad (4.3.5)$$

and applying the EULER-LAGRANGE equations of motion by deriving \mathcal{L} with respect to $\bar{\psi}$, we get back the gauge invariant DIRAC equation.

Gauge invariance of the fermion action

In electrodynamics the action is invariant under a local phase transformation, of the form $\exp(i e_0 \phi(x))$. These transformations form the group $\mathbf{U}(\mathbf{1})$, the associated generator would be simply 1. As already mentioned, in QCD, gauge transformations $\Omega(x)$ are traceless, 3×3 matrices with $\det[\Omega(x)] = 1$ and $\Omega(x)^\dagger = \Omega(x)^{-1}$, defining the special unitary group $\mathbf{SU}(\mathbf{3})$ with the GELL-MANN matrices as generators. Since these matrices do not commute, they are called *non-abelian*, associated gauge theories are referred to as YANG-MILLS theories.

Now we want to show the gauge invariance of the fermionic action, $S_F[\psi', \bar{\psi}', \mathcal{A}'] = S_F[\psi, \bar{\psi}, \mathcal{A}]$. Using (4.3.1) and inserting it into (4.3.5), yields,

$$S_F[\psi', \bar{\psi}', \mathcal{A}'] = \int d^4x \bar{\psi} \Omega^\dagger (\gamma^\mu (\partial_\mu + i\mathcal{A}'_\mu) + m) \Omega \psi. \quad (4.3.6)$$

For the mass term, the matrices Ω cancel, since $\Omega^\dagger = \Omega^{-1}$. Comparing (4.3.5) with (4.3.6), we find,

$$\partial_\mu + i\mathcal{A}_\mu = \Omega^\dagger (\partial_\mu + i\mathcal{A}'_\mu) \Omega, \quad (4.3.7)$$

and therefore the transformation for the gauge field reads,

$$\mathcal{A}_\mu \rightarrow \mathcal{A}'_\mu = \Omega \mathcal{A}_\mu \Omega^\dagger + i(\partial_\mu \Omega) \Omega^\dagger. \quad (4.3.8)$$

The gluon action

The gluon action $S_G[\mathcal{A}_\mu] = S_G[\mathcal{A}'_\mu]$ has to be invariant under transformations of the form (4.3.8). To obtain an action, we use the already introduced covariant derivative,

$$\mathcal{D}_\mu(x) = \partial_\mu + i\mathcal{A}_\mu(x). \quad (4.3.9)$$

By use of (4.3.7), we are able to read off the transformation behaviour of the covariant derivative to be,

$$\mathcal{D}_\mu \rightarrow \mathcal{D}'_\mu = \partial_\mu + i\mathcal{A}'_\mu = \Omega\mathcal{D}_\mu\Omega^\dagger. \quad (4.3.10)$$

Hence, $\mathcal{D}_\mu(x)\psi(x)$ and $\psi(x)$ transform in exactly the same way – they transform covariant.

Now we are able to define the *field strength tensor* $\mathcal{F}_{\mu\nu}$, in a generalized form of electrodynamics,

$$\mathcal{F}_{\mu\nu}(x) \equiv -i[\mathcal{D}_\mu(x), \mathcal{D}_\nu(x)] = \underbrace{\partial_\mu\mathcal{A}_\nu(x) - \partial_\nu\mathcal{A}_\mu(x)}_{\text{QED}} + i[\mathcal{A}_\mu(x), \mathcal{A}_\nu(x)], \quad (4.3.11)$$

$\underbrace{\hspace{15em}}_{\text{QCD}}$

who transforms like,

$$\mathcal{F}_{\mu\nu} \rightarrow \mathcal{F}'_{\mu\nu} = \Omega\mathcal{F}_{\mu\nu}\Omega^\dagger. \quad (4.3.12)$$

Therefore, $\text{Tr}[\mathcal{F}_{\mu\nu}\mathcal{F}^{\mu\nu}]$ is a gauge invariant quantity as one may easily check, by using the cyclic permutation inside the trace and in addition it is a LORENTZ scalar, because of the contracting indices. These are precisely the characteristics, which we need for an action,

$$S_G[\mathcal{A}] = \frac{1}{2g^2} \int d^4x \text{Tr}[\mathcal{F}_{\mu\nu}\mathcal{F}^{\mu\nu}]. \quad (4.3.13)$$

Here, g is the coupling constant, which was neglected up to now, $\mathcal{D}_\mu = \partial_\mu + ig\mathcal{A}_\mu$ and the factor $1/2$ arrives just of convention.

Colour components

The \mathcal{A}_μ are in the LIE-algebra $\mathfrak{su}(3)$, thus they can be written as,

$$\mathcal{A}_\mu(x) = \sum_{a=1}^8 A_\mu^a(x)t_a, \quad (4.3.14)$$

where the t_a form a basis for traceless, hermitian 3×3 matrices. Writing the field strength tensor in its components, we get,

$$\mathcal{F}_{\mu\nu} = \sum_{a=1}^8 (\partial_\mu A_\nu^a - \partial_\nu A_\mu^a) t_a + i \sum_{a,b=1}^8 A_\mu^a A_\nu^b \underbrace{[t_a, t_b]}_{if_{abc}t_c}, \quad (4.3.15)$$

where f_{abc} are the structure constants of $\mathbf{SU}(3)$. Using $\mathcal{F}_{\mu\nu} = \sum_{a=1}^8 F_{\mu\nu}^a t_a$, we may write,

$$F_{\mu\nu}^a = \partial_\mu A_\nu^a - \partial_\nu A_\mu^a - f_{abc} A_\mu^b A_\nu^c. \quad (4.3.16)$$

Inserting this expression into (4.3.13) leads to,

$$S_G[\mathcal{A}] = \frac{1}{4g^2} \sum_{a=1}^8 \int d^4x F_{\mu\nu}^a F_a^{\mu\nu}. \quad (4.3.17)$$

From this result, we see, that the gluon action looks like the sum of eight action terms, known from electrodynamics. However, the big difference is the commutator term in (4.3.16), who gives rise to self interaction of gluons, whereas photons never interact with each other.

4.3.2 Naive discretization of fermions

We introduce a four-dimensional lattice Λ ,

$$\Lambda = \{n = (n_1, n_2, n_3, n_4) | n_1, n_2, n_3 = 0, 1, \dots, N-1; n_4 = 0, 1, \dots, N_T-1\}, \quad (4.3.18)$$

where $n \in \Lambda$ labels the points in space-time, who are separated by an equidistant length a . To carry on, we take a look on the fermion action, with no gauge field,

$$S_F^0[\psi, \bar{\psi}] = \int d^4x \bar{\psi}(x) (\gamma^\mu \partial_\mu + m) \psi(x). \quad (4.3.19)$$

To discretize this expression, we have to replace $\psi(x)$ with $\psi(n)$ and find a discrete version for the derivative,

$$\partial_\mu \psi(x) \rightarrow \frac{1}{2a} (\psi(n + \hat{\mu}) - \psi(n - \hat{\mu})). \quad (4.3.20)$$

The integral gets simply replaced by the sum over the lattice points and a scaling factor a^4 ,

$$S_F^0[\psi, \bar{\psi}] = a^4 \sum_{n \in \Lambda} \bar{\psi}(n) \left(\gamma^\mu \frac{\psi(n + \hat{\mu}) - \psi(n - \hat{\mu})}{2a} + m \psi(n) \right). \quad (4.3.21)$$

Gauge fields as link variables

The requirement of the action to be invariant under local rotations in colour space enforced the introduction of gauge fields as shown before. We need the same characteristics on the lattice, therefore we have a matrix $\Omega(n) \in \mathbf{SU}(3)$ at each lattice point,

$$\psi(n) \rightarrow \psi'(n) = \Omega(n) \psi(n). \quad (4.3.22)$$

The mass term in (4.3.21) is again invariant under this transformation and for the other term we find the relation,

$$\bar{\psi}(n)\psi(n + \hat{\mu}) \rightarrow \bar{\psi}'(n)\psi'(n + \hat{\mu}) = \bar{\psi}(n)\Omega(n)^\dagger\Omega(n + \hat{\mu})\psi(n + \hat{\mu}), \quad (4.3.23)$$

which is not gauge invariant, unfortunately. Hence, we introduce a field $U_\mu(n)$ with the defined transformation behaviour,

$$U_\mu(n) \rightarrow U'_\mu(n) \equiv \Omega(n)U_\mu(n)\Omega(n + \hat{\mu})^\dagger, \quad (4.3.24)$$

making the expression,

$$\bar{\psi}'(n)U'_\mu(n)\psi'(n + \hat{\mu}) = \bar{\psi}(n)\Omega(n)^\dagger U'_\mu(n)\Omega(n + \hat{\mu})\psi(n + \hat{\mu}), \quad (4.3.25)$$

gauge invariant. The directional index μ of the new field U_μ makes clear, that this is a vector like quantity and therefore defined on the links of the lattice. Hence, $U_\mu(n)$ is called the *link variable* and connects the points n and $n + \hat{\mu}$.

It is mentionable, that in the discrete version, we introduced the gluon fields U_μ as elements of the $\mathbf{SU}(3)$, whereas in the continuum they lived in the LIE-algebra $\mathbf{su}(3)$.

Now we are able to incorporate the introduced gluon fields, U_μ into (4.3.21) and find the so called *naive fermion action* on the lattice,

$$S_F[\psi, \bar{\psi}] = a^4 \sum_{n \in \Lambda} \bar{\psi}(n) \left(\gamma^\mu \frac{U_\mu(n)\psi(n + \hat{\mu}) - U_{-\mu}(n)\psi(n - \hat{\mu})}{2a} + m\psi(n) \right), \quad (4.3.26)$$

which respects the invariance under gauge transformations, $S_F[\psi, \bar{\psi}, U] = S_F[\psi', \bar{\psi}', U']$.

Link variables and the continuum gauge fields

Our goal now is to find a relation between the link variables and the continuum gauge field, we begin with the gauge transformation in continuous space-time,

$$\psi(x) \rightarrow \psi(x)' = \Omega(x) \psi(x). \quad (4.3.27)$$

Because $\Omega(x)$ is a local gauge transformation, it depends on the position x . The same vector ψ is transformed at $x + dx$ in a different way. Therefore, we introduce the term parallelism. We demand two parallel vectors $\psi_1(x)$ and $\psi_2(x + dx)$, to stay parallel under a gauge transformation. To do so, we need the gauge fields \mathcal{A}_μ to define a parallel transport,

$$\psi_2(x + dx) = [\mathbb{1} + i\mathcal{A}^\mu(x)dx_\mu] \psi_1(x) = V(x, dx_\mu) \psi_1(x). \quad (4.3.28)$$

After gauge transformation, (4.3.28) reads,

$$\psi'_2(x + dx) = [\mathbb{1} + i\mathcal{A}'^\mu(x)dx_\mu] \psi'_1(x). \quad (4.3.29)$$

From the last two equations, we are able to extract the transformation behaviour of A_μ and we find it to be in accordance with (4.3.8).

For a finite parallel transport along a curve \mathcal{C} , defined by,

$$\mathcal{C}_x^y = \{s^\mu(t) | 0 \leq t \leq 1, s^\mu(0) = x^\mu, s^\mu(1) = y^\mu\}, \quad (4.3.30)$$

we get the total parallel transporter as the consecutive application of infinitesimal transporters,

$$\begin{aligned} \psi_2(y) &= V_x^y \psi_2(x) = \\ &= \lim_{N \rightarrow \infty} \prod_{n=N}^1 \left\{ \underbrace{\mathbb{1} + i\mathcal{A}^\mu \left(\frac{s(n-1)}{N} \right)}_{\text{argument of } \mathcal{A}^\mu} \underbrace{\left[\frac{s_\mu n}{N} - \frac{s_\mu(n-1)}{N} \right]}_{\text{infinitesimal element}} \right\} \psi_2. \end{aligned} \quad (4.3.31)$$

By help of the path order operator \mathcal{P} , we write V_x^y as,

$$V_x^y = \mathcal{P} \exp \left\{ i \int_{\mathcal{C}_x^y} \mathcal{A}^\mu(x) dx_\mu \right\}, \quad (4.3.32)$$

with the same transformation property as we had for the link variable $U_\mu(n)$ in (4.3.24),

$$\psi'_2 = \Omega(x + dx) V_x^y \psi_1 = V_x^{y'} \Omega(x) \psi_1 \quad \implies \quad V_x^{y'} = \Omega(x + dx) V_x^y \Omega^\dagger(x). \quad (4.3.33)$$

Therefore, we interpret the link variable $U_\mu(n)$ as the lattice version of the parallel transporter $V_n^{n+\hat{\mu}}$ and obtain,

$$U_\mu(n) = \exp \left(ia\mathcal{A}_\mu(n) \right), \quad (4.3.34)$$

where we set dx_μ to a in comparison with (4.3.28).

Wilson gauge action

Before we introduce the gluon action on the lattice, we need gauge invariant quantities to form it, hence we consider a string of link variables along a path \mathcal{P} from n_0 to n_1 ,

$$P[U] = U_{\mu_0}(n_0)U_{\mu_1}(n_0 + \hat{\mu}_0)\dots U_{\mu_{k-1}}(n_1 - \hat{\mu}_{k-1}) \equiv \prod_{(n,\mu) \in \mathcal{P}} U_\mu(n), \quad (4.3.35)$$

which is the lattice version of (4.3.32). Inserting the transformation behaviour of U_μ along the whole path, we are left with,

$$P[U] \rightarrow P[U'] = \Omega(n_0)P[U]\Omega(n_1)^\dagger, \quad (4.3.36)$$

because all matrices Ω and Ω^\dagger cancel each other in between the path. Only at the start- and endpoint they stay. We can get rid of them too, by closing the path, getting a closed loop \mathcal{L} and obtaining a gauge invariant object. After that, we may take the trace to obtain a scalar quantity,

$$L[U] = \text{Tr} \left[\prod_{(n,\mu) \in \mathcal{L}} U_\mu(n) \right] = L[U']. \quad (4.3.37)$$

To construct the gluon action, we use the shortest possible loop on the lattice, which is called *plaquette*. It forms a square on the lattice with base length a . The *plaquette variable* $U_{\mu\nu}(n)$ is defined by the consecutive application of four link variables around a plaquette,

$$U_{\mu\nu}(n) = U_\mu(n)U_\nu(n + \hat{\mu})U_\mu(n + \hat{\nu})^\dagger U_\nu^\dagger. \quad (4.3.38)$$

WILSON's form of the gauge action is given by using all plaquette variables on the lattice,

$$S_G[U] = \frac{2}{g^2} \sum_{n \in \Lambda} \sum_{\mu < \nu} \text{Re} \text{Tr} (\mathbb{1}_3 - U_{\mu\nu}(n)). \quad (4.3.39)$$

As a last point we want to show, that in the continuous limit, $a \rightarrow 0$, we get back the continuous gauge action in (4.3.13). Therefore, we expand $U_\mu = \exp(ia\mathcal{A}_\mu)$ for small a and make use of the BAKER-CAMPBELL-HAUSDORFF formula³ to compute the plaquette variable. By neglecting terms of order a^3

³

$$\exp(A)\exp(B) = \exp\left(A + B + \frac{1}{2}[A, B] + \dots\right) \quad (4.3.40)$$

and after a lengthy rearranging we obtain,

$$\begin{aligned} U_{\mu\nu}(n) &= \exp \left(ia^2 (\partial_\mu \mathcal{A}_\nu(n) - \partial_\nu \mathcal{A}_\mu(n)) + i[\mathcal{A}_\mu(n), \mathcal{A}_\nu(n)] \right) = \\ &= \exp \left(ia^2 \mathcal{F}_{\mu\nu}(n) + \mathcal{O}(a^3) \right) \approx \mathbb{1} + ia^2 \mathcal{F}_{\mu\nu}(n) - \frac{1}{2} a^4 \mathcal{F}_{\mu\nu}^2(n). \end{aligned} \quad (4.3.41)$$

Inserting this result into (4.3.39), we find,

$$\begin{aligned} S_G[U] &= \frac{2}{g^2} \sum_{n \in \Lambda} \sum_{\mu < \nu} \text{Re} \text{Tr} \left(-ia^2 \mathcal{F}_{\mu\nu}(n) + \frac{1}{2} a^4 \mathcal{F}_{\mu\nu}^2(n) \right) = \\ &= \frac{a^4}{2g^2} \sum_{n \in \Lambda} \sum_{\mu, \nu} \text{Tr}[\mathcal{F}_{\mu\nu}^2(n)] + \mathcal{O}(a^2). \end{aligned} \quad (4.3.42)$$

The second order term in a vanishes because $F_{\mu\nu}$ is traceless and hence every plaquette may be uniquely defined by exactly 2 links, the factor $1/2$ arrives in (4.3.42) by changing the sum from plaquettes p to the space-time indices μ, ν . The sum over the lattice points, together with a^4 is just the continuous version of the integral $\int d^4x$,

$$\lim_{a \rightarrow 0} S_G[U] = \lim_{a \rightarrow 0} \frac{a^4}{2g^2} \sum_{n \in \Lambda} \sum_{\mu, \nu} \text{Tr}[\mathcal{F}_{\mu\nu}^2(n)] = \frac{1}{2g^2} \int d^4x \text{Tr}[\mathcal{F}_{\mu\nu} \mathcal{F}^{\mu\nu}] = S_G[\mathcal{A}], \quad (4.3.43)$$

which shows, that we get back the continuous version of the gluon action from (4.3.13).

To do QCD on the lattice, we would have to go deeper into the formalism and get rid of the naive discretization of the fermion fields, which we cared not to much up to now. The reason therefore is, that our MTF only needs the "gluonic" part of the QCD formalism, since it has no fermion fields in its description.

4.3.3 MTF on the lattice

Our starting point to find an expression for the gauge action on the lattice for the MTF is formula (4.3.39). There we see, that we need the parallel transporter U_μ . According to (3.2.5), a soliton field $Q(x^\mu)$ gets transported to the point $(x^\mu + dx^\mu)$ by,

$$Q(x^\mu + dx^\mu) = \exp \left\{ -i \vec{\sigma} \vec{\Gamma}_\mu(x^\mu) dx^\mu \right\} Q(x^\mu) = W(x^\mu, dx^\mu) Q(x^\mu). \quad (4.3.44)$$

Therefore the parallel transporter in this case is $W(x^\mu, dx^\mu)$. For reasons to be cleared later, we introduce another vector field $\vec{A}_\mu = 2\vec{\Gamma}_\mu$ and may write,

$$W(x^\mu, dx^\mu) = \exp \left\{ -i \vec{\sigma} \vec{\Gamma}_\mu dx^\mu \right\} = \exp \left\{ -i \frac{\vec{\sigma}}{2} \vec{A}_\mu dx^\mu \right\}. \quad (4.3.45)$$

We use the generators of the group $\mathbf{SU}(2)$, which are half of the PAULI matrices, $\sigma/2$, to define \mathcal{A}_μ for the MTF,

$$\mathcal{A}_\mu \equiv \frac{\vec{\sigma}}{2} \vec{A}_\mu. \quad (4.3.46)$$

Starting at any soliton field $Q(x^\mu)$ and applying four parallel transporters W_i around a closed loop, we have to arrive at the same matrix $Q(x^\mu)$. This leads to the constraint⁴,

$$\mathbb{1} = W_1 W_2 W_3 W_4 \equiv W_{\mu\nu}. \quad (4.3.47)$$

By extending $W(x^\mu, dx^\mu)$ in (4.3.45) up to second order and inserting it into (4.3.47), we arrive at the requirement for $\mathcal{A}^\mu(x)$,

$$\mathbb{1} = \mathbb{1} - idx_\mu dy_\nu \{ \partial^\mu \mathcal{A}^\nu(x) - \partial^\nu \mathcal{A}^\mu(x) + i[\mathcal{A}^\mu(x), \mathcal{A}^\nu(x)] \}, \quad (4.3.48)$$

where terms $\propto \mathcal{O}(dx^3)$ were discarded. We see easily, that the expression in curved brackets has to be zero,

$$\partial^\mu \mathcal{A}^\nu(x) - \partial^\nu \mathcal{A}^\mu(x) + i[\mathcal{A}^\mu(x), \mathcal{A}^\nu(x)] = 0. \quad (4.3.49)$$

The commutator in (4.3.49) may be written as,

$$[\mathcal{A}^\mu, \mathcal{A}^\nu] = \left[\frac{\vec{\sigma}}{2} \vec{A}^\mu, \frac{\vec{\sigma}}{2} \vec{A}^\nu \right] = \frac{1}{4} A_a^\mu A_b^\nu \underbrace{[\sigma_a, \sigma_b]}_{2i\epsilon_{abc}\sigma_c} = \frac{i}{2} A_a^\mu A_b^\nu \epsilon_{abc} \sigma_c = \frac{i}{2} \vec{\sigma} \cdot (\vec{A}^\mu \times \vec{A}^\nu) \quad (4.3.50)$$

Hence we get for equation (4.3.49),

$$\partial^\mu \frac{\vec{\sigma}}{2} \vec{A}^\nu - \partial^\nu \frac{\vec{\sigma}}{2} \vec{A}^\mu - \frac{1}{2} \vec{\sigma} \cdot (\vec{A}^\mu \times \vec{A}^\nu) = 0, \quad (4.3.51)$$

or,

$$\partial^\mu \vec{A}^\nu - \partial^\nu \vec{A}^\mu - (\vec{A}^\mu \times \vec{A}^\nu) = 0. \quad (4.3.52)$$

Inserting $\vec{A}^\mu = 2\vec{\Gamma}^\mu$ and we get the restriction in terms of $\vec{\Gamma}_\mu$,

$$\partial^\mu \vec{\Gamma}^\nu - \partial^\nu \vec{\Gamma}^\mu = 2\vec{\Gamma}^\mu \times \vec{\Gamma}^\nu, \quad (4.3.53)$$

which is the MAURER-CARTAN equation, already established in (3.2.10). It is an additional constraint to the affine connection $\vec{\Gamma}_\mu$. It guarantees

⁴For calculations, it is more simple to use an equivalent form of (4.3.47), which reads $W_1 W_2 = W_4^\dagger W_3^\dagger$.

the uniqueness of the soliton field $Q(x^\mu)$ and makes $\exp\left(-i \int_{x_0}^{x_1} \vec{\sigma} \vec{\Gamma}_\mu dx^\mu\right)$ ⁵ integrate able, which means that the integration only depends on start- and end point.

We remember, how the curvature tensor in (3.2.8) was defined and use the just received MAURER-CARTAN equation to find the following relation for the curvature tensor,

$$\vec{R}_{\mu\nu} \equiv \vec{\Gamma}_\mu \times \vec{\Gamma}_\nu = \frac{1}{2} \left(\partial_\mu \vec{\Gamma}_\nu(x) - \partial_\nu \vec{\Gamma}_\mu(x) \right) = \underbrace{\partial_\mu \vec{\Gamma}_\nu - \partial_\nu \vec{\Gamma}_\mu}_{2\vec{R}_{\mu\nu}} - \underbrace{\vec{\Gamma}_\mu \times \vec{\Gamma}_\nu}_{\vec{R}_{\mu\nu}} = \vec{R}_{\mu\nu}. \quad (4.3.56)$$

Because of the form of equation (4.3.56), we may suspect, that we have to use another parallel transporter, namely $U = \sqrt{\vec{W}}$ and apply it around a closed loop to get the curvature tensor. Let us do the check explicitly and begin with,

$$U(x^\mu, dx^\mu) = \exp \left\{ -i \frac{\vec{\sigma}}{2} \vec{\Gamma}_\mu dx^\mu \right\} \quad (4.3.57)$$

For convenience, we introduce two abbreviations once more,

$$\mathcal{G}_\mu \equiv \frac{\vec{\sigma}}{2} \vec{\Gamma}_\mu \quad \text{and} \quad \mathcal{R}_{\mu\nu} \equiv \frac{\vec{\sigma}}{2} \vec{R}_{\mu\nu}. \quad (4.3.58)$$

Calculating again the plaquette variable around a square as done before leads to,

$$\begin{aligned} U_{\mu\nu} &= U_1 U_2 U_3 U_4 = \\ &= \mathbb{1} - i \mathcal{R}^{\mu\nu} dx_\mu dy_\nu = \mathbb{1} - i dx_\mu dy_\nu \{ \partial^\mu \mathcal{G}^\nu(x) - \partial^\nu \mathcal{G}^\mu(x) + i[\mathcal{G}^\mu(x), \mathcal{G}^\nu(x)] \}, \end{aligned} \quad (4.3.59)$$

where we are able to read off the curvature tensor in fundamental representation,

$$\mathcal{R}^{\mu\nu} = \partial^\mu \mathcal{G}^\nu(x) - \partial^\nu \mathcal{G}^\mu(x) + i[\mathcal{G}^\mu(x), \mathcal{G}^\nu(x)]. \quad (4.3.60)$$

⁵ The change of $Q(x_0)$ along a path from x_0 to x_1 results as a sequence of infinitesimal parallel transports,

$$Q(x_1) = \lim_{N \rightarrow \infty} \prod_{n=N}^1 \left\{ 1 - i \vec{\sigma} \vec{\Gamma}_\mu \left(x_0 + \frac{x_1 - x_0}{N} (n-1) \right) \frac{x_1 - x_0}{N} \right\} Q(x_0). \quad (4.3.54)$$

The product may be written formally as an exponential function,

$$Q(x_1) = \mathcal{P} \exp \left\{ -i \int_{x_0}^{x_1} \vec{\sigma} \vec{\Gamma}_\mu(x) dx^\mu \right\} Q(x_0), \quad (4.3.55)$$

where the so called path-ordering operator \mathcal{P} is used. It guarantees the interchangeability of the matrices $\vec{\sigma} \vec{\Gamma}_\mu(x)$, by arranging the products in (4.3.54) with respect to their arguments x_i .

If we compute the commutator in the last equation, we get the curvature tensor finally, as obtained in (4.3.56),

$$\vec{R}_{\mu\nu} = \partial_\mu \vec{\Gamma}_\nu - \partial_\nu \vec{\Gamma}_\mu - \vec{\Gamma}_\mu \times \vec{\Gamma}_\nu. \quad (4.3.61)$$

Therefore we see the need of taking the factor $1/2$ into account and continue with the parallel transporter $U = \exp(-i\vec{\sigma}\vec{\Gamma}_\mu dx^\mu/2)$.

To do the numerics it is more simple to work with the soliton field $Q(x^\mu)$ instead of the connection $\vec{\Gamma}_\mu$. Therefore, we use (4.3.57) and a discretized version of equation $\partial_\mu Q = -i\vec{\Gamma}_\mu \vec{\sigma} Q$ from (4.3.44) to find a relation between U and Q ,

$$-i\vec{\Gamma}_\mu \vec{\sigma} Q(x^\mu) = \partial_\mu Q(x^\mu) \approx \frac{Q(x^\mu + a\hat{\mu}) - Q(x^\mu)}{a^\mu}. \quad (4.3.62)$$

We multiply the last equation with $a^\mu Q^\dagger(x)$ and obtain,

$$Q(x^\mu + a\hat{\mu})Q^\dagger(x^\mu) \approx \mathbb{1} - ia^\mu \vec{\Gamma}_\mu \vec{\sigma} \approx \exp\{-ia^\mu \vec{\Gamma}_\mu \vec{\sigma}\}. \quad (4.3.63)$$

By comparison of (4.3.57) with (4.3.63), where we identify a^μ with dx^μ , we are able to see that the parallel transporter yields in terms of the soliton field and first order,

$$U(x^\mu, \hat{\mu}) \approx \sqrt{Q(x^\mu + a\hat{\mu})Q^\dagger(x^\mu)}. \quad (4.3.64)$$

Wilson action and curvature energy

While (4.3.64) builds the base for the numerical computation, we want to go on and show, that the action $S_G[U]$ in (4.3.39) is in a *static* consideration the curvature energy times the lattice constant, aH_{cur} . Therefore the two methods, GAMMA- and WILSON action are comparable regarding the curvature energy. To show that claim, we look for the analytical expression of the overall plaquette action $S_G[U]$ and start therefore with (4.3.59),

$$U_{\mu\nu} \equiv U_1 U_2 U_3 U_4 = \exp\left\{-ia^2 \vec{R}_{\mu\nu} \frac{\vec{\sigma}}{2}\right\}, \quad (4.3.65)$$

where we set $dx_\mu dy_\nu = a^2$, since we go round a plaquette. Also the space-time indices μ, ν are to be seen as discretized, labelling the links. For the MTF – a **SU(2)** theory – we change the term "gluon action" to curvature

action,

$$\begin{aligned} S_G[U] \rightarrow S_{\text{cur}}[U] &= \frac{2}{g^2} \sum_{n \in \Lambda} \sum_{\mu < \nu} \text{Tr}(\mathbb{1}_2 - U_{\mu\nu}(n)) = \frac{4}{g^2} \sum_{n \in \Lambda} \sum_{\mu < \nu} \left(1 - \frac{1}{2} \text{Tr} U_{\mu\nu}(n)\right) \\ &= \frac{4}{g^2} \sum_{n \in \Lambda} \sum_{\mu < \nu} \left[1 - \frac{1}{4} (\text{Tr} U_{\mu\nu} + \text{Tr} U_{\mu\nu}^\dagger)\right] \end{aligned} \quad (4.3.66)$$

Inserting the concrete form of $U_{\mu\nu}$ expanded up to second order,

$$\begin{aligned} U_{\mu\nu} &= \mathbb{1} - \frac{1}{2} i a^2 \vec{R}_{\mu\nu} \vec{\sigma} - \frac{1}{8} a^4 (\vec{R}_{\mu\nu} \vec{\sigma})^2 + \mathcal{O}(a^6), \\ U_{\mu\nu}^\dagger &= \mathbb{1} + \frac{1}{2} i a^2 \vec{R}_{\mu\nu} \vec{\sigma} - \frac{1}{8} a^4 (\vec{R}_{\mu\nu} \vec{\sigma})^2 + \mathcal{O}(a^6). \end{aligned} \quad (4.3.67)$$

$$\text{Tr} U_{\mu\nu} + \text{Tr} U_{\mu\nu}^\dagger = \text{Tr} \left[2 \cdot \mathbb{1} - \frac{1}{4} a^4 (\vec{R}_{\mu\nu} \vec{\sigma})^2 \right] = 4 - \frac{1}{4} a^4 \text{Tr} (\vec{R}_{\mu\nu} \vec{\sigma})^2, \quad (4.3.68)$$

the curvature action reads,

$$S_{\text{cur}}[U] = \frac{a^4}{g^2} \sum_{n \in \Lambda} \sum_{\mu < \nu} \text{Tr} (\vec{R}_{\mu\nu} \vec{\sigma})^2. \quad (4.3.69)$$

Now we use the identity,

$$\begin{aligned} \text{Tr} (\vec{R}_{\mu\nu} \vec{\sigma})^2 &= \text{Tr} (R_{\mu\nu a} \sigma_a R_{\mu\nu b} \sigma_b) = \text{Tr} (R_{\mu\nu a} R_{\mu\nu b} \delta_{ab}) = 2 R_{\mu\nu a} R_{\mu\nu a} = \\ &= 2 \vec{R}_{\mu\nu}^2, \end{aligned} \quad (4.3.70)$$

which leads to the action on the lattice for the MTF as a function of the curvature tensor,

$$S_{\text{cur}}[U] = \frac{2a^4}{g^2} \sum_{n \in \Lambda} \sum_{\mu < \nu} \vec{R}_{\mu\nu}^2 = \frac{a^4}{g^2} \sum_{\mu, \nu} \vec{R}_{\mu\nu}^2 \quad (4.3.71)$$

Because every plaquette may be uniquely defined by exactly 2 links, the factor 1/2 arrives in (4.3.71) by changing the sum from plaquettes to the space-time indices. By comparison with the continuous action in (4.3.73), we see, that the coupling constant equals, $g^2 = -\frac{16\pi}{\alpha_f \hbar c}$.

To show, how the WILSON action in (4.3.71), and the curvature energy H_{cur} are related, we begin with the total action of the MTF,

$$S = \int d^4x \mathcal{L} = -\frac{\alpha_f \hbar c}{4\pi} \int d^4x \left(\frac{1}{4} \vec{R}_{\mu\nu}^2 + \Lambda(q_0) \right) = S_{\text{cur}} + S_{\text{pot}}, \quad (4.3.72)$$

where S_{cur} is the continuous version of the WILSON action in (4.3.71),

$$S_{\text{cur}} = -\frac{\alpha_f \hbar c}{4\pi} \int dt \int d^3x \frac{1}{4} \vec{R}_{\mu\nu} \vec{R}^{\mu\nu}. \quad (4.3.73)$$

Because we are considering static snapshots only, $\vec{R}_{\mu\nu}$ does not depend on time and we can evaluate the integral over time separately. By using our definition for dimensionless time units, $t \equiv a\bar{t}$, we get,

$$\int dt = a \int_{\bar{t}}^{\bar{t}+1} d\bar{t} = a. \quad (4.3.74)$$

Hence, we obtain for (4.3.73),

$$S_{\text{cur}} = -\frac{\alpha_f \hbar c}{4\pi} a \int d^3x \frac{1}{4} \vec{R}_{ij} \vec{R}_{ij} = a \underbrace{\left[-\frac{\alpha_f \hbar c}{4\pi} \int d^3x \frac{1}{4} \vec{R}_{ij} \vec{R}_{ij} \right]}_{-H_{\text{cur}}} \stackrel{4.2.2}{=} -aH_{\text{cur}}, \quad (4.3.75)$$

which makes clear, how the WILSON action in a static case relates to the curvature energy H_{cur} in GAMMA action. The potential energy H_{pot} , as well as the outside energy H_{out} , are computed for both methods in the same way, as described in section 4.2.3.

4.4 Measures of accuracy

A lattice simulation of a monopole with radius $\bar{r}_0 = r_0/a$ in lattice units a results in \bar{H}_{tot} , the total energy H_{tot} in units of $\frac{\alpha_f \hbar c}{a}$. We can fix the scale and therefore a by using the analytical solution (3.2.32),

$$H_{\text{mono}} = \frac{\alpha_f \hbar c \pi}{r_0 4}. \quad (4.4.1)$$

Comparing (4.4.1) with the electron rest mass $m_e c^2 \approx 0.511 \text{ MeV}$ ⁶, we are able to find the radius of a monopole to be $r_0 = 2.21 \text{ fm}$. Hence, the lattice distance yields,

$$a = \frac{r_0}{\bar{r}_0} = \frac{2.21 \text{ fm}}{\bar{r}_0}. \quad (4.4.2)$$

Now we are capable of transforming the total energy on the lattice \bar{H}_{tot} into SI-units,

$$H_{\text{tot}} = \frac{\alpha_f \hbar c}{a} \bar{H}_{\text{tot}} = \frac{1.44}{2.21} \bar{r}_0 \bar{H}_{\text{tot}} \text{ MeV}. \quad (4.4.3)$$

As a measure of the deviation of the obtained energy from $m_e c^2 \approx 0.511 \text{ MeV}$, we introduce ΔH , which is defined as,

$$\Delta H \equiv \frac{H_{\text{tot}} - 0.511 \text{ MeV}}{0.511 \text{ MeV}} = \frac{H_{\text{tot}}}{0.511 \text{ MeV}} - 1. \quad (4.4.4)$$

Similarly, for the deviation of the energy ratio $H_{\text{tot}}/H_{\text{pot}}$, which is equal to 4 in the analytical result (3.2.34), we define the following quantity,

$$\Delta R \equiv \frac{4 - H_{\text{tot}}/H_{\text{pot}}}{4} = 1 - \frac{H_{\text{tot}}}{4H_{\text{pot}}}. \quad (4.4.5)$$

With these two measures, which are only valid for the monopole configuration, we are now ready to do some simulations and check the results for their accuracy. After gathering knowledge about optimal parameters and regimes for the numerical simulation, we will continue to apply the algorithm onto dipole configurations.

⁶The most accurate value known up to now (in the year 2020) is $m_e c^2 = 0.51099895000(15) \text{ MeV}$, where the digits in round brackets are uncertain. Hence 0.511 MeV is a very good approximation to the exact value.

Chapter 5

Dipole configurations

Up to now, only monopole configurations were considered. Let us now move on to dipoles. We are able to reuse a lot of modules of the algorithm, we only need to redo the energy outside the box and we have to change the initial configuration. As RESCH showed in his diploma thesis[13], we are essentially left with two different cases. We call them in analogy to usual spin systems, *singlet* and *triplet*. The only characteristic, which make them differentiable are the values of q_0 . For the singlet case, we have $q_0 > 0$ for both monopoles. At the triplet, one monopole has $q_0 < 0$ and at the border between the poles, at the $z = 0$ axis, we have $q_0 = 0$.

5.1 Energy contribution outside the box

As done for the monopoles, we use classical electrodynamics to evaluate the energy outside the box. Again we take care, that the two solitons of the dipole configuration have both a distance of at least $10\bar{r}_0$ to the edges of the box.

To find the electric potential of the dipole, we make use of the superposition principle, adding two monopole potentials,

$$\phi_{\text{monopole}} = \frac{e_0}{4\pi\epsilon_0} \frac{q}{r} = \frac{e_0}{4\pi\epsilon_0} \frac{q}{\sqrt{\rho^2 + z^2}}. \quad (5.1.1)$$

Now, we move two monopoles with different charges apart. For the distance between them, we choose $2a$,

$$\phi_+ = \frac{e_0}{4\pi\epsilon_0} \frac{+1}{\sqrt{\rho^2 + (z - a)^2}} \quad \phi_- = \frac{e_0}{4\pi\epsilon_0} \frac{-1}{\sqrt{\rho^2 + (z + a)^2}}. \quad (5.1.2)$$

By introducing the abbreviations, $z_{\pm} = z \pm a$ and adding the two potentials, we arrive at the dipole potential,

$$\Phi_{\text{dipole}} = \frac{e_0}{4\pi\epsilon_0} \left(\frac{1}{\sqrt{\rho^2 + z_-^2}} - \frac{1}{\sqrt{\rho^2 + z_+^2}} \right), \quad (5.1.3)$$

with the electrical field components, $\vec{E}(r) = -\nabla\Phi$,

$$\begin{aligned} E_{\rho}(\rho, z) &= \frac{e_0}{4\pi\epsilon_0} \left(\frac{\rho}{(\rho^2 + z_+^2)^{3/2}} - \frac{\rho}{(\rho^2 + z_-^2)^{3/2}} \right), \\ E_z(\rho, z) &= \frac{e_0}{4\pi\epsilon_0} \left(\frac{z_+}{(\rho^2 + z_+^2)^{3/2}} - \frac{z_-}{(\rho^2 + z_-^2)^{3/2}} \right). \end{aligned} \quad (5.1.4)$$

We find therefore the energy outside, $H_{\text{out}} = \frac{\epsilon_0}{2} \int_{\mathbb{R}^3 \setminus \text{box}} d^3x |\vec{E}|^2$, which is numerically integrated using a trapezoidal summation. Furthermore, we will use this field components in the following to create a good initial configuration for the minimization procedure.

5.2 Initial configuration

In general, we have four field components for a soliton field, q_0, q_x, q_y, q_z , but due to cylindrical symmetry and the normalization, $|Q| = 1$, we are able to characterize a configuration by two variables at each lattice point. These are the vector's length $l(r, z) = \sqrt{1 - q_r(r, z)^2 - q_z(r, z)^2} = q_0(r, z)$ and the angle $\theta(r, z)$ with respect to the z -axis.

Scalar part

For the scalar part, q_0 , we use the same contour function, as for the monopole, just separated $2a$ away from each other, compare figure 5.2.1. At the $r = 0$ axis, we will get discontinuities, which should be smoothed in the minimization process. The contour function was already shown in figure 4.2.2 and the analytical expression reads respectively for the two poles,

$$q_0(z > 0) = \frac{r_0}{\sqrt{r_0^2 + (\rho^2 + z_-)^2}}, \quad q_0(z \leq 0) = \frac{r_0}{\sqrt{r_0^2 + (\rho^2 + z_+)^2}}. \quad (5.2.1)$$

Note that 5.2.1 is the case for the so called singlet¹ configuration, whereas the triplet one is given in the equations below,

$$q_0(z > 0) = \frac{r_0}{\sqrt{r_0^2 + (\rho^2 + z_-)^2}}, \quad q_0(z < 0) = \frac{-r_0}{\sqrt{r_0^2 + (\rho^2 + z_+)^2}}, \quad (5.2.2)$$

$$q_0(z = 0) = 0.$$

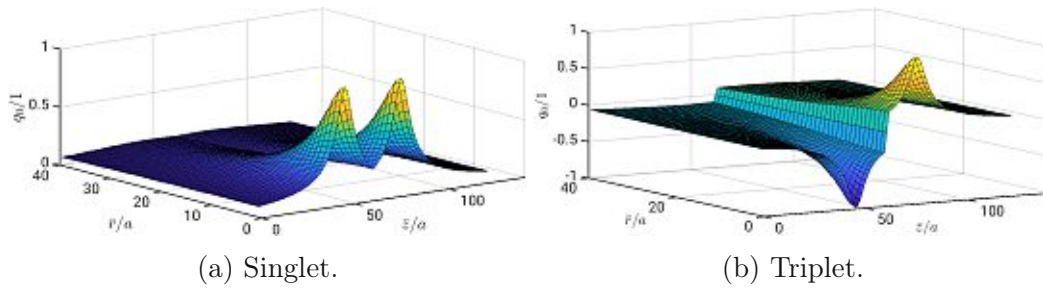


Figure 5.2.1: Shown are the initial configurations of q_0 for the singlet and triplet configuration as used in the MATLAB algorithm.

Vector part

Now we want to find the angle $\theta(r, z)$ for the initial configuration. The most important point here is, that we know already the field of a "classical" dipole from MAXWELL's electrodynamics. Far away from the origin, the two models –topological fermions and classical electrodynamics– coincidence. We use this fact to find an abbreviate initial field and start with the differential equation known from electrodynamics for the dipole field,

$$\frac{d\rho}{E_\rho} = \frac{dz}{E_z}, \quad (5.2.3)$$

with the field components, already found in 5.1.4. By defining the short cuts,

$$z_\pm = z \pm a, \quad u = \frac{z_+}{\rho}, \quad v = \frac{z_-}{\rho}, \quad (5.2.4)$$

$$r_\pm = \sqrt{\rho^2 + z_\pm^2}, \quad r_+ = \rho\sqrt{u^2 + 1}, \quad r_- = \rho\sqrt{v^2 + 1}, \quad (5.2.5)$$

¹For further explanation about singlet- and triplet configurations, see chapter 5.3

we may rewrite the electric field as follows,

$$\begin{aligned} E_\rho(\rho, z) &= \frac{e_0}{4\pi\epsilon_0} \frac{1}{\rho^2} \left[\frac{1}{\sqrt{(u^2 + 1)^3}} - \frac{1}{\sqrt{(v^2 + 1)^3}} \right], \\ E_z(\rho, z) &= \frac{e_0}{4\pi\epsilon_0} \frac{1}{\rho^2} \left[\frac{u}{\sqrt{(u^2 + 1)^3}} - \frac{v}{\sqrt{(v^2 + 1)^3}} \right]. \end{aligned} \quad (5.2.6)$$

Inserting them into the differential equation, 5.2.3 leads to,

$$\frac{d\rho}{\sqrt{(v^2 + 1)^3} - \sqrt{(u^2 + 1)^3}} = \frac{dz}{u\sqrt{(v^2 + 1)^3} - v\sqrt{(u^2 + 1)^3}}. \quad (5.2.7)$$

By help of a rearranged form of the abbreviations in 5.2.4,

$$\rho(u + v) = 2z, \quad \rho(u - v) = 2a \quad \text{and} \quad \rho = \frac{2a}{u - v}, \quad z = a \frac{u + v}{u - v}, \quad (5.2.8)$$

we find the following expressions for the differentials in terms of our substitution variables du and dv ,

$$d\rho = 2a \frac{dv - du}{(u - v)^2} \quad (5.2.9)$$

$$dz = 2a \frac{udv - vdu}{(u - v)^2}. \quad (5.2.10)$$

Those get inserted back in 5.2.7 again, which makes it possible to separate the differential equation and therefore easy to solve.

$$\begin{aligned} \frac{dv - du}{(v^2 + 1)^{\frac{3}{2}} - (u^2 + 1)^{\frac{3}{2}}} &= \frac{udv - vdu}{u(v^2 + 1)^{\frac{3}{2}} - v(u^2 + 1)^{\frac{3}{2}}} \\ (dv - du) \left[u(v^2 + 1)^{\frac{3}{2}} - v(u^2 + 1)^{\frac{3}{2}} \right] &= (udv - vdu) \left[(v^2 + 1)^{\frac{3}{2}} - (u^2 + 1)^{\frac{3}{2}} \right] \\ -vdu(u^2 + 1)^{\frac{3}{2}} - udu(v^2 + 1)^{\frac{3}{2}} &= -udv(u^2 + 1)^{\frac{3}{2}} - vdu(v^2 + 1)^{\frac{3}{2}} \\ (udv - vdv)(u^2 + 1)^{\frac{3}{2}} &= (udu - vdu)(v^2 + 1)^{\frac{3}{2}}. \end{aligned} \quad (5.2.11)$$

After this lengthy rearranging, we get finally the separated form,

$$\frac{du}{\sqrt{(u^2 + 1)^3}} = \frac{dv}{\sqrt{(v^2 + 1)^3}}, \quad (5.2.12)$$

which can be integrated on both sides by using the identity,

$$\frac{d}{du} \frac{u}{\sqrt{u^2 + 1}} = \frac{1}{(u^2 + 1)^{\frac{3}{2}}}. \quad (5.2.13)$$

Hence we get,

$$\frac{z_+}{\sqrt{z_+^2 + \rho^2}} - \frac{z_-}{\sqrt{z_-^2 + \rho^2}} = C, \quad (5.2.14)$$

where we switched to the former variables, ρ and z back again, C is the constant of integration, which we choose to be one in the following. The angle for the initial configuration in both, singlet and triplet case, therefore reads,

$$\theta = \arccos \left(1 - \frac{z_+}{\sqrt{z_+^2 + \rho^2}} + \frac{z_-}{\sqrt{z_-^2 + \rho^2}} \right). \quad (5.2.15)$$

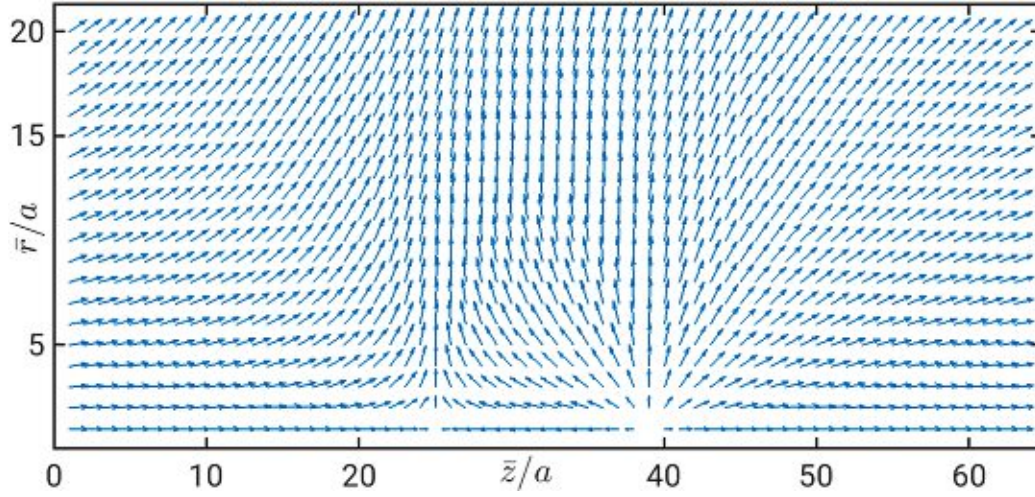


Figure 5.2.2: Vector part of an initial configuration.

5.3 Singlet and triplet on the lattice

As already stated, the difference between singlet and triplet is the sign for the values of q_0 . For the singlet, one soliton sits at the north- and the other on the south pole of the \mathcal{S}^3 sphere. As RESCH and THEUERKAUF found out, the singlet is not stable for small dipole distances $2a$. It was suspected, that the attractive force causes the collapse. THEUERKAUF solved this problem by introducing a radius of fixed soliton field around the centres, which makes it possible to get to very small distances, but producing an error, because obviously those field components does not get involved into the minimization procedure.

This collapse of the dipole configuration should not be the case for the triplet, since there is a force of repulsion, caused from the q_0 field, which has to be

zero at $z = 0$ axis, therefore pushing the centres away. So we expect to find an equilibrium distance, where this repulsion has the same magnitude as the attractive force due to the curvature energy. As we wanted to investigate triplets as well, the first try was to adapt the existing code. By digging deeper into the numerics, we realized that the collapse of the configuration is caused by the tiny inaccuracies in the computation of the two energy contributions. As a second try, an algorithm in MATLAB was created.

5.3.1 Adapting sol.c

The code written by THEUERKAUF was intended to compute only singlet configurations. We want to go a step further and do also triplets. By adapting the algorithm from singlet to triplet dipoles, we have to switch sign of the scalar part for one monopole, $q_0(z < 0) \rightarrow -q_0$, leading to $q_0 = 0$ along the $z = 0$ axis. The charges remain the same for both cases, therefore we are able to use the same procedure for calculating H_{out} , and because H_{pot} is proportional to q_0^{2m} , an even power of q_0 , no changes are needed for the potential energy. For H_{cur} , the dependencies can not be seen on first glance, so we have to be careful.

Curvature energy for negative scalar part

As already used, the zeroth component of energy momentum tensor is,

$$\Theta^0_0 = \underbrace{\frac{\epsilon_0}{2} \vec{\mathbf{E}}\vec{\mathbf{E}}}_{\mathcal{H}_{\text{cur}}} + \underbrace{\frac{\alpha_f \hbar c}{4\pi} \frac{q_0^{2m}}{r_0^4}}_{\mathcal{H}_{\text{pot}}}, \quad (5.3.1)$$

with

$$\begin{aligned} \mathcal{H}_{\text{cur}} &= \frac{1}{2} \epsilon_0 \vec{E}_i \vec{E}_i = \frac{1}{2} \epsilon_0 (\vec{E}_r^2 + \vec{E}_\phi^2 + \vec{E}_z^2) = \\ &= \frac{1}{2} \frac{\alpha_f \hbar c}{4\pi} \frac{1}{r^2} \left\{ q_r^2 [(\partial_z q_0)^2 + (\partial_z q_r)^2 + (\partial_z q_z)^2] + \frac{r^2}{q_0^2} (\partial_r q_r \partial_z q_z - \partial_z q_r \partial_r q_z)^2 + \right. \\ &\quad \left. + q_r^2 [(\partial_r q_0)^2 + (\partial_r q_r)^2 + (\partial_r q_z)^2] \right\}. \end{aligned} \quad (5.3.2)$$

We don't have to care about the bare q_0^2 in (5.3.2), since its square is positive in both cases. To get the derivatives, $(\partial_s q_0)$, the algorithm uses the relation, $q_0^2 + \vec{q}^2 = 1$,

$$q_0 \partial_s q_0 + q_r \partial_s q_r + q_z \partial_s q_z = 0, \quad (5.3.3)$$

which yields for the derivatives,

$$\partial_s q_0 = -\frac{q_r \partial_s q_r + q_z \partial_s q_z}{q_0}. \quad (5.3.4)$$

Therefore, (5.3.2) may be written as,

$$\begin{aligned} \mathcal{H}_{cur} = & \frac{1}{2} \frac{\alpha_f \hbar c}{4\pi} \frac{1}{r^2} \left\{ q_r^2 \left[\left(-\frac{q_r \partial_z q_r + q_z \partial_z q_z}{q_0} \right)^2 + (\partial_z q_r)^2 + (\partial_z q_z)^2 \right] + \right. \\ & + \frac{r^2}{q_0^2} (\partial_r q_r \partial_z q_z - \partial_z q_r \partial_r q_z)^2 + \\ & \left. + q_r^2 \left[\left(-\frac{q_r \partial_r q_r + q_z \partial_r q_z}{q_0} \right)^2 + (\partial_r q_r)^2 + (\partial_r q_z)^2 \right] \right\}, \end{aligned} \quad (5.3.5)$$

which leads to the same curvature energy density for positive and negative q_0 . Hence the algorithm is not able to distinguish between a singlet and a triplet dipole,

$$\mathcal{H}_{cur}(+q_0) = \mathcal{H}_{cur}(-q_0). \quad (5.3.6)$$

A way to solve this problem, would be to numerically calculate the derivatives $\partial_z q_0$ and $\partial_r q_0$. Thus, we have to initialise q_0 on the lattice, which was up to this point not needed. We may use the relation, $q_0 = \pm \sqrt{1 - q_r^2 - q_z^2}$ to compute the q_0 values and set them negative on the lower- and positive on the upper half of the lattice.

After applying this other method to compute the derivatives of q_0 , a test for the singlet case was made, to see if we still get the same energies. Surprisingly the two methods lead to slightly different values and the difference stays relatively constant for big lattices. If we remember, how the numerical derivatives are calculated, we are able to explain this circumstance. At the box's boundaries, the derivative carries the highest error, because only two neighbouring points can be taken into account. For bigger lattices, the impact of the boundaries get less important and so the difference between the two methods approaches an constant.

$n_r \times n_z/2$	\bar{r}_0/a	d/a	E using num. derivatives	E using (5.3.4)	difference
30×30	2	20	0.71880277	0.72195009	3.14732e-3
30×60	2	20	0.72024847	0.72339145	3.14298e-3
30×90	2	20	0.72031251	0.72345549	3.14298e-3
30×120	2	20	0.72032086	0.72346385	3.14299e-3

Table 5.1: Comparison of the numerical values for the total energy in lattice units $\alpha_f \hbar c a^{-1}$, for the two different methods of calculating the derivatives of q_0 .

To find out, which one of the two procedures is more accurate, we interpolate the values for q_0 as shown in figure A.0.3. We are then able to compare the derivatives with the analytic result. As can be seen, in figure 5.3.1, we get more accuracy by computing $\partial_s q_0$ by use of the formula 5.3.4 as THEUERKAUF did.

Unfortunately, this method does not work for the triplet configuration, because at $z = 0$, we get different values for the derivation of $\partial_z q_0$.

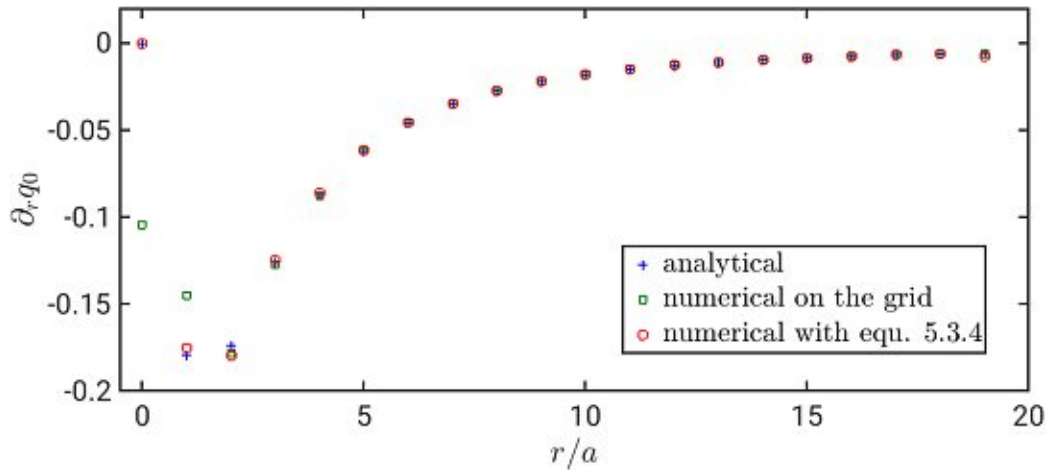


Figure 5.3.1: Comparison for the different methods of calculating the derivatives for $\partial_r q_0$.

5.3.2 Writing a Matlab simulation

The basis for this algorithm builds the c program called *sol9.c* from THEUERKAUF, although we added some improvements when possible. The derivatives for

$r = 0$ were changed under exploiting symmetry arguments to,

$$\begin{aligned}
 \partial_r q_i(r_0, z) &= 0, \quad i = \{0, r, z\}, \\
 \partial_r q_0(r_1, z) &= \frac{q_0(r_1) - 8q_0(r_0) + 8q_0(r_2) - q_0(r_3)}{12a}, \\
 \partial_r q_r(r_1, z) &= \frac{-q_r(r_1) + 8q_r(r_2) - q_r(r_3)}{12a}, \\
 \partial_r q_z(r_1, z) &= \frac{q_z(r_1) - 8q_z(r_0) + 8q_z(r_2) - q_z(r_3)}{12a}.
 \end{aligned} \tag{5.3.7}$$

As THEUERKAUF stated, a problem for dipoles with small distances arose. Due to numerical errors arising from the discretization, values for the potential- and curvature energy density carried a too big error and therefore, the result of the minimization procedure were not physical.

It was suspected, that this phenomenon was due to the attractive force between the two monopoles. But under this circumstance, the soliton field must convert itself into the vacuum state, which carries the least possible energy. Since $H_{\text{pot}} \propto q_0$ and H_{cur} is proportional to the r, z -derivatives of the field components, the vacuum must look like $q_0(r, z) = 0 \quad \forall r, z$ and the vector part, \vec{q} , should be a parallel field.

However, the obtained results had arrows \vec{q} , pointing sometimes criss-cross in the r, z plane, which indicates that the curvature energy gets underestimated in the algorithm. To solve this problem, several approaches were tried,

- Introduction of a border radius:
 Inside of that radius, we provide the analytical solution of the monopoles. Potential- and curvature energy were computed analytically. Outside of that region, the usual numerical method was used. If we calculate the centres of the monopoles analytically, we must not forget that they get contracted in z -direction, due to the curvature energy. Due to the contracted solitons, the dependencies of the various energy contributions must be known as a function of the γ factor. Therefore we did the analytical calculation in B.1, where $E_{\text{cur}}(\gamma)$ and $E_{\text{pot}}(\gamma)$ are presented for a LORENTZ contracted, three dimensional soliton.
 This try was not very successful, because to improve results significantly, the border radius was in the range of $n_r/2$, where n_r is the number of points in one direction.
- Enhancing accuracy by interpolation:
 Due to the functional behaviour of q_0 , the resolution of the poten-

tial energy density is not good enough, especially for smaller lattices ($n_r, n_z < 20$). To get more accurate results, the potential-, as well the curvature energy density were interpolated between the lattice points with a cubic interpolation method. A comparison has shown, that the precision gets better. The price to pay are the run times, which get obviously longer. Nevertheless, the pay off is quite good, as run times don't get unreasonable big.

- Adding a term known from the SKYRME model:
If the accuracy of the minimization routine was drastically increased, the monopole solution showed a wave characteristic in r direction overlapped with the analytical solution. We suspect, that those waves cause the singlet configuration to collapse for small dipole distances. To suppress those waves, we modified the minimization function with an additional term, who reminds us to a kinetic term from the SKYRME model,

$$H = H_{\text{pot}} + H_{\text{cur}} + \lambda \sum_i \left(\partial_i \frac{\vec{q}}{|\vec{q}|} \right)^2, \quad i = \{r, z\}, \quad (5.3.8)$$

where λ is just a factor, which may be chosen one.

The physical interpretation of that term is, that it gives a mass to the photons. Since we are analysing static configurations, it makes no difference for us if the photons carry a mass. But with this term, the interaction is suppressed and therefore, no waves can travel through the lattice. It turned out, that this additional term causes the dipole configuration not to collapse for small dipole distances.

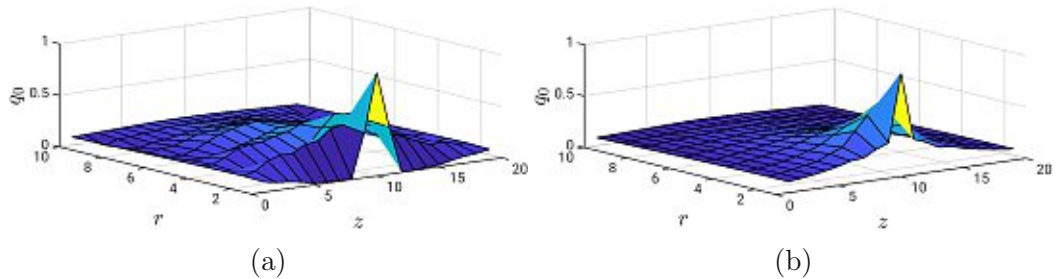


Figure 5.3.2: Comparison of the same computation with (b) and without (a) the additional term from the SKYRME model. To illustrate the rather tiny effect, a very small lattice with $n_r \times n_z = 10 \times 20$ was used.

routine	total energy / MeV	$H_{\text{tot}}/H_{\text{pot}}$	iteration	time
c	0.50815049	3.9304	0	
	0.47753249	4.0535	38	$\approx 25\text{min}$
MATLAB	0.50696222	4.0005	0	
	0.50629401	3.9866	34	$\approx 28\text{min}$
analytical	0.51099895	4.0000		

Table 5.2: Comparison of the two algorithms for a $n_r \times n_z = 30 \times 60$ lattice for a monopole. The improvements (interpolation + additional SKYRME-like term) in the MATLAB routine increase accuracy and run times.

Chapter 6

Results

The results presented from 6.1 to 6.3 were produced from the already existing algorithm, `sol.c` and only treat monopoles. Based on them, the improvements as stated in 5.3.2 were made and applied on dipoles. Dipole results are presented in 6.4.

6.1 Type of integration method

The algorithm written by THEUERKAUF[11] offers the choice of four different numerical integration methods for the equations (4.2.56) and (4.2.57), which calculate the curvature and potential energy, respectively. We have numbered the various methods and they are,

1. SIMPSON's rule[14] using integers,
2. SIMPSON's rule using doubles,
3. trapezoidal RIEMANN sum and
4. simple summation.

To find out, which one of them operates the best, we perform a test for a monopole configuration. Therefore, the rest mass of an electron, 0.511MeV and the theoretical ratio of the energies, $H_{\text{tot}}/H_{\text{pot}} = 4$ are compared with the numerical results in a lattice simulation, using the different integration methods, as showed in figure 6.1.1. As can be seen in the plot, the simple summation works best and therefore we will do all further calculations with this numerical method of integration.

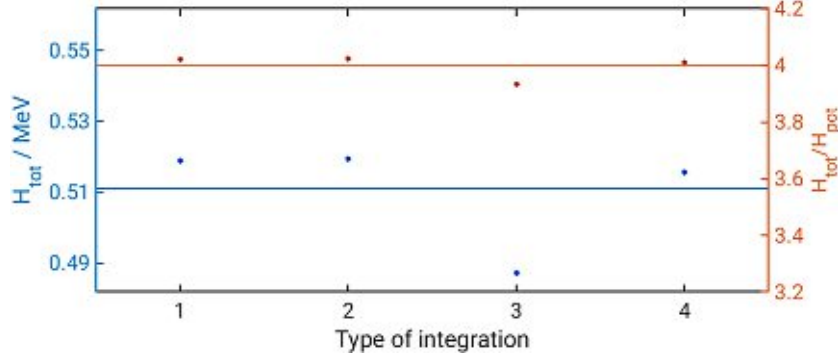


Figure 6.1.1: Comparison of various integration methods for a monopole configuration with a lattice size of $n_z \times n_r = 80 \times 80$. The soliton core was chosen to be $\bar{r}_0 = 12a$. Lines indicate the analytical reference values, dots are measurements from the algorithm.

6.2 Initialisation of a monopole configuration

In this section, we will take a look on the precision of the algorithm, who calculates the GAMMA- and WILSON action for a given soliton configuration. To compare them, an analytical monopole configuration, as stated in (3.2.3) is placed in the origin of the two dimensional lattice. For each run and lattice size, the radius of the soliton core \bar{r}_0 is varied. The algorithm performs the calculation of the potential- and outside energy, \bar{H}_{pot} and \bar{H}_{out} as stated in section 4.2.3. The curvature energy, \bar{H}_{cur} is computed by the different methods, namely GAMMA- and WILSON action. After having all three energy contributions for a single simulation, we are able to sum them up and obtain the total energy \bar{H}_{tot} . This quantity is then used to compute the two measures of accuracy as introduced in section 4.4,

$$\Delta H \equiv \frac{H_{\text{tot}}}{0.511 \text{MeV}} - 1, \quad (6.2.1)$$

$$\Delta R \equiv 1 - \frac{H_{\text{tot}}}{4H_{\text{pot}}}, \quad (6.2.2)$$

which are plotted with respect to the grid sizes and soliton cores to gather general information about the accuracy and precision of the algorithm.

Gamma action

We start with the case of GAMMA action. In figure 6.2.1, the deviation of the energy ΔH is plotted over the soliton's radius \bar{r}_0 for different grid sizes, which

are marked with a colour code. Obviously, for larger lattices, we get better results as can be seen in the overall flattening of the curves. Furthermore, we see that for very small soliton cores \bar{r}_0 , the curves overlap. This behaviour is based on the fact, that for small \bar{r}_0 , the inner structure of the soliton is not dissolve able and in the point of view of the lattice, it just appears as a point charge, as one might say. This behaviour is based on so called lattice artefacts, where discrete derivations blow up, due to too big distances between two neighbouring lattice points. Additionally we recognize, that the curves extend mainly over the negative regime of ΔH . For this reason, we are able to find an optimum for \bar{r}_0 , represented by the maxima of these curves. For even higher values of \bar{r}_0 , the accuracy gets worse again, due to the fact, that our assumption of electrodynamic limit outside the box is not valid any more. In section 4.2.1, we showed, that this assumption holds only for distances in the order of $\approx 10\bar{r}_0$, which means for the lattice sizes, that they have to be at least $10\bar{r}_0$ times wide in every direction.

Analogously, in figure 6.2.2, we see the deviation of the energy ratio ΔR depending on \bar{r}_0 and various grid sizes. We notice again the same behaviour as for the last consideration. For too low, as well for too high ratios of $\bar{r}_0/(\text{latticesize})$ the numerical error is rather big. In contrast to figure 6.2.1, the functions decrease monotonically and therefore we find the optimums at the zero crossings.

These optimal radii \bar{r}_0^{opt} are finally plotted versus the lattice size in figure 6.2.3. We see, that we get two separate lines for optimal radii, therefore we suggest to interpret them as an upper- and lower bound of a good regime and to take care of this boundaries in future simulations.

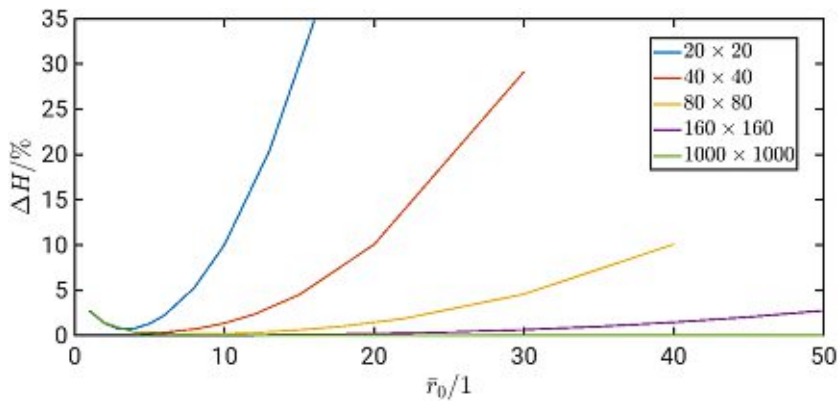


Figure 6.2.1: Plot of the energy deviation ΔH , (6.2.1) as a function of the soliton's core \bar{r}_0 in multiples of the lattice distance a . The different lattice sizes, $n_z \times n_r$, are labelled in colours.

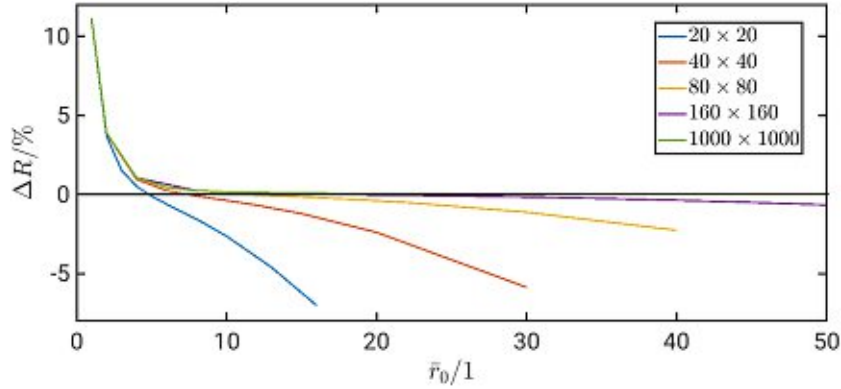


Figure 6.2.2: Plot of the energy ratio's deviation ΔR , (6.2.2) as a function of \bar{r}_0 for various lattice sizes $n_z \times n_r$. The lattices are marked in different colours.

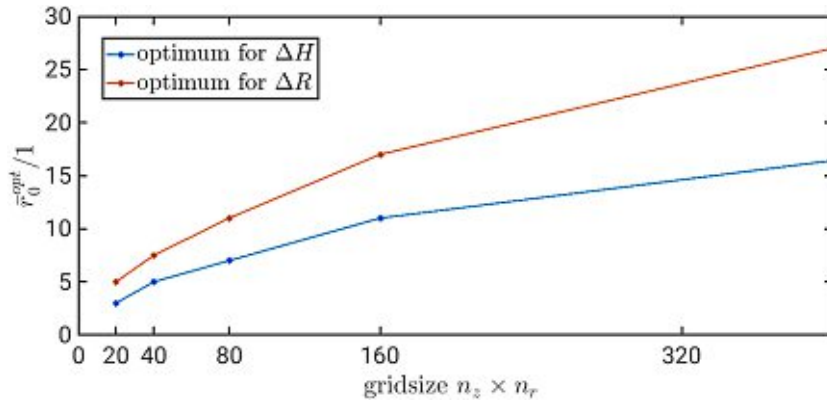


Figure 6.2.3: Plot of the optimal soliton core radius \bar{r}_0^{opt} extracted from figures 6.2.1 and 6.2.2, depending on the lattice size $n_z \times n_r$. The blue line corresponds to the optimal radius regarding the minimization of ΔH and the brown line to the optimum for minimizing ΔR .

Wilson action

The method of calculating the WILSON action differs from GAMMA action in the computation of the curvature energy H_{cur} as explained in section 4.3.3. In figure 6.2.4, we see a comparison between the two methods. Plotted are the deviations ΔH and ΔR for the two methods in dependence of \bar{r}_0 and for the same grid sizes, as used in the previous investigations.

Energy deviations are plotted with blue colour, ratio deviations in black. Pulled through lines indicate the GAMMA method, dashed lines specify the

WILSON method. Regarding ΔH , GAMMA is for all length scales more precise than WILSON. Also for small ratios of $\bar{r}_0/(\text{latticesize})$, GAMMA is better with respect to ΔR .

The only regime where WILSON is more accurate, is at high $\bar{r}_0/(\text{latticesize})$, regarding the ratio deviation. But since for this region, ΔH is tremendous big, it is not useful to work at this high ratios of $\bar{r}_0/(\text{latticesize})$.

To conclude, we are able to see, that the method of GAMMA action works more precise in general and that the region where both methods work the best ($10\bar{r}_0 \approx \text{latticesize}$) becomes wider with higher lattice sizes. Furthermore, by comparing figure 6.2.5, we may suspect, that both algorithm's precision converge in this region towards 0% deviation for infinitely big lattices, which would be continuous space again.

Due to this results, we will work in the minimization procedures with the method of GAMMA action, because the soliton field is minimized with respect to the total energy on the lattice and we don't want, that the avoidable errors get accumulated in every iteration.

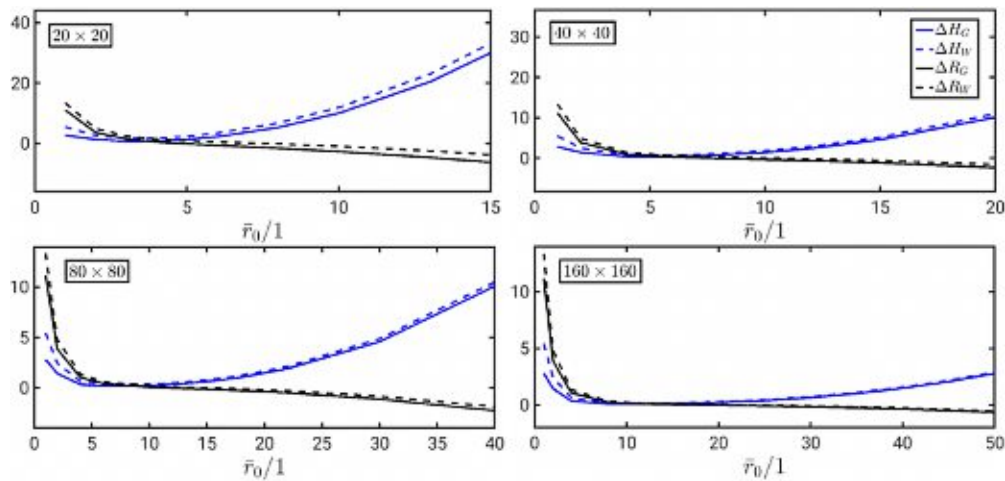


Figure 6.2.4: Comparison of the two methods, GAMMA,- and WILSON action, of calculating the curvature energy and their accuracy regarding ΔH and ΔR . Blue lines indicate energy deviation; black lines ratio deviation, both measured in percent. Dashed lines stand for GAMMA action; pulled through lines for WILSON action.

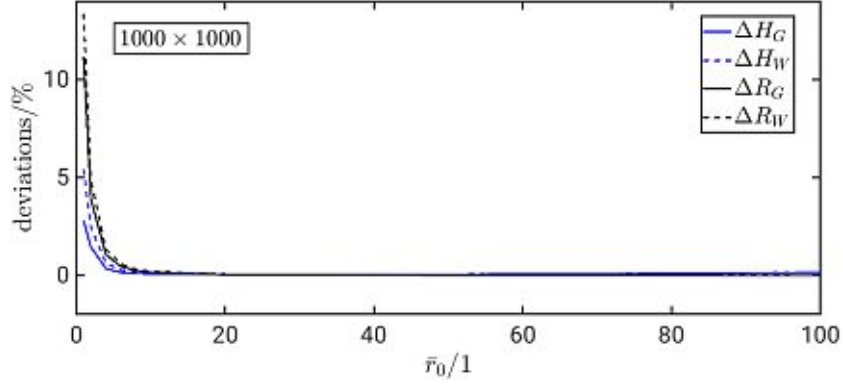


Figure 6.2.5: Continuation of figure 6.2.4 for a rather big lattice, 1000 points in each direction wide.

6.3 Minimization of monopole configurations

Up to now, all we did was to place a monopole on the origin of the lattice and calculate its total energy. Carrying on, we want to minimize this energy to find the ground state, which should be realized by nature.

The minimization procedure is called POWELL and it is taken from Numerical recipes[14]. It is a more dimensional gradient method to find a local minimum of a function depending on many arguments, $f = f(x_1, x_2, \dots, x_n)$. In our case, the function to minimize reads,

$$\bar{H}_{\text{tot}} = \bar{H}_{\text{tot}}(Q(r, z)) = \bar{H}_{\text{tot}}(q_{r,1}, \dots, q_{r,n_r}, q_{z,1}, \dots, q_{z,n_z}). \quad (6.3.1)$$

POWELL starts at a given point on the hyper surface of \bar{H}_{tot} and works its way to the minimum by doing iterations. After the difference of two consecutive iterations falls below a certain value, the algorithm stops. In table 6.1 and figure 6.3.1, we see how the runtime scales up for higher lattices. A fit of the form $f(x) = ax^b + c$ for the runtime was made and leads to a power of $b \approx 5$, which is higher than expected.

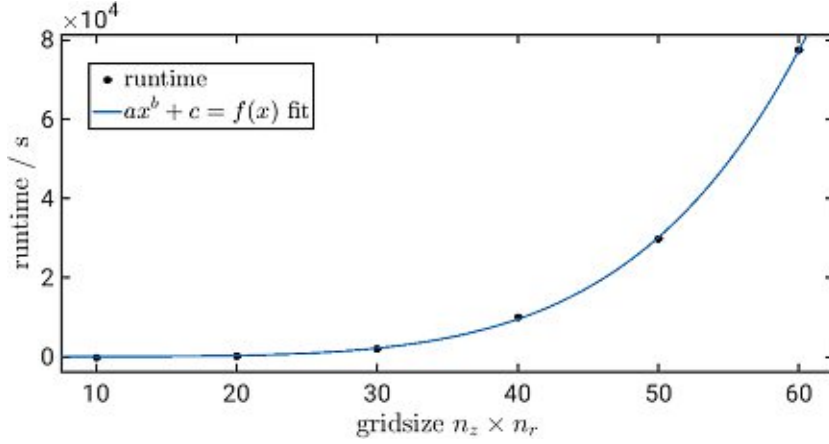


Figure 6.3.1: Evolution of the runtime with the gridsize. The dots mark values from table 6.1 and the line indicates a fit with the parameters $a \approx 5 \cdot 10^{-5}$, $b \approx 5$, $c \approx 92$.

$n_r \times n_z/2$	\bar{r}_0	#iterations	runtime	time/iteration
10×10	1	21	8.6s	0.41s
10×10	2	23	9.7s	0.42s
20×20	2	43	5m35s	7.8s
20×20	3	43	5m20s	7.4s
30×30	3	51	35m13s	41.9s
30×30	4	57	40m19s	42.4s
40×40	4	59	2h46m46s	2m50s
40×40	5	69	3h11m56s	2m47s
50×50	5	70	8h18m14s	7m7s
60×60	6	83	21h31m43s	15m34s

Table 6.1: Number of iterations and runtimes for simulations with various grid sizes and soliton cores \bar{r}_0 . A machine with 4GB of RAM and 4×1.6 GHz processor was used.

In figure 6.3.2, three different cases of table 6.1 are plotted. Shown is the total energy for each iteration in MeV. The lattice constant was fixed with the relation, $\bar{H}_{\text{tot}} \frac{\alpha_f \hbar c}{a} = 0.511 \text{MeV}$, where for each curve, the minimal energy from the last iteration was used. As expected, we see, that the initial soliton

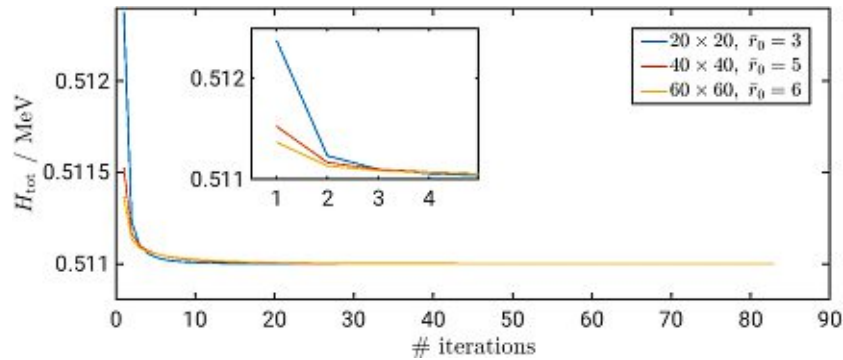


Figure 6.3.2: Minimization of the total energy with respect to the number of iterations used in POWELL's method. Different grid sizes are marked with colours.

field was already very near to the minimum configuration on the lattice. For bigger lattices, the deviation of the initial configuration becomes less. Again, we may suspect, that for an infinitely big lattice, the analytical hedgehog approach as initial configuration would exactly lead to a total energy of 0.511MeV on the lattice after the first iteration.

After just approximately ten iterations, the end value is reached in a very good approximation as shown in the magnification of figure 6.3.2.

The small difference of initial and minimized configuration is shown in figure 6.3.3, where we have plotted a comparison a monopole field, before- and after the minimization. If we take a look to the ratio of $H_{\text{tot}}/H_{\text{pot}}$ in figure 6.3.4, we are able to recognize, that in the first few iterations of the 20×20 lattice, the deviation to the analytical result rises rapidly. For bigger lattices, this spike gets smaller and stays then relatively constant. At the 80×80 lattice, the deviation to the analytical result is about $\approx 1\%$.

The spikes in figure 6.3.4 can be also seen in figure 6.3.5, where energy components for curvature and potential are plotted for each iteration. In the first few iterations, H_{pot} decreases rapidly and linear. After that period it begins a regressive decrease. For H_{cur} , the same behaviour, but mirrored may be recognized. Maybe a closer look to the soliton field for each iteration would provide insight to the process which is going on here. The outside energy is not provided in this graph, because it stays simply constant, since it is calculated in an analytical way. As a check, we list the different energies of the last iteration,

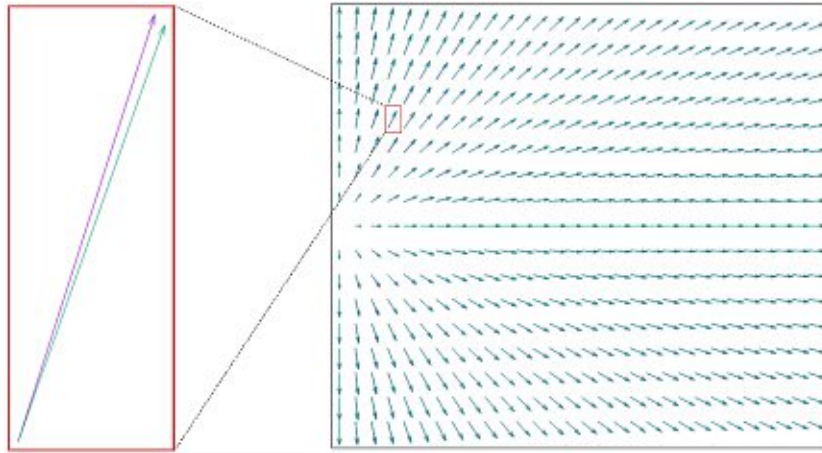


Figure 6.3.3: Comparison of a monopole configuration, before (green) and after (purple) the minimization procedure with a magnification on the left to illustrate the tiny difference. Since we start with the analytical solution, the deviation seen in the magnification arises due to numerical errors.

H_{cur}	H_{pot}	H_{out}	Σ	$H_{\text{tot}}/H_{\text{pot}}$
0.35464	0.12713	0.02923	0.511	4.02

Table 6.2: Obtained energies in MeV from the simulation shown in figure 6.3.5.

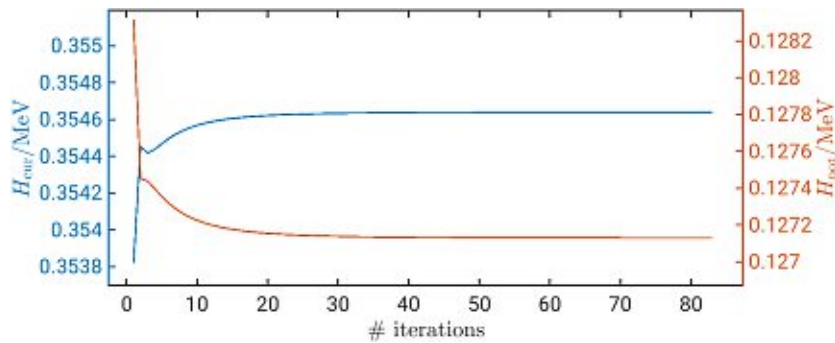


Figure 6.3.5: Potential- and curvature energy as a function of the number of iterations for a 60×60 lattice. Since H_{out} is calculated analytical, it stays constant.

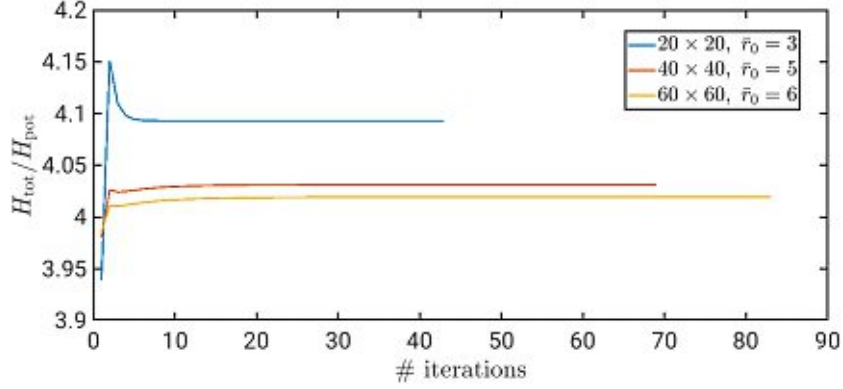


Figure 6.3.4: Ratio of $H_{\text{tot}}/H_{\text{pot}}$ as a function of the number of iterations in the minimizing process. Different grid sizes are marked with colours. We see how the minimization process increases the error, especially for smaller lattices.

6.4 Dipole configurations

6.4.1 Singlet energies

THEUERKAUF presented in his diploma thesis[11] results for the dipole energies as a function of the distance. Although, there is a small error to expect, because the fields had to be fixed near the soliton centres, let us use his data and compare it to the new one. In figure 6.4.1, we see the energies obtained from sol.c compared to the rest mass of two electrons minus the coulomb potential,

$$E = 2m_0c^2 - \frac{\alpha_f \hbar c}{r}, \quad (6.4.1)$$

where r denotes the distance between the two solitons. For this and the following plots, the rest mass was evaluated by doing a monopole computation on the same grid size, $2m_0c^2 \rightarrow 2m'_0c^2$. If we would use the precise value, ≈ 1.022 MeV, we obtain an offset between the curves. For better comparability, we introduced this shift, who does not change the functional behaviour. We see, that the two energy lines split for distances smaller than 40 fm. If we interpret this characteristic as a variable running coupling constant, we may write,

$$E = 2m'_0c^2 - \frac{\alpha_f(r) \hbar c}{r}, \quad (6.4.2)$$

and therefore,

$$\alpha_f(r) = \frac{(2m'_0c^2 - E)r}{\hbar c}. \quad (6.4.3)$$

The values for $\alpha_f(r)$ from sol.c together with the new data (sol.m) with- and without kinetic term from the SKYRME model are plotted in figure 6.4.2.

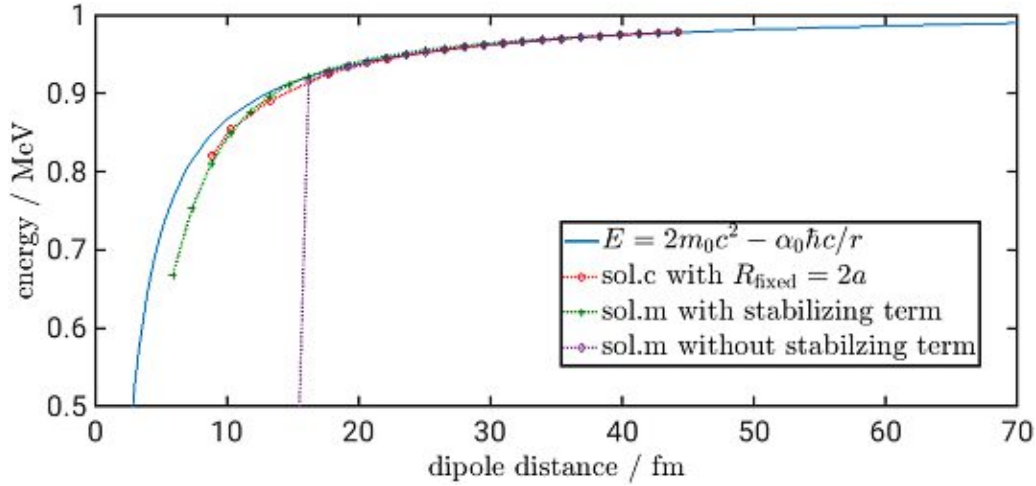


Figure 6.4.1: Dipole results from sol.c[11] and sol.m in comparison with the usual COULOMB potential.

6.4.2 Running coupling in the MTF

By applying formula (6.4.3) on to the data presented in figure 6.4.1, we obtain values for $\alpha_f(r)$ in the MTF, shown in figure 6.4.2.

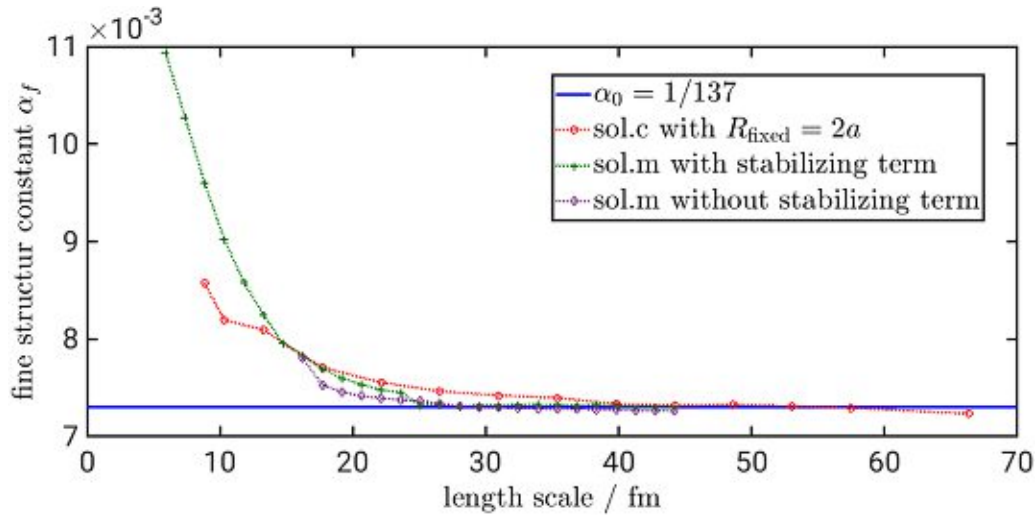


Figure 6.4.2: Running coupling α_f , extracted from lattice computations in sol.c and sol.m. The pulled through line indicates the low energy value $\alpha_0 = 137^{-1}$.

Finally, we are able to compare the running coupling effect in the MTF with measurements made in experiment as presented in table 2.1. Below, we see that running in the MTF occurs about three orders of magnitude too early on the length scale. For the functional behaviour of $\alpha_f(r)$, we can support THEUERKAUF's suggestion in [11], that it shows an exponential behaviour.

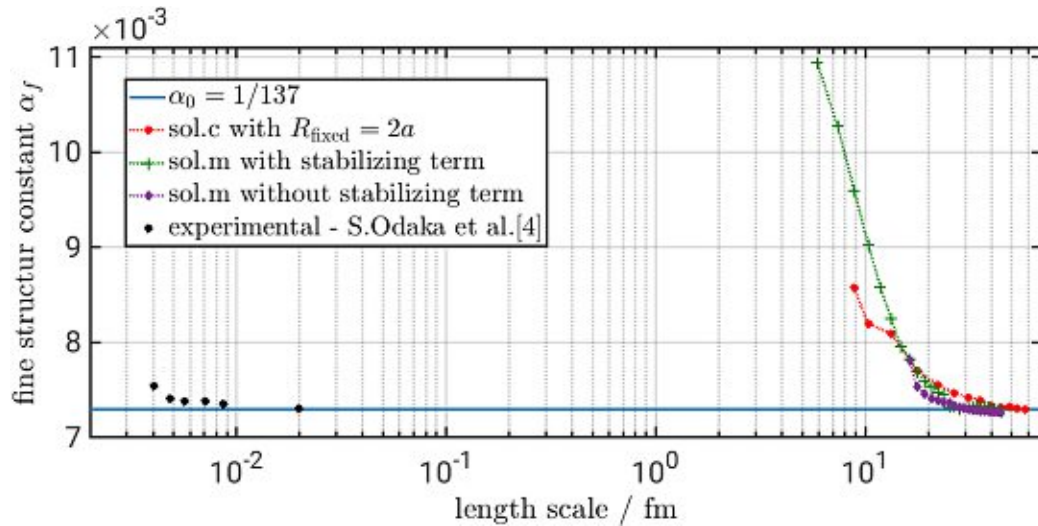


Figure 6.4.3: Numerical data in comparison with the experimental results from S. Odaka et al.[4].

Chapter 7

Conclusion

After introducing the running coupling constant in quantum electrodynamics and presenting the model of topological fermions we put forward a numerical routine for energy minimization of soliton configurations on a lattice. By testing the algorithm upon monopoles we found, that the deviation to the analytical solution of 0.51099895MeV is about, $\Delta H \approx -0.03\%$ ($n_r \times n_z = 100 \times 200$ and after minimization) for the new program created in MATLAB, which is called sol.m.

For sol.c we found, that the GAMMA action works slightly better than WILSON action. Nevertheless, they both coincidence in accuracy for big enough lattices.

sol.c crashed for dipole configuration with small dipole distances. Up to now, it was suggested, that the attractive force causes the configuration to annihilate, but by interpreting the new data, we think that those instabilities are caused from numerical errors. This behaviour could be suppressed by introducing an additional term, similar to the kinetic one in the SKYRME model. Thus we were able to go to smaller distances without fixing field components in the centres of the monopoles as was done in sol.c.

We then compared the new energy values of dipoles with the one from sol.c and all together with the total energy obtaining from $E = 2m_0c^2 - \alpha_f \hbar c/r$. As done in QED, we interpret deviations from that energy as a running coupling effect, which we have plotted and compared to the experimental results[4].

As a main result, we found that α_f^{MTF} starts to deviate from $\alpha_0 = 1/137$ about three orders of magnitude earlier than α_f^{QED} does.

Appendix A

Additional figures and diagrams

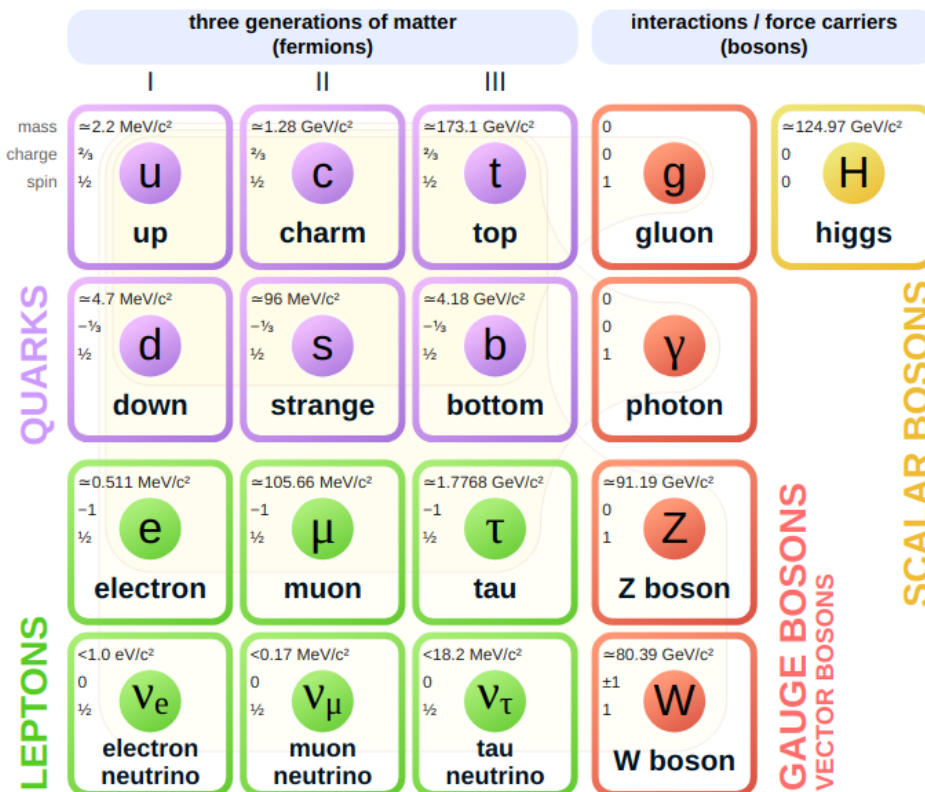


Figure A.0.1: Elemental particles of the standard model.

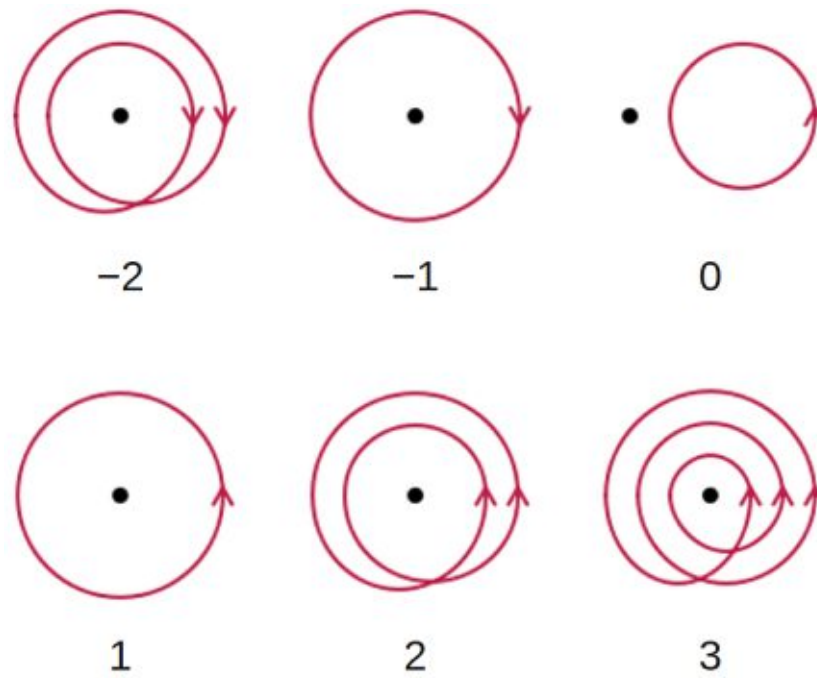


Figure A.0.2: Illustration of various examples for understanding the winding number in the two dimensional case, from https://en.wikipedia.org/wiki/Winding_number.

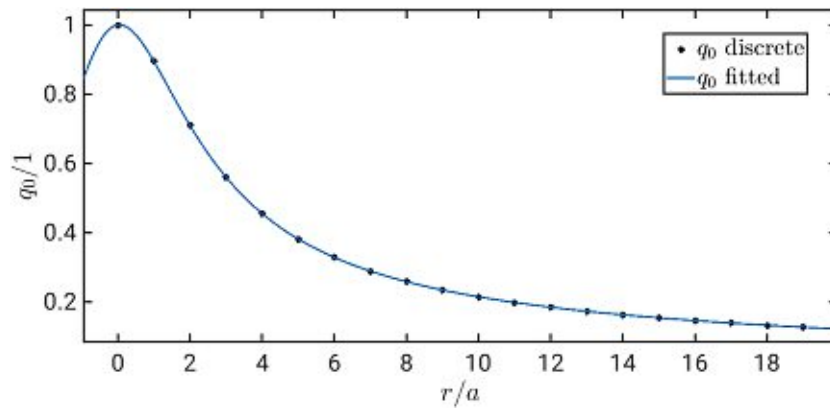


Figure A.0.3: Fitted curve for the numerical q_0 values to evaluate a reference derivation for $\partial_r q_0$.

Appendix B

Lengthy calculations

B.1 Energy contributions for a relativistic soliton

Remoissenet presented the energy contributions for a one dimensional soliton and their dependency on the LORENTZ factor γ in [10]. Now we want to redo this calculation for kinetic-, curvature- and potential energy for a moving soliton in three dimensions. We begin with energy-momentum tensor and its 00 component,

$$\begin{aligned}
 \Theta^0_0 &= -\frac{\alpha_f \hbar c}{4\pi} \vec{R}_{0\sigma} \vec{R}^{0\sigma} - \mathcal{L}(x) = -\frac{\alpha_f \hbar c}{4\pi} \left(\vec{R}_{0\sigma} \vec{R}^{0\sigma} - \frac{1}{4} \vec{R}_{\mu\nu} \vec{R}^{\mu\nu} - \Lambda(q_0) \right) = \\
 &= -\frac{\alpha_f \hbar c}{4\pi} \left(\vec{R}_{0\sigma} \vec{R}^{0\sigma} - \frac{1}{4} \vec{R}_{\mu\nu} \vec{R}^{\mu\nu} \right) + \frac{\alpha_f \hbar c}{4\pi} \Lambda(q_0) = \\
 &= -\frac{\alpha_f \hbar c}{4\pi} \left(\vec{R}_{0\sigma} \vec{R}^{0\sigma} - \frac{1}{4} \left(\vec{R}_{ij} \vec{R}^{ij} + 2\vec{R}_{0\sigma} \vec{R}^{0\sigma} \right) \right) + \frac{\alpha_f \hbar c}{4\pi} \Lambda(q_0).
 \end{aligned} \tag{B.1.1}$$

We split the contributions in the following, reasonable way. The kinetic energy in the SINE-GORDON model is in the MTF the magnetic field energy, the tension energy in the springs is related to the electric field energy, and the potential term has the same interpretation,

$$\begin{aligned}
 E_{\text{kin}} &= -\frac{\alpha_f \hbar c}{4\pi} \int_V d^3x \frac{1}{2} \vec{R}_{0\sigma} \vec{R}^{0\sigma}, \\
 E_{\text{cur}} &= \frac{\alpha_f \hbar c}{4\pi} \int_V d^3x \frac{1}{4} \vec{R}_{ij} \vec{R}^{ij}, \\
 E_{\text{pot}} &= \frac{\alpha_f \hbar c}{4\pi} \int_V d^3x \Lambda.
 \end{aligned} \tag{B.1.2}$$

To calculate the tensor components, we take the following ansatz for a moving soliton,

$$Q_v(x) = \underbrace{\cos \alpha(|\mathbf{r} - \mathbf{v}t|)}_{q_0} - i\vec{\sigma} \cdot \underbrace{\frac{\mathbf{r} - \mathbf{v}t}{|\mathbf{r} - \mathbf{v}t|}}_{\vec{q}} \sin \alpha(|\mathbf{r} - \mathbf{v}t|), \quad (\text{B.1.3})$$

with

$$\alpha = \arctan \left(\frac{|\mathbf{r} - \mathbf{v}t|}{r_0} \right), \quad (\text{B.1.4})$$

and the velocity in z direction

$$\mathbf{v} = (0, 0, v). \quad (\text{B.1.5})$$

The LORENTZ factor comes into play the following way,

$$|\mathbf{r} - \mathbf{v}t| = \text{abs} \begin{pmatrix} x \\ y \\ \gamma(z - vt) \end{pmatrix} = \sqrt{x^2 + y^2 + \gamma^2(z - vt)^2}. \quad (\text{B.1.6})$$

In the next step, the field components q_0 , \vec{q} as well as their derivations in t, x, y and z direction were computed. With them, the components of the affine connections $\vec{\Gamma}_\mu = q_0 \partial_s \vec{q} - \vec{q} \partial_s q_0 + \vec{q} \times \partial_s \vec{q}$ and then the tensor components $\vec{R}_{\mu\nu} = \vec{\Gamma}_\mu \times \vec{\Gamma}_\nu$ were calculated. This work is not very complex, but troublesome. The volume integrations in (B.1.2), yield finally,

$$- \int_V d^3x \frac{1}{2} \vec{R}_{0\sigma} \vec{R}^{0\sigma} = \frac{1}{2} \frac{\pi^2}{r_0} v^2 \gamma, \quad (\text{B.1.7})$$

$$\int_V d^3x \frac{1}{4} \vec{R}_{ij} \vec{R}^{ij} = \frac{\pi^2}{2r_0} \left(\frac{1}{2\gamma} + \gamma \right), \quad (\text{B.1.8})$$

$$\int_V d^3x \Lambda = \frac{\pi^2}{4r_0} \frac{1}{\gamma}. \quad (\text{B.1.9})$$

The sum of the energy contributions therefore is,

$$E_{\text{tot}} = E_{\text{pot}} + E_{\text{cur}} + E_{\text{kin}} = \frac{\alpha_f \hbar c}{4\pi} \cdot \frac{\pi^2}{r_0} \left(\frac{1}{4\gamma} + \frac{1}{4\gamma} + \frac{\gamma}{2} + \frac{1}{2} v^2 \gamma \right), \quad (\text{B.1.10})$$

and inserting the velocity v as a function of γ with speed of light, $c \equiv 1$,

$$\gamma = \frac{1}{\sqrt{1 - v^2}} \implies v^2 = 1 - \frac{1}{\gamma^2}, \quad (\text{B.1.11})$$

we get,

$$\begin{aligned}
 E_{\text{tot}}(\gamma) &= \frac{\alpha_f \hbar c}{4\pi} \cdot \frac{\pi^2}{r_0} \left(\frac{1}{2\gamma} + \frac{\gamma}{2} + \frac{1}{2} \left(1 - \frac{1}{\gamma^2} \right) \gamma \right) = \\
 &= \frac{\alpha_f \hbar c}{4\pi} \cdot \frac{\pi^2}{r_0} \left(\frac{1}{2\gamma} + \frac{\gamma}{2} + \frac{\gamma}{2} - \frac{1}{2\gamma} \right) = \\
 &= \underbrace{\frac{\alpha_f \hbar c}{4} \frac{\pi}{r_0}}_{H_{\text{mono}}} \cdot \gamma = m_0 c^2 \gamma.
 \end{aligned} \tag{B.1.12}$$

Therefore, we have explicitly shown, that the relativistic mass gain for a moving soliton holds.

B.2 Dual tensor identity

We want to show that following identity holds,

$$\epsilon_{\mu\nu\rho\sigma} \partial_\lambda f^{\lambda\sigma} = \partial_\mu {}^* f_{\nu\rho} + \partial_\nu {}^* f_{\rho\mu} + \partial_\rho {}^* f_{\mu\nu}. \tag{B.2.1}$$

By use of the identity for dual tensors, $f_{\mu\nu} = -1/2 \epsilon_{\mu\nu\rho\sigma} {}^* f^{\rho\sigma}$, we get for the right hand side,

$$\epsilon_{\mu\nu\rho\sigma} \partial_\lambda f^{\lambda\sigma} = -\frac{1}{2} \epsilon_{\mu\nu\rho\sigma} \epsilon^{\lambda\alpha\beta\sigma} \partial_\lambda {}^* f_{\alpha\beta} = \frac{1}{2} \delta_{\mu\nu\rho}^{\lambda\alpha\beta} \partial_\lambda {}^* f_{\alpha\beta}. \tag{B.2.2}$$

The KRONECKER-Delta with the three sub- and super scripts yields,

$$\delta_{\mu\nu\rho}^{\lambda\alpha\beta} = \det \begin{pmatrix} \delta_\mu^\lambda & \delta_\nu^\lambda & \delta_\rho^\lambda \\ \delta_\mu^\alpha & \delta_\nu^\alpha & \delta_\rho^\alpha \\ \delta_\mu^\beta & \delta_\nu^\beta & \delta_\rho^\beta \end{pmatrix}, \tag{B.2.3}$$

and therefore (B.2.2) becomes,

$$\begin{aligned}
 &\frac{1}{2} \delta_{\mu\nu\rho}^{\lambda\alpha\beta} \partial_\lambda {}^* f_{\alpha\beta} = \\
 &= \frac{1}{2} (\delta_\mu^\lambda \delta_\nu^\alpha \delta_\rho^\beta + \delta_\nu^\lambda \delta_\rho^\alpha \delta_\mu^\beta + \delta_\rho^\lambda \delta_\mu^\alpha \delta_\nu^\beta - \delta_\mu^\beta \delta_\nu^\alpha \delta_\rho^\lambda - \delta_\nu^\beta \delta_\rho^\alpha \delta_\mu^\lambda - \delta_\rho^\beta \delta_\mu^\alpha \delta_\nu^\lambda) \partial_\lambda {}^* f_{\alpha\beta} = \\
 &= \frac{1}{2} (\partial_\mu {}^* f_{\nu\rho} + \partial_\nu {}^* f_{\rho\mu} + \partial_\rho {}^* f_{\mu\nu} - \partial_\rho {}^* f_{\nu\mu} - \partial_\mu {}^* f_{\rho\nu} - \partial_\nu {}^* f_{\mu\rho}).
 \end{aligned} \tag{B.2.4}$$

By making use of the antisymmetry of ${}^* f_{\rho\nu} = -{}^* f_{\nu\rho}$, we obtain,

$$\frac{1}{2} \delta_{\mu\nu\rho}^{\lambda\alpha\beta} \partial_\lambda {}^* f_{\alpha\beta} = \frac{1}{2} (2\partial_\mu {}^* f_{\nu\rho} + 2\partial_\nu {}^* f_{\rho\mu} + 2\partial_\rho {}^* f_{\mu\nu}), \tag{B.2.5}$$

which ends the proof.

List of Figures

2.1.1 The two different time ordered possibilities for the interaction via a virtual particle X, from[1].	8
2.2.1 e^-e^+ annihilation[1].	11
2.2.2 Leading order (a) and $\mathcal{O}(e_0^4)$ corrections (b-e) of the considered e^-e^+ annihilation[1].	12
2.2.3 Higher order loop corrections[1].	13
3.1.1 Mechanical model[8].	17
3.1.2 Particle characteristics of two solitons with opposite twist of ϕ , annihilating each other, if friction is considered. Plotted is equation (3.1.13, for different times T	20
3.2.1 Illustration for the definition of the curvature tensor, taken from [8].	23
3.2.2 For $\Lambda = 0$, electrodynamics is recovered, therefore photons may be interpreted as goldstone bosons of the MTF. Illustration was taken from [8].	26
3.2.3 Plot of the three terms energy densities in (3.2.31). Tangential and potential components approach zero relatively quickly, whereas the radial component shows the usual $1/r^2$ behaviour for large distances.	29
3.2.4 "Elemental soliton configurations". Shown are cross-sections of the spheric symmetrical vector part, \vec{q} . The sign of q_0 is depicted in the colour with, red stands for $q_0 > 0$ and blue for $q_0 < 0$. Illustration was made by THEUERKAUF[11].	34
4.2.1 Integration areas.	40
4.2.2 Plot of the scalar part q_0 as a function of the ratio $r/r_0 \equiv \eta$. Potential energy is proportional to q_0^6	42
5.2.1 Shown are the initial configurations of q_0 for the singlet and triplet configuration as used in the MATLAB algorithm.	65

5.2.2	Vector part of an initial configuration.	67
5.3.1	Comparison for the different methods of calculating the derivatives for $\partial_r q_0$	70
5.3.2	Comparison of the same computation with (b) and without (a) the additional term from the SKYRME model. To illustrate the rather tiny effect, a very small lattice with $n_r \times n_z = 10 \times 20$ was used.	72
6.1.1	Comparison of various integration methods for a monopole configuration with a lattice size of $n_z \times n_r = 80 \times 80$. The soliton core was chosen to be $\bar{r}_0 = 12a$. Lines indicate the analytical reference values, dots are measurements from the algorithm.	76
6.2.1	Plot of the energy deviation ΔH , (6.2.1) as a function of the soliton's core \bar{r}_0 in multiplies of the lattice distance a . The different lattice sizes, $n_z \times n_r$, are labelled in colours.	77
6.2.2	Plot of the energy ratio's deviation ΔR , (6.2.2) as a function of \bar{r}_0 for various lattice sizes $n_z \times n_r$. The lattices are marked in different colours.	78
6.2.3	Plot of the optimal soliton core radius \bar{r}_0^{opt} extracted from figures 6.2.1 and 6.2.2, depending on the lattice size $n_z \times n_r$. The blue line corresponds to the optimal radius regarding the minimization of ΔH and the brown line to the optimum for minimizing ΔR	78
6.2.4	Comparison of the two methods, GAMMA,- and WILSON action, of calculating the curvature energy and their accuracy regarding ΔH and ΔR . Blue lines indicate energy deviation; black lines ratio deviation, both measured in percent. Dashed lines stand for GAMMA action; pulled through lines for WILSON action.	79
6.2.5	Continuation of figure 6.2.4 for a rather big lattice, 1000 points in each direction wide.	80
6.3.1	Evolution of the runtime with the gridsize. The dots mark values from table 6.1 and the line indicates a fit with the parameters $a \approx 5 \cdot 10^{-5}$, $b \approx 5$, $c \approx 92$	81
6.3.2	Minimization of the total energy with respect to the number of iterations used in POWELL's method. Different grid sizes are marked with colours.	82

6.3.3 Comparison of a monopole configuration, before (green) and after (purple) the minimization procedure with a magnification on the left to illustrate the tiny difference. Since we start with the analytical solution, the deviation seen in the magnification arises due to numerical errors.	83
6.3.5 Potential- and curvature energy as a function of the number of iterations for a 60×60 lattice. Since H_{out} is calculated analytical, it stays constant.	83
6.3.4 Ratio of $H_{\text{tot}}/H_{\text{pot}}$ as a function of the number of iterations in the minimizing process. Different grid sizes are marked with colours. We see how the minimization process increases the error, especially for smaller lattices.	84
6.4.1 Dipole results from sol.c[11] and sol.m in comparison with the usual COULOMB potential.	85
6.4.2 Running coupling α_f , extracted from lattice computations in sol.c and sol.m. The pulled through line indicates the low energy value $\alpha_0 = 137^{-1}$	85
6.4.3 Numerical data in comparison with the experimental results from S. Odaka et al.[4].	86
A.0.1Elemental particles of the standard model.	89
A.0.2Illustration of various examples for understanding the winding number in the two dimensional case, from https://en.wikipedia.org/wiki/Winding_number	90
A.0.3Fitted curve for the numerical q_0 values to evaluate a reference derivation for $\partial_r q_0$	90

List of Tables

2.1	Shown are the measured ratios of α_f at various energies from the VENUS Collaboration[4], where BHABBA-scattering and muon-pair production at e^+e^- collisions were used. The first measurement at t_0 defines the scale and has a high error, compared to the ratios $\alpha(t_m)/\alpha(t_0)$, for which systematic errors in the experimental setup cancel. As can be clearly seen, the fit rises with higher energies Q	10
4.1	Compilation of the various energies in,- and outside a sphere with radius $r = 10r_0$. By comparing radial, tangential and potential energy outside the box, it can be seen that electrodynamic limit is very well approached.	41
5.1	Comparison of the numerical values for the total energy in lattice units $\alpha_f \hbar c a^{-1}$, for the two different methods of calculating the derivatives of q_0	70
5.2	Comparison of the two algorithms for a $n_r \times n_z = 30 \times 60$ lattice for a monopole. The improvements (interpolation + additional SKYRME-like term) in the MATLAB routine increase accuracy and run times.	73
6.1	Number of iterations and runtimes for simulations with various gridsizes and solitoncores \bar{r}_0 . A machine with 4GB of RAM and 4×1.6 GHz processor was used.	81
6.2	Obtained energies in MeV from the simlation shown in figure 6.3.5.	83

Bibliography

- [1] Mark Thomson. *Modern particle physics*. Cambridge University Press, New York, 2013.
- [2] Richard P. Feynman. *QED – The strange theory of light and matter*. Princeton University Press, 1985. S. 129.
- [3] A. Sommerfeld. *Zur Quantentheorie der Spektrallinien*. *Ann Phys* 51:1-94, 125-167, volume 356. March 2006.
- [4] S. Odaka et al. *Measurement of the Running of Effective QED Coupling at Large Momentum Transfer in the Spacelike Region*. *Physical Review Letters*, 1998.
- [5] M. Kaku. *Quantum Field Theory: A Modern Introduction*. Oxford University Press, 1993.
- [6] Tests of the standard model and constraints on new physics from measurements of fermion-pair production at 189-209 gev at lep. *The European Physical Journal C*, 33(2):173–212, Mar 2004.
- [7] Manfred Faber. Charges and electromagnetic radiation as topological excitations. *Advances in High Energy Physics*, 2017, 07 2017.
- [8] Manfred Faber. Spin and charge from space and time. *Journal of Physics: Conference Series*, 504:012010, 04 2014.
- [9] Manfred Faber. *Solitonen, Differentialgeometrie und Topologie*. Script, Physics, Technische Universität Wien, 2019.
- [10] M. Remoissenet. *Waves called solitons : concepts and experiments / M. Remoissenet*. Springer-Verlag, Berlin ;.
- [11] Dominik Theuerkauf. *Charged particles in the model of topological fermions*. Diploma thesis, Physics, Technische Universität Wien, 2016.

- [12] Joachim Wabnig. *Interaction in the Model of Topological Fermions*. Diploma thesis, Physics, Technische Universität Wien, 2001.
- [13] Josef Resch. *Numerische Analyse an Dipolkonfigurationen im Modell topologischer Fermionen*. Diploma thesis, Physics, Technische Universität Wien, 2011.
- [14] William H. Press, Saul A. Teukolsky, William T. Vetterling, and Brian P. Flannery. *Numerical Recipes 3rd Edition: The Art of Scientific Computing*. Cambridge University Press, USA, 3 edition, 2007.
- [15] Christof Gattringer and Christian B. Lang. *Quantum chromodynamics on the lattice*, volume 788. Springer, Berlin, 2010.